MICORSEISMIC MODELING OF HYDRAULIC FRACTURING AND ANALYSIS OF LOCATION AND DETECTABILITY UNCERTAINTIES

BY

Haitham Alsahfy

A Thesis Presented to the
DEANSHIP OF GRADUATE STUDIES

KING FAHD UNIVERSITY OF PETROLEUM & MINERALS
DHAHRAN, SAUDI ARABIA

In Partial Fulfillment of the
Requirements for the Degree of

MASTER OF SCIENCE

In

EARTH SCIENCES

NOVEMBER, 2014.

MICROSEISMIC MODELING OF HYDRAULIC FRACTURING AND ANALYSIS OF LOCATION AND DETECTABILITY UNCERTAINTIES

Haitham Alsahfy

EARTH SCIENCES DEPARTMENT

November, 2014

KING FAHD UNIVERSITY OF PETROLEUM & MINERALS

DHAHRAN- 31261, SAUDI ARABIA

DEANSHIP OF GRADUATE STUDIES

This thesis, written by **Haitham Alsahfy** under the direction of his thesis advisor and approved by his thesis committee, has been presented and accepted by the Dean of Graduate Studies, in partial fulfillment of the requirements for the degree of **MASTER OF SCIENCE IN GEOPHYSICS**.

Prof. Gabor Korvin
(Advisor)

Dr. Isma'il Kaka SanLinn
(Co-Advisor)

Dr. Mohammed Ameen
(Member)

Dr. Abdulaziz Al-Shaibani
Department Chairman

Dr. Salam A. Zummo
Dean of Graduate Studies

7/5/15

Date

Dedicated to Rehab, Bader, and my Parents.

ACKNOWLEDGMENTS

I would like to acknowledge

Dr. Aldo Vesnaver

For his support and contribution throughout my Thesis research

Dr. Aldo was my original committee chairman and advisor until later stages.

I also would like to acknowledge

Dr. Huseyin S Kuleli

For his support, fruitful discussions, and Ideas throughout my Thesis research

I consider him as one of my committee members

TABLE OF CONTENTS

LIST OF TABLES

LIST OF FIGURES

LIST OF TECHNICAL TERMS & ABBREVIATIONS

Accuracy:	*Degree of closeness of measurements of a quantity to that quantity's actual (true) value.*
***Anisotropy**:*	*Quality of a material property that depends on the direction along which it is measured.*
***Back-azimuth**:*	*Azimuth from the epicenter of an event to a receiver.*
***Borehole**:*	*A hole driven into the ground to obtain geological information, release water, etc.*
***Casing**:*	*Steel pipe placed in an oil or gas well as drilling progresses to prevent the wall of the hole from caving in during drilling, to prevent seepage of fluids, and to provide a means of extracting petroleum if the well is productive (oilgasglossary.com).*
***Dip angle**:*	*Angle between a given direction and the vertical axis (positive upward).*
***Doublet**:*	*Pair of earthquakes showing almost identical waveforms in the seismograms.*
Effective velocity:	*Velocity of a homogeneous medium equivalent to a layered 1D medium, that is, yielding the same zero-offset traveltime*
***Gas shale**:*	*Organic-rich shale formation hosting natural gas.*
Hodogram:	*Cross-plot of two horizontal components of particle motion over a time window.*
***HTI**:*	*Horizontal transverse isotropy*
***Hydraulic Fracturing**:*	*Process of injecting fluids under high pressure into a formation to fracture the target rock and increase its permeability.*
***Isotropy**:*	*Quality of a material property that does not depend on the direction along which it is measured.*
***Offset**:*	*Horizontal distance between source and receivers.*
***Origin time**:*	*Time of microseismic event occurrence.*
***Out-of-pay**:*	*Outside the pay portion of a reservoir (see Pay).*
***Overburden**:*	*Rocks overlying the reservoir.*
***Pay**:*	*A reservoir or portion of a reservoir that contains economically producible hydrocarbons.*

Picking error:	*Errors in identifying, naming and measuring seismic phases.*
***PKS**:*	*Unspecified P-wave bottoming in the Earth's core and converting to S at the core-mantle boundary.*
Poisson	*Elastic constant that is a measure of the compressibility of a material perpendicular to applied stress, or the ratio of latitudinal to longitudinal strain.*
***Precision**:*	*Degree to which repeated measurements under unchanged conditions show the same results (http://en.wikipedia.org).*
***Ray-path**:*	*Geometric path between the transmitting and receiving locations.*
***Shale gas**:*	*Natural gas, mainly methane, produced from shales.*
***Shear-wave**:*	*Splitting of a linear polarized shear wave into orthogonally polarized fast and slow shear waves, when travelling in anisotropic media.*
***Split time**:*	*Time delay between the fast and slow split shear waves.*
***Spread**:*	*The geometrical pattern of groups of geophones relative to the seismic source.*
***TI**:*	*Transverse isotropy*
***Time-delay**:*	*The delay between the arrival times of the two split shear-wave phases in case of seismic anisotropy.*
***TTI**:*	*Tilted transverse isotropy*
Unconventional reservoirs:	*Rocks hosting hydrocarbons but characterized by a very low permeability, like gas shales and tight sands and carbonates.*
***VTI**.*	*Vertical transverse isotropy*
***Wellbore**:*	*A borehole; the hole drilled by the bit (oilgasglossary.com).*
***Wellhead**:*	*The equipment installed on top of the borehole at the surface.*

ABSTRACT

Full Name	:	[Haitham Own Mohammed Alsahfy]
Thesis Title	:	[Microseismic Modeling Of Hydraulic Fracturing And Analysis Of Location and Detectability Uncertainties]
Major Field	:	[Geophysics]
Date of Degree	:	[November, 2014]

Multistage hydraulic fracturing is one of the key technologies for the successful development of unconventional reservoirs. Fracturing is conducted through a high pressure pumping of fluids to induce fractures into the rock matrix, and establish a complex network to enhance connectivity between the pores system. Proponents or acid are pumped alongside to keep the induced fractures network open after stimulation to allow hydrocarbons to flow, and thereby maintaining reservoir conductivity and productivity. Microseismic data can provide critical information for optimizing both the hydraulic stimulation operations and the resulting production from wells, and hypocenter locations form the basis of simulated rock volume estimation.

MS events location uncertainty is a challenge in microseismic data interpretation. Forward modeling has shown that velocity model and acquisition geometry settings are the main sources of those uncertainties as covered by this research, as well as waveforms arrivals picking. Construction of a detailed velocity structure is critical for accurate predication of arrival times, and it requires sufficient details. Depending on the lithological details and acoustic characteristics of the reservoir, velocity heterogeneity and anisotropy parameters may need to be incorporated in the processing workflow. Transverse Isotropy velocity model calibration is most suitable solution to correct for anisotropy effects on hypocenter location estimation.

ملخص الرسالة

الاسم الكامل: هيثم عون محمد الصحفي

عنوان الرسالة:
النمذجه الميكروسايزميه للتكسير الهيدروليكي و تحليل إمكانية الكشف والمواقع للاحدثيات و مجال الخطأ

التخصص: جيوفيزياء

تاريخ الدرجة العلمية: نوفمبر 2015

التكسير الهيدروليكي متعدد المراحل هي واحدة من التكنولوجيات الرئيسية لنجاح تطوير المكامن غير التقليدية. التكسير يتم من خلال ضخ ضغط عالي من السوائل للحث على تكسير الطبقه المستهدفه، وإنشاء شبكة معقدة لتعزيز الترابط بين نظام المسام. يتم ضخ حبيبات رمليه أو حمض اسيدي جنبا إلى جنب للحفاظ على شبكة الكسور الناجمة مفتوحة بعد التحفيز للسماح لتدفق النفط والغاز، وبالتالي الحفاظ على الموصلية والإنتاجية للمكمن المستهدف يمكن البيانات الميكروسيزميه توفر معلومات هامة لتحسين عمليات التحفيز الهيدروليكية وما ينتج عنها من إنتاج، وتشكل الاحدثيات الميكروسيزميه الاساس للمحاكاة و تقدير حجم المنطقه المحفزه من الصخور المستهدفه.

يشكل عدم اليقين والشك في إحدثيات البيانات الميكروسيزميه في تفسير و تحليل البيانات. وقد أظهرت النمذجة المتقدمه في هذه الرساله أن إعدادات نموذج السرعة و تصميم برنامج جمع البيانات هي المصادر الاساسيه لهذه الشكوك وعدم اليقين. بناء هيكل سرعة تفصيلي هو أمر حاسم لتوكيد نموذجه أوقات وصول للاحدثيات الميكروسيزميه، و هكذا هيكل يتطلب تفاصيل كافية. اعتمادا على تفاصيل الخصائص الصخرية للمكمن، قد تحتاج الي هيكل سرعه ذو خصائص انيسوتروبكيه لتوجد تجانس بين هيكل السرعة و الخصائص الصخريه و تصحيح آثار التباين في تقدير مواقع الاحدثيات.

CHAPTER 1:
INTRODUCTION

Hydraulic fracturing is commonly employed in tight sand and shale reservoirs to initiate fracture networks and stimulate production. Typically, treatment designs are created as 2D fracture/ mechanical models to simulate the required fluid and proppants volumes to obtain optimal fracture lengths for production purposes. To assess the effectiveness of the treatment, some standard techniques are usually employed such as renewing the treatment's fracture model by matching the actual pump pressure profiles recorded during the treatment, or another method involving the borehole measurement and mapping of radioactive tracers contained within the proponents. However, such techniques do not provide sufficient information to validate the fractures model designs, and assess induced fractures geometry, which relates to stimulation effectiveness.

Microseismic monitoring and mapping of induced hydraulic fractures (frac) are important tools in unconventional oil and gas exploitation. This is a key technology for completion evaluation, which allows for continuous improved frac design, frac effectiveness, and ultimate resources recovery estimation and development. (Green et al., 2007) Shale response to hydraulic stimulation can be estimated mainly by the local density and pattern of hypocentres. Linear trends of microseismic events and their associated focal mechanisms may highlight the reactivation of faults due to hydraulic stimulation, while the location of events outside the target zone may suggest a need for adjustment to the completion/ stimulation plan, and in some cases, re-stimulation. However, errors in the hypocentre locations may convert clear trends into “fuzzy” clouds, hampering our understanding of how the stimulation interacted with the formation. The accuracy of hypocentral coordinates of micro-earthquakes is critical for understanding and proper planning for the hydraulic stimulation jobs in a shale play.

The scope of this thesis includes understanding of different source of uncertainties associated with passive seismic data processing and estimation of hypocenters. The subject dataset comprises of downhole, shallow wells, and a surface monitoring recordings that were acquired through a comprehensive microseismic monitoring network installed during the shale’s hydraulic stimulation job. Recordings include perforation shots and microseismic events produced by hydraulic fracturing. The 20 highest Signal to noise ratio (SNR) events of each stage were processed and relocated for uncertainty analysis. The processing workflow includes spectral analysis, signal enhancement, velocity model calibration, and location estimation, preceded by a full forward modeling analysis.

1.1 Understanding Hydraulic Fracturing

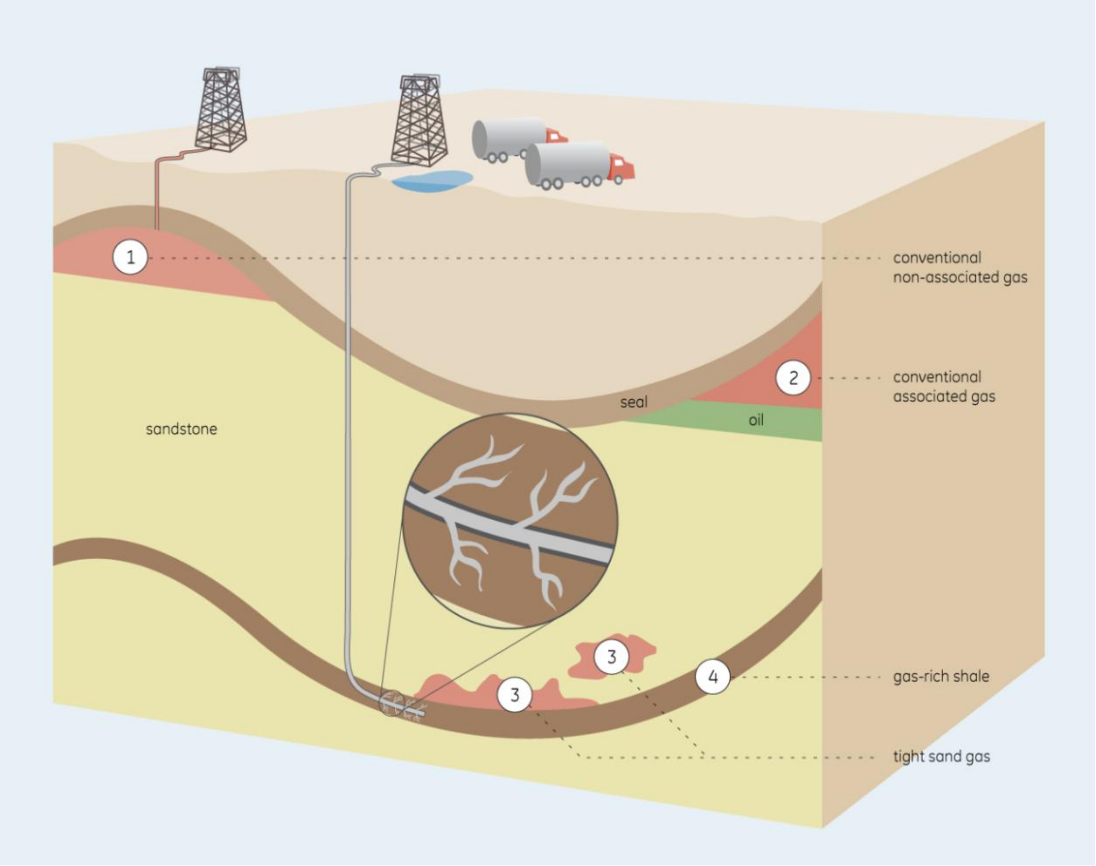

Figure 1-1: Various types of different hydrocarbon traps potential (U.S. Energy Information Administration (eia))

Conventional Oil and gas resources are developed and produced through drilling structural/ stratigraphic traps that are generally of permeable clastic or carbonate reservoirs. Meanwhile, all hydrocarbon resources locked in tight, impermeable formations like shale were considered uneconomical to produce. However, recent advances in horizontal drilling and reservoir stimulation (hydraulic fracturing) have dramatically changed that perspective. Productions of unconventional resources have changed the North America and global energy markets posture. Figure 1-1 illustrates the schematic geology of hydrocarbon reservoirs.

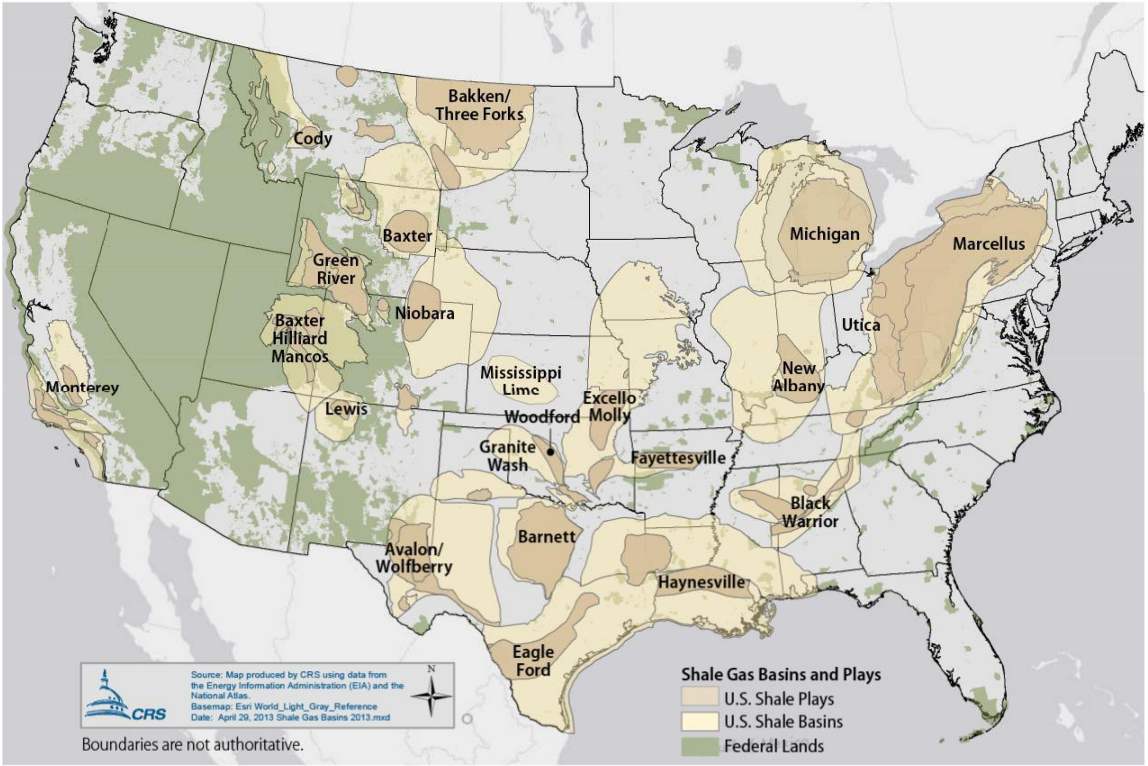

Source: Map produced by CRS using data from the Energy Information Administration (EIA) and the National Atlas.
Basemap: Esri World_Light_Gray_Reference
Date: April 29, 2013 Shale Gas Basins 2013.mxd

Boundaries are not authoritative.

Figure 1-2: United States shale gas plays (U.S. Energy Information Administration (eia))

North America is in the midst of an unconventional energy boom. Technological advancements of hydraulic fracturing and horizontal drilling have led the expansion of new shale resources development. Figure 1-2 shows shale gas plays in United States. Rapid expansion of technically recoverable shale resources was accompanied by a boom in the number of wells drilled targeting those shale reservoirs. Figure 1-3 shows the growth in number of shale wells in Marcellus shale, Pennsylvania from January 2007 to September 2010. More than 2109 wells were drilled in a period of 3 years.

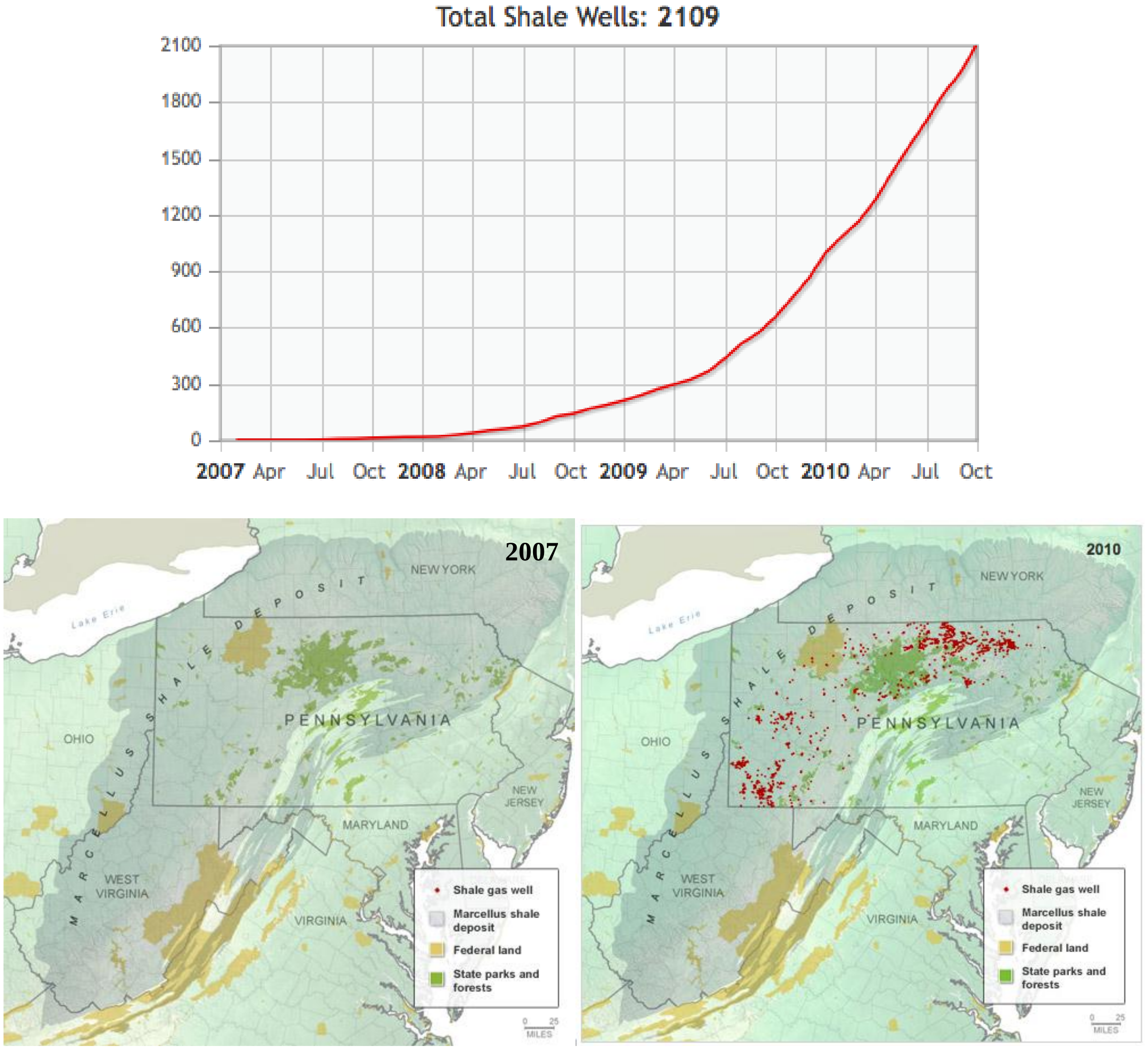

Figure 1-3: Shale wells in Pennsylvania from January 2007 to September 2010 (National Geographic)

The shale boom in North America will certainly be emulated across the world. International oil companies are already in partnership with US oil fields service companies and operators to gain access to management and technical expertise to capture the best approaches and practices to develop shale plays; and eventually apply it across the world. Even more, major service companies such as Schlumberger, Halliburton, and Baker Hughes are already spreading shale resources internationally to meet demand and tap into the world’s largest and most difficult to extract resources across the globe. Figure 1-4 shows assessed potential shale basin across the world.

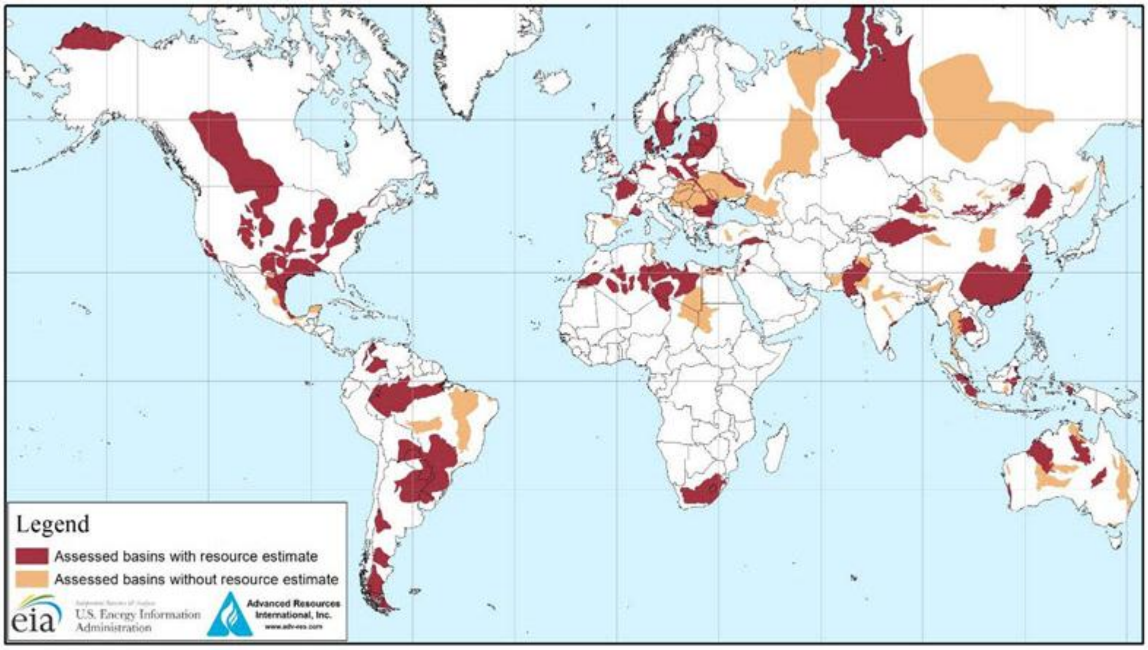

Source: United States basins from U.S. Energy Information Administration and United States Geological Survey; other basins from ARI based on data from various published studies.

Figure 1-4: Map of international sedimentary basins with assessed shale Gas and Oil formations by U.S. Energy Information Administration as of May 2013.

The term "Unconventional shale reservoir" are generally referred to a low permeability formation, micro to nano darcy rocks, that produces hydrocarbon upon stimulation. Over the past decade, hydraulic fracturing has been the technique to increase permeability and produce- ability of unconventional reservoirs. In hydraulic-fracture treatment, large volumes of fluids and proponents are injected with high pumping rates into the tight reservoirs through either vertical, deviated, or horizontal wells. Fractures initiates and propagates once the pressure of the pumped fluid exceeds the reservoir closure pressure. (Economides and Nolte, 2000) The stimulation induced fractures network acts as the pathway for the trapped hydrocarbons out of the formation. High stimulation rates could also reactivate pre-existing faults and fractures, which would enhance the induced subsurface fractures network and ultimately the productivity of the well. Figure 1-5 schematically demonstrates the fundamental steps during fracturing process.

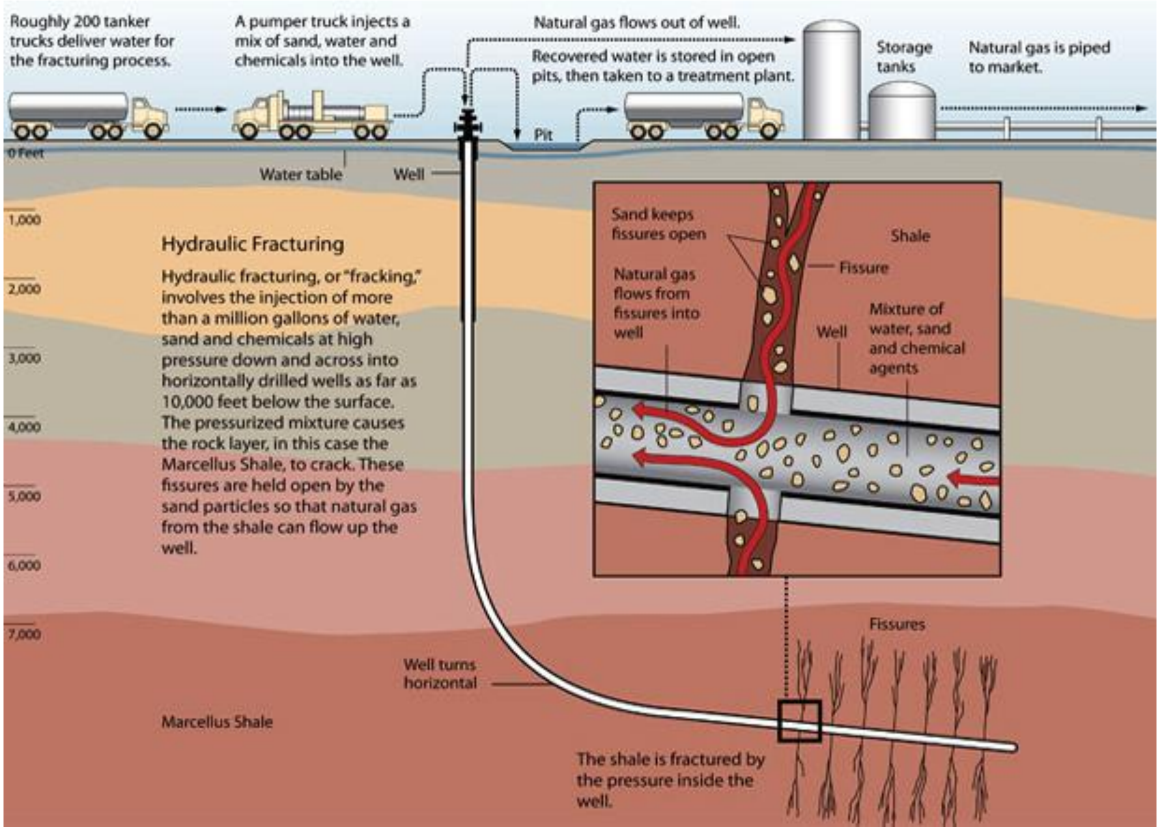

Figure 1-5: Schematic of hydraulic fracturing process (Granberg, 2010).

During Hydraulic stimulation, high fluid pressure causes the rock to fail, during which the rock behaves as a seismic source and generates small earthquakes, commonly referred to as microseisms, whose magnitudes are between -4 and +2 on Richter scale (Kendall et al., 2011). Microseismic imaging of hydraulic fracturing involves detecting micro-earthquakes associated with the induced fractures (Urbancic et al., 1999). The very small energy from the microseisms is recorded continuously by sensors placed on the surface and/or in boreholes. Reservoir dynamics can be mapped by passively listening to the earth, and recording the small magnitude earthquakes (events) caused by stress and strain changes in the reservoir. Mapping the event locations and mechanisms both in time and space at different stages of fracturing can be used to understand how the reservoir rocks response to the stimulations (Eisner et al., 2009). Analyzing microseismicity is also useful for interpreting fracture location, orientation, height, growth, length of the fractured formation (Maxwell, 2012). Additional source parameters such as event magnitude, stress and energy release, displacement of slip, orientation of fault etc., can be extracted from the microseismic events. Furthermore, moment tensor (beach ball solutions) can be determined by analyzing radiation patterns (Maxwell, 2001).

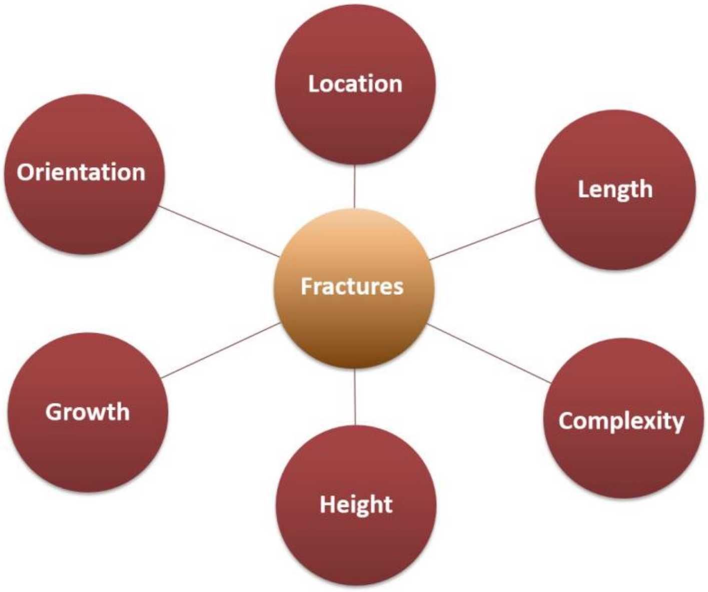

Figure 1-6: Fracture parameters can be extracted by analyzing microseismic events.

Microseismic monitoring is also a commonly used technique in CO2 sequestration projects. It helps to assess any possible seismic hazards that can be caused by injection of CO2, to map out the CO2 radiation paths and to monitor fracture network activity (Riding, 2009). Passive seismic monitoring differs from the active seismic method in various aspects. Table 1-1 shows a comparison between active and passive seismic techniques (Eisner et al., 2013).

Table 1-1: Comparison of the passive and active seismic methods.

	Passive Seismic	Active Seismic
Origin time (t0)	Unknown	Known and controlled
Seismic source location	Unknown	Known and controlled
Type of seismic source	Unknown	Known (dynamite or vibroseis)
Source Mechanism	Unknown	Uniform seismic source
Fracture type	Unknown	Generally point source assumption

CHAPTER 2:

GEOLOGICAL SETTING

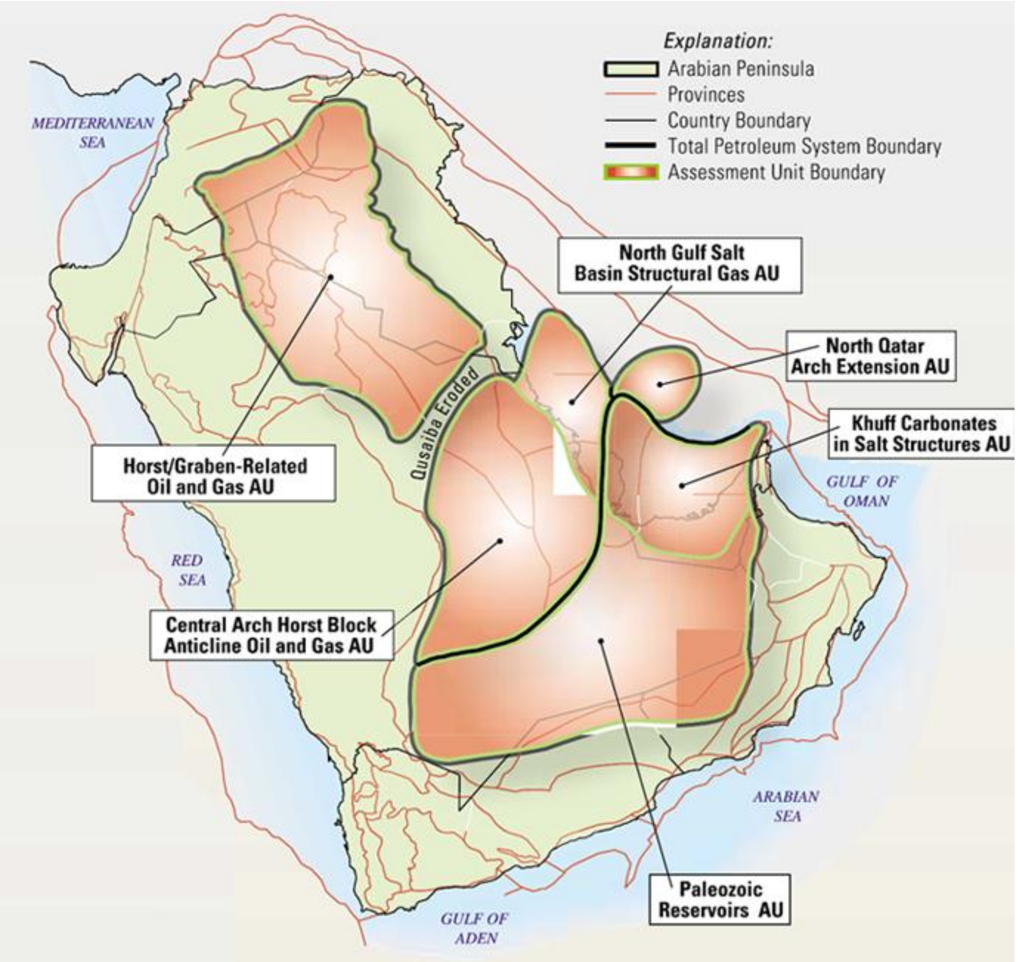

Figure 2-1: Assessment units of the Qusaiba-Paleozoic Total Petroleum Systems of the Arabian Peninsuls as described by USGS.

The target reservoir of our study is the Qusaiba hot-shale, which is the organic-rich shale interval of Qusaiba member of the Qalibah formation. Qusaiba hot-shale is lower Silurian in age, and the prolific source rock for hydrocarbons in four Paleozoic total petroleum systems of the Arabian Peninsula. Exploration efforts until recently have only focused on conventional traps for Qusaiba sourced reservoirs such as Khuff, Unayzah, Jauf, Sarah, and Qasim formations. Figure 2-1 by USGS shows six units in four regional Lower

Silurian Qusaiba-Paleozoic Total Petroleum Systems across the Arabian subcontinent. Reservoirs in the six units are mainly Permian Khuff shelf carbonates, Lower Paleozoic marine, and Permian alluvial and eolian sandstones (Evans, 1997; Aqrawi, 1998). Qusaiba-sourced conventional traps of Paleozoic reservoirs across the Arabian subcontinent are mainly salt-related structural traps, structures related to wrench-fault systems, fault-block anticlinal traps, and sediment drape over pre-existing topography. However, today the Silurian Qusaiba Member of the Qalibah formation, along with Paleozoic tight reservoirs are emerging as promising targets for shale/ tight sand gas resources in the Kingdom of Saudi Arabia.

The Lower Silurian Qalibah Formation consists of two members, the (upper) Sharawra Member and the (lower) Qusaiba Member. (P. J. Jones, 1999) The Qusaiba Member is composed mostly of claystone and shale with interbeds of siltstone and sandstone. Depositionally, the Qusaiba Member is interpreted to represent the delta-toe clays, whereas the Sharawra Member was deposited as pro-delta sandstones of an immense fluviodeltaic system that dominated the Silurian–Carboniferous of Arabia. The organic-rich and most effective hydrocarbon source-rock facies is referred to as “Qusaiba hot shale.” It is up to 75 m of hot shale with total organic carbon as high as 14 percent (Cole, 1994; Jones and Stump, 1999). It is unconformably bounded below by the Upper Ordovician Sarah Formation and above by the Lower Devonian Tawil Formation (Figure 2-2). Anoxic water conditions resulted in the preservation of organic-rich shales, which occur in most of the northern, central and eastern parts of the Arabian Plate.

Today, Qusaiba mudstones are found from the edge of the Arabian Shield eastward to the Zagros, from the Rub’ al Khali basin in the south to basins of the Levant in the north. (US

GS) Hercynian deformation modified the original depositional distribution of the Qusaiba source rock across Arabian Plate basins. This deformation eroded the Silurian source rocks from large areas over the Levant, Al-Batin, and Oman-Hadhramaut arches (Figure 2-1). Two major anoxic basins are recognized; Faydah-Jafurah to the south and Nafud-Ma’aniya to the north, with their northeastward extensions to the Zagros suture (Figure 2-1). One depocenter was located in central and southern Arabia, and the other depocenter in northwestern Saudi Arabia. The widespread erosion of the Silurian source rocks over these arches limited the Paleozoic hydrocarbon potential to the margins of the Hercynian basins (Faqira et al., 2009).

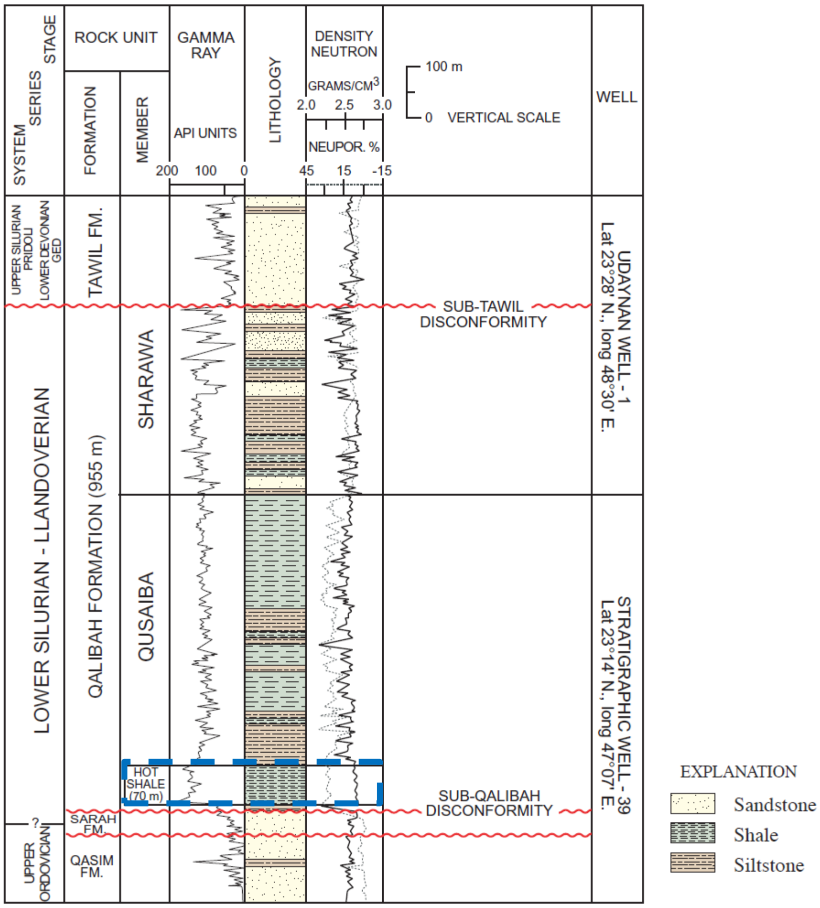

Figure 2-2: A Subsurface reference section of the Qalibah formation in central Arabian Peninsula. Hot shale is labeled with a blue box. (USGS)

The Qusaiba hot shale, across the eastern Arabian subcontinent, is mostly thermally mature for gas generation; however, the Qusaiba is overmature for gas generation in the deeper parts of some basins, and mature for oil generation along some basin margins. A study was conducted by (Cole, 1994) to assess the organic richness of the Qusaiba Member. Geochemical data, such as TOC, hydrogen index (HI), and normalized iron:sulfur:carbon ratios (Cole, 1994; Cole et al., 1994b) were used to assess the organic richness of the Qusaiba Member throughout the study area. These measurements, which were derived mostly from core samples, were used by (Cole, 1994) in Figure 2-3 to plot the gamma-ray response and organic richness (TOC) of typical Qusaiba Member source rock facies in two typical wells. The work has demonstrated this relationship established relationship between gamma-ray response level and organic richness. Previously, it had been shown (Beers and Goodman, 1944) that for marine depositional settings there is commonly a correlation between zones with high levels of organic richness and high radioactivity (i.e., high gamma-ray response), which is caused primarily by an increase in uranium content in the sediments (Meyer and Nederlof, 1984). The Qusaiba Member was deposited in marine settings and, therefore, should exhibit an association between high gamma ray response and high levels of organic richness.

In most Qusaiba Member penetrations in Saudi Arabia a cutoff value of 150 API gamma-ray units distinguishes potential source shale from non-source shale. The relationship between gamma-ray response and organic enrichment was used to geochemically interpret wells that lack cores from the basal Qusaiba Member. Thus, even in wells where only samples of drill cuttings were available, the gamma-ray response could be used to more accurately determine what total thickness should be considered source rock quality

(TOC> 2%) sediment. The source rock facies of the Qusaiba Member is confined almost entirely to the basal part of the lower Qusaiba Member. The thickest Qusaiba Member hot shale lies east of the Qalibah trough.

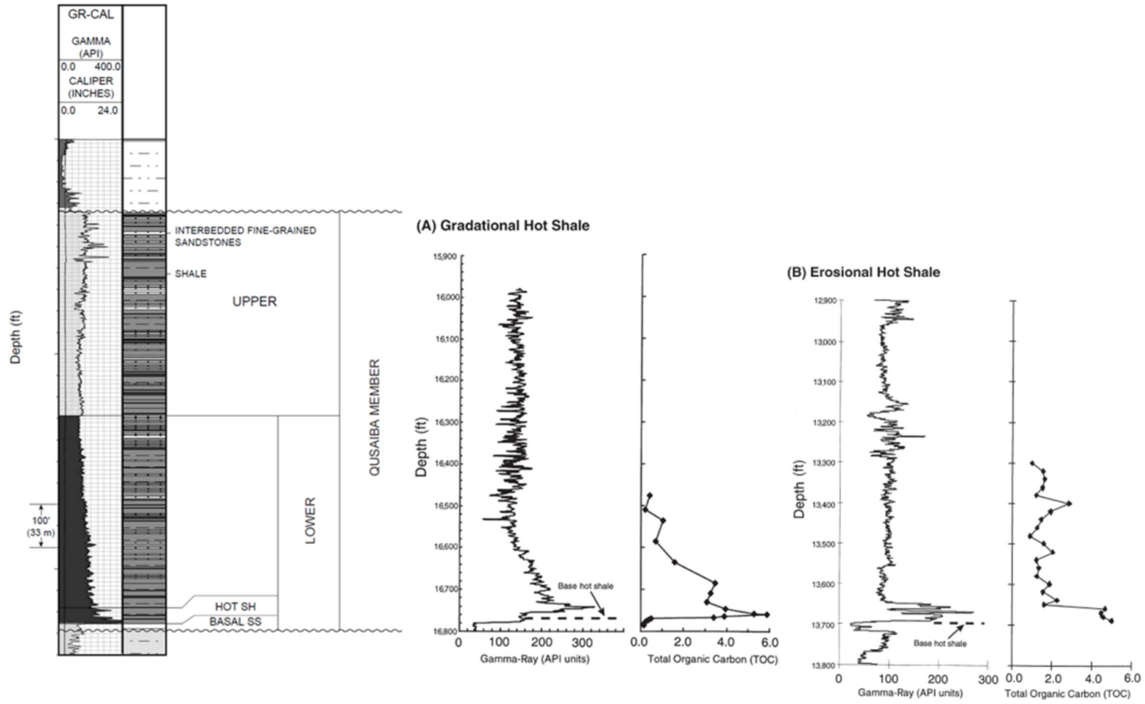

Figure 2-3: Subdivisions of the Qusaiba Member, Qalibah Formation on the left column. On the right, gamma ray response and total organic carbon (TOC) vs. depth for Quasaiba sections that exhibit (A) typical graduational and (B) erosional contacts with overlaying units that contain coarse clastic innerbeds.

CHAPTER 3:
MICROSEISMIC REVIEW

Passive seismic monitoring application covers a number of different settings and is almost hundred years old. In 1910, a horizontal seismograph was installed over a gold mine in Witwatersrand region of South Africa to monitor mining associated tremors. (Gane et al., 1946) Though the observed tremors hypocenters were unknown, their activity and intensity increased over the years as did the rate and depth of mining operations. 30 year later, 5 mechanical seismographs were deployed, and seismologists concluded, through calculated hypocenters, that indeed the tremors originate from the mine. (Gane et al., 1946) From these humble beginnings, extensive microseismic arrays are now a standard for monitoring operating mines. (e.g., Gibowicz and Kijko, 1994)

Microseismicity has also been used to monitor fracture propagation during fluid injection in hydrocarbon reservoir since mid-1900s (Phillips et al., 2002). In the late 1960's in Denver, Colorado, Evans (1966) and Healy et al. (1968) showed that injection of high-pressure fluids triggers minor earthquakes. Fluid injection, or extractions from subsurface reservoirs, initiate fractures and change local stress distribution, which would trigger microseismic events. Mapping the induced fractures and stress changes has been of a considerable interest in Oil and Gas industry (e.g., Evans, 1966; Healy et al., 1968; De Meersman et al., 2009; Verdon et al., 2009; Maxwell, 2009; Dyer et al., 2010).

Microseismic has emerged as a common fracture diagnostic tool to image induced fracture-networks that accompanies oil and gas operations. The growth is attributed to the success of induced fractures imaging in the Barnett shale, and the value and implications of such information on the hydraulic stimulation designs and ultimately well productivity. Though today, most common application of microseismicity is induced hydraulic fracture monitoring, it is also used for thermal processes monitoring, reservoir production surveillance, and other applications in hydrocarbons and mining industries (Maxwell, 2009).

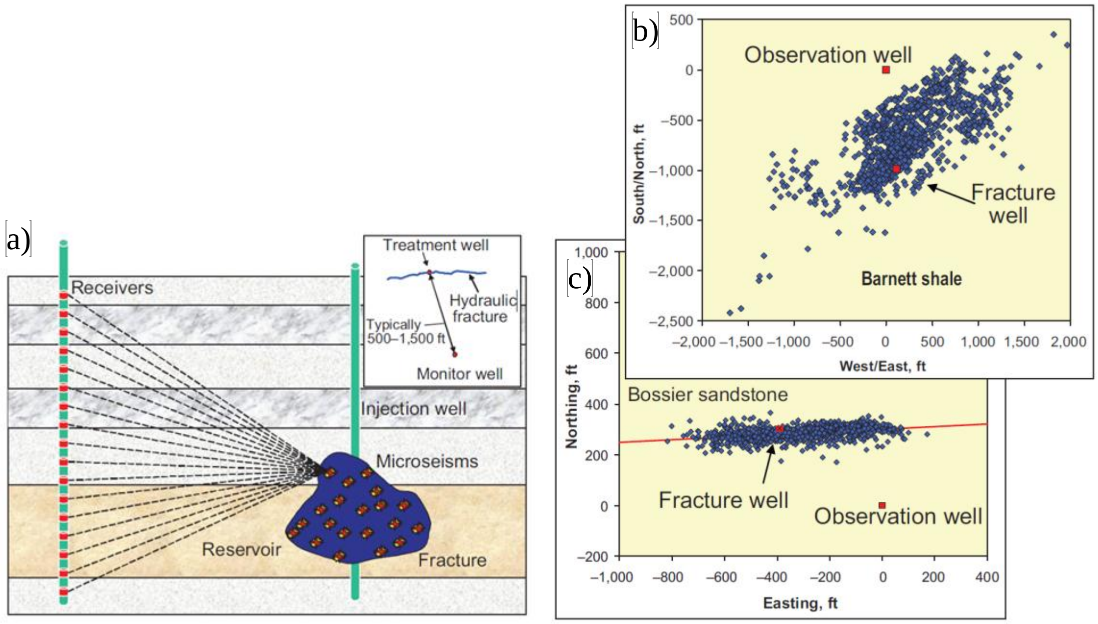

Figure 3-1: a) A typical downhole monitoring geometry of a vertical frack b) map view of the located microseismic events of a frac job in the Barnett shale and c) Bossier sandstone each with a different fractures growth pattern (Fisher et al. 2005)

The microseismic monitoring process requires a monitoring well at a relatively close distance to the main borehole and a receiver array vertically as close as possible to hydraulic fractures zone (Figure 3-1). Vertical and horizontal positioning of the receiver array is critical as there is a maximum monitoring distance, due to the amplitude decays of the microseismic signal with distance. When the amplitude falls below the level of the background noise, it cannot be measured anymore.

A well-designed microseismic survey can provide information of the induced hydraulic fractures properties and behavior, such as fractures height, length, dip, azimuth, asymmetry, and complexity. Understanding fractures helps to optimize frac job design and play development at the long run (Warpinski, 2009).

3.1 Application of microseismic

Microseismic is used to yield spatial and temporal plots of the development of fracture creation and reactivation. (Stein, 2003) It has been a growing technology for hydraulic fractures mapping and reservoir monitoring. The concept of microseismic process has grown out of standard earthquake seismology principles, which describe earthquakes and the propagation of elastic waves through the earth.

Microseismic monitoring is the placement of receiver arrays in a systematic position to record the microseismic emissions created by the hydraulic fracturing process. Detected microseisms provide information about the geometry and properties of the induced fractures. The hypocenter location is an inverse problem where the data are arrival times recorded by receiver arrays at defined positions, and the unknowns are the spatial coordinates (x, y, z) and the origin time, t0, of the microseism event (Stein, 2003). Hypocenter locations are determined from the observed arrival time differences between P and S waves, assuming a known velocity model. The computed hypocentral locations of the emissions may be used to produce 4D time-lapse images of fracture growth. Hypocenters are usually calculated without a corresponding uncertainty estimation, which may let the uninitiated to believe that hypocenter locations are very precise.

3.2 Noise Challenge:

Microseismic events are generally very weak signals. Any source of noise can ruin their recording. Noise is any kind of acoustic energy that could interfere with the desired signal. It can be either coherent or incoherent noise; coherent noise is more systematic in its behavior and tends to have a certain well-defined frequency ranges. Incoherent noise is a more challenging type; it is random in nature and can be triggered by any local phenomena related to the ongoing work, as drilling mud pumps or pipe mounting, or even within the borehole such as nearby drilling of the same formation, gas bubbles, some pad drilling, or wind on the wireline. Due to the random nature, each geophone could experience a different set of noise signals both at surface and downhole. Noise related effects can be controlled by filtration or avoidance. Avoidance is the ideal option as much of the noise tends to fall in the same frequency range as the microseismic events (Warpinski, 2009).

3.3 Acquisition Geometry

Microseismic monitoring systems include a number of different possible sensor configurations. Sensors are continuously monitoring passive seismic activities, in various ways (Figure 3-2) either in an observation well or on surface, depending on requirement and scope of the job. Borehole arrays are the most common monitoring system, followed by the surface array deployment.

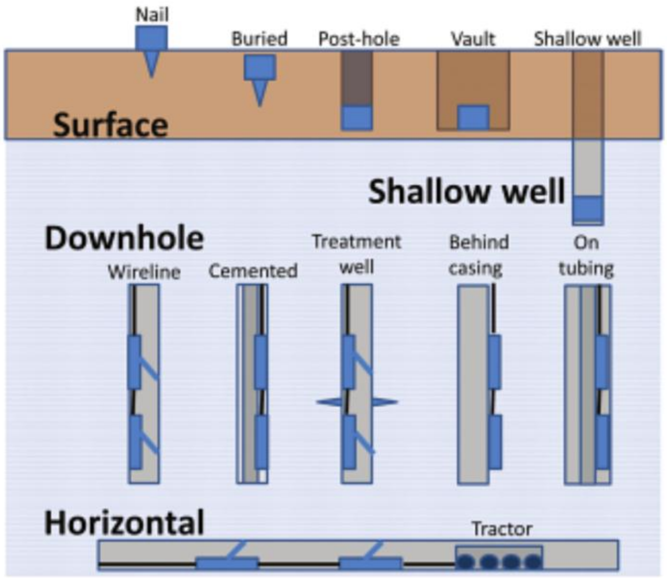

Figure 3-2: Various deployment scenarios in different configurations. (Maxwell, 2014)

Borehole array can be deployed via wireline as used for VSP or crosswell seismic, or cemented in shallow or deep observations wells (Smith, 2010). Wireline arrays are usually installed in a near vertical borehole or through a wireline tractor in horizontal wells to pull the array across the lateral section. Alternatively or in combination, an array can also be deployed on surface as used for earthquake monitoring or reflection seismic surveys. (Duncan and Eisner, 2010) Surface array sensors can be broadband seismometers as in earthquake monitoring or typical reflection seismic geophones, the sensors can be deployed in radial lines away from the treatment wellhead or following gridlines (crosslines) or in 2D patches over the treatment well (Pandolfi et al., 2013) Extensive microseismic monitoring network of single and three-component geophones is recommended. Integrated monitoring networks of surface and borehole arrays allow for more advanced processing of the data such as determining source mechanisms, tomographic imaging and shear wave splitting analysis. (e.g., Young et al., 1992)

3.3.1 Downhole monitoring

Borehole deployment is the most common technique for passive seismic monitoring in the oil and gas industry. In downhole monitoring, high sensitivity sensors are deployed in a vertical, near vertical, or horizontal boreholes, or even in multiple wells simultaneously (Warpinski, 2009). Most downhole monitoring is done through an offset observation well; treatment well deployment is not as common due to the increase in background noises resulting from the fluid pumping through the same borehole. (Gaucher et al., 2005) Observation wells are usually existing production wells with open perforations and used temporary for monitoring purposes; in preparation for arrays deployment any production tubing would be removed, and a hydraulic isolation packer would be installed above the shallowest perforations to isolate for safe well operations and quite monitoring conditions.

Preferably, the observation borehole should be located in close proximity to the seismic sources minimize attenuation, and enhance single to noise ratio. (Maxwell, 2011) This will allow detecting small-magnitude microseisms with a sufficient signal to noise (S/N) ratio to calculate source locations. Proper positioning of the microseismic array is the main issue for a successful result, including both horizontal and vertical distance to the monitored zone. The optimum vertical positioning is to have the array at the same depth as the fractures zone, which may not be possible due to borehole drilling issues, or because of access limitations and near-surface conditions. Monitoring still can be carried out effectively from a higher vertical position, but interfering scattering and noise will accumulate with distance. Shallower position usually increases complexity by adding more layers with different properties. Finally, the microseismic signal decreases with distance from the source, yielding a lower Signal/Noise ratio. A dominant factor for amplitude decrease is the geometric spreading G, which is described by the function: G=1/R (where R is the receiver distance from the source). Anelastic attenuation may be relevant too in some formations. In some cases, as for the Barnett shale, positioning receivers at a higher level is a meaningful option, as it can often result in simpler seismic waveforms, and minimal refracted energy.

The number of sensors in borehole arrays has increased over the years, early experimental work used a single 3C sensor. Later in commercial applications, the arrays developed from several levels to up to hundreds of sensors in modern monitoring projects. The tools' configuration is a critical aspect of the monitoring process; it has to provide the required optimum receiver aperture, as precise location estimation of the microseismic source requires sufficient triangulation. Too large an aperture must be avoided because microseismic events might not be detectable at far distances, and it adds some structural complexity due to lateral velocity variations. A good monitoring program would have an efficient tools configuration close enough to the microseism source with wide enough apertures for acceptable triangulation (Warpinski, 2009).

3.4 Concept of downhole data processing

The main concept behind microseismic imaging is the use of recorded information to estimate location, timing, and mechanisms of the induced microseismic events. The data can be used to make inference about the changes that accompany injection into or production from a conventional reservoir, or as fracture diagnostic tool for unconventional reservoirs.

Processing of the downhole microseismic data involves detection of an event, determination of the Primary (P) and Shear (S) waves' arrival time, and analysis of the phases (Quirein, 2006). The microseism's Primary (P) and Shear (S) waves can be detected and utilized for location calculation. The microseism's source location is found from the arrival times of the Primary (P) and Shear (S) waves marked "+" on Fig.2 for the HX-component of the waveform below:

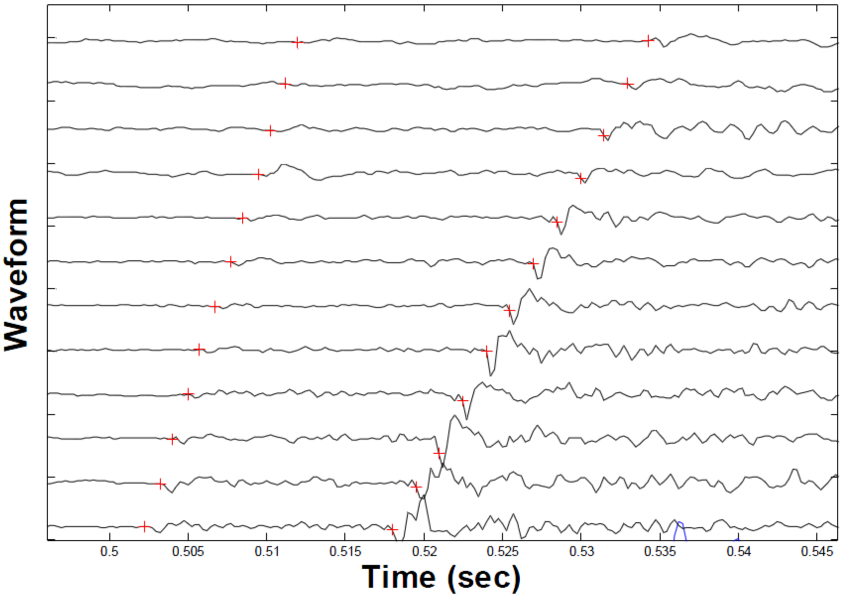

Figure 3-3: Seismogram for a microseismic event occurring below the receivers (bottom up moveout). First arrivals are the P waves. The S waves generally have the greater amplitude. (Quirein, 2006)

Assuming an isotropic homogenous medium, the basic equation relating distance, velocities, and time is simply:

$$d_i = V_p(T_{pi} - T_0) = V_s(T_{si} - T_0) \qquad \textit{Equation 3-1}$$

d_i is the distance from the source of the microseism and the ith geophone, T_0 is the time of origin of the event, T_{pi} is the arrival time of the (P) wave at the ith geophone, Ts_i is the arrival time of (S) wave at the i-th geophone, V_p is the primary (P) velocity, and V_s is the shear (S) velocity.

From Equations (1) we get:

$$Vp(Tpi - Tpj) = (di - dj) \qquad \textit{Equation 3-2}$$

$$di = (Tsi - Tpi)/(1/ Vs - 1/ Vp) \qquad \textit{Equation 3-3}$$

Equation 2 indicates that the difference of the distance between event I and J is directly proportional to the time difference of P arrivals at geophone I and j. Equation 3 indicates that d_i from an event to the i-th geophone is proportional to the time difference between the S and P arrivals, $T_{si} - T_{pi}$. Equation 1 can be rewritten to represent the distance for all receivers by accounting for the radial distance and the true vertical depth (Mandel 2000) based on the monitoring geometry.

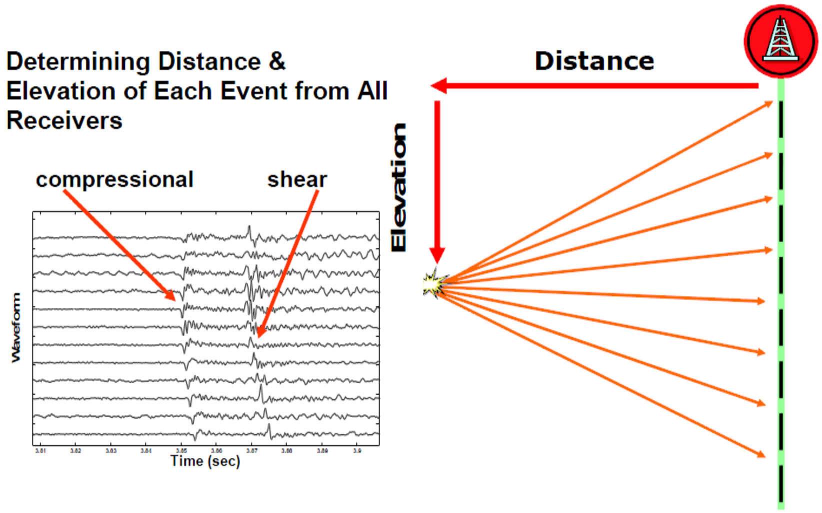

Figure 3-4: The P and S arrival times from all receivers can be used to determine the radial distance of the event from the monitor well, along with the true vertical depth of the event. (Quirein, 2006)

In an homogenous medium, P wave direction (after geophone spatial calibration) is in the direction of travel of wave and it is indicative of the point of orgin azimuthal direction

(Warpinski, 1998). Direction is determined by a cross-plot of the 3 components of the recorded seismograms, called "hodogram", as shown in Fig. 3-5 below:

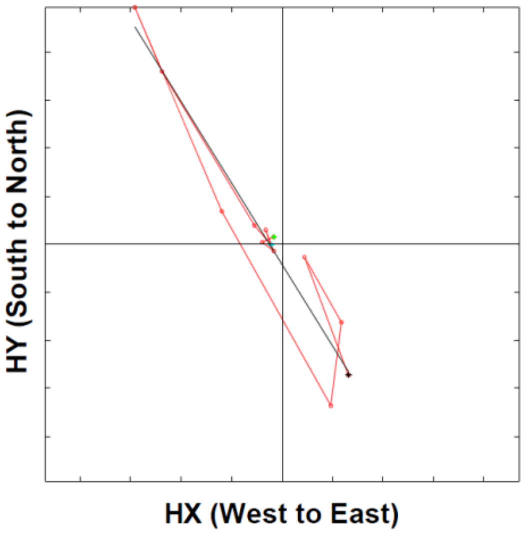

Figure 3-5: Hodogram of HX and HY waveform conponents. Blak line determines the best-fit line to represent the direction of an event from the monitor borehole. (Quirein 2006)

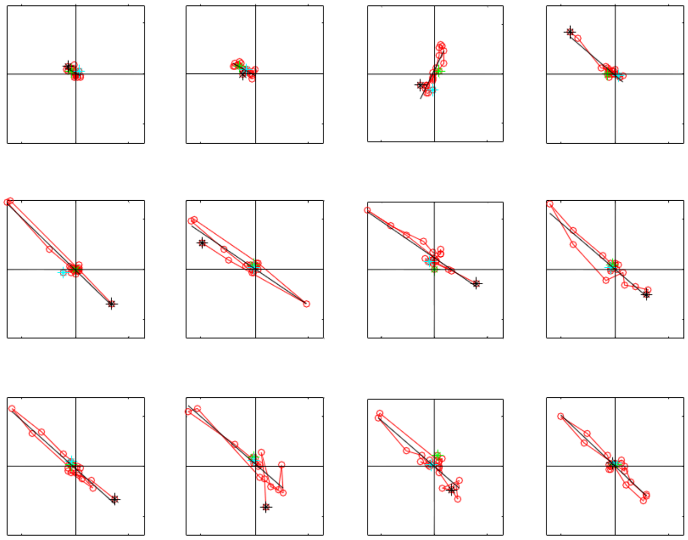

Figure 3-6: Hodogram waveform for all geophone of the event decpicted in Fig. 3-4 (Quirein, 2006)

Hodograms tend to be more representative when the geophones "straddle" the event rather than being below or above the event. It is important to be selective while processing the data as some geophones are "disoriented" during monitoring. A good approach is to cross-plot the median of the microseism azimuth predicted by hodograms against the hodograms correlation coefficients, as in Fig. 3-7 (John A. Quirein, 2006).

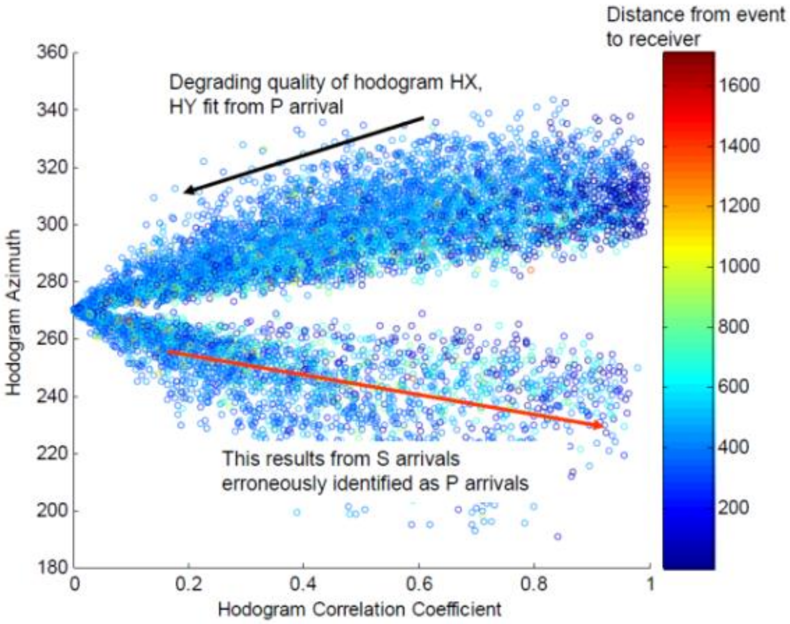

Figure 3-7: Calculated azimuth from hodogram versus hodogram correlation coefficient for all recoreded microseism from all receivers. Color coded with distance from a source event to receiver as obtained from equations 3-2. (Quirein, 2006)

The lower part of the figure is a consequence of an error in the automatic event locator, which often identifies S arrivals as P arrivals. From the monitoring geometry it is impossible for any event azimuth to be less than 270 degrees (Quirein, 2006).

3.5 Velocity structure uncertainty

Microseisms locations uncertainty and fracture geometry are critical in hydraulic fracture monitoring. Location uncertainties are more complex in anisotropic shale reservoirs. The estimation of uncertainty is not a simple calculation as there is random uncertainty associated with data quality and a systematic uncertainty associated with the velocity model errors. (Maxwell, 2011) The velocity model is a critical element of microseismic image processing: even if all components are optimum, an inaccurate velocity model can lead to few hundred feet off in hypocenters locations. In many cases, it is initially derived from dipole sonic logs, where from high-resolution primary (P) and shear (S) velocities can be obtained. These velocities do not fully describe the subsurface as they are vertical velocities close to the side of the borehole at the time of drilling. The wellbore could be non-competent due to drilling mud invasion, or several other disturbing factors. The correct velocities tend to be different relative the log derived velocities, a subsequent step to overcome these problems is to adjust the velocity model based on a known source position such as perforation or string shot. These measurements will not provide velocities across the specific path of the microseism, nor will provide information about the different geological layers.

Although calibration shots can provide sufficient accuracy, this method does not allow for the anisotropic nature of geological formations, which is especially relevant to shales. Thomsen’s anisotropy parameters for all geological Intervals must be known to account for it. (Thomsen, 1986) Lateral velocity changes could also be due to lithological variations and geological features such as pinchouts and faults, which would have a major impact on the event location results. Vertical velocity, however, may be accurately measured by dipole sonic. (Warpinski, 2009)

CHAPTER 4:

MICROSEISMIC MONITOIRNG CONFIGURATION

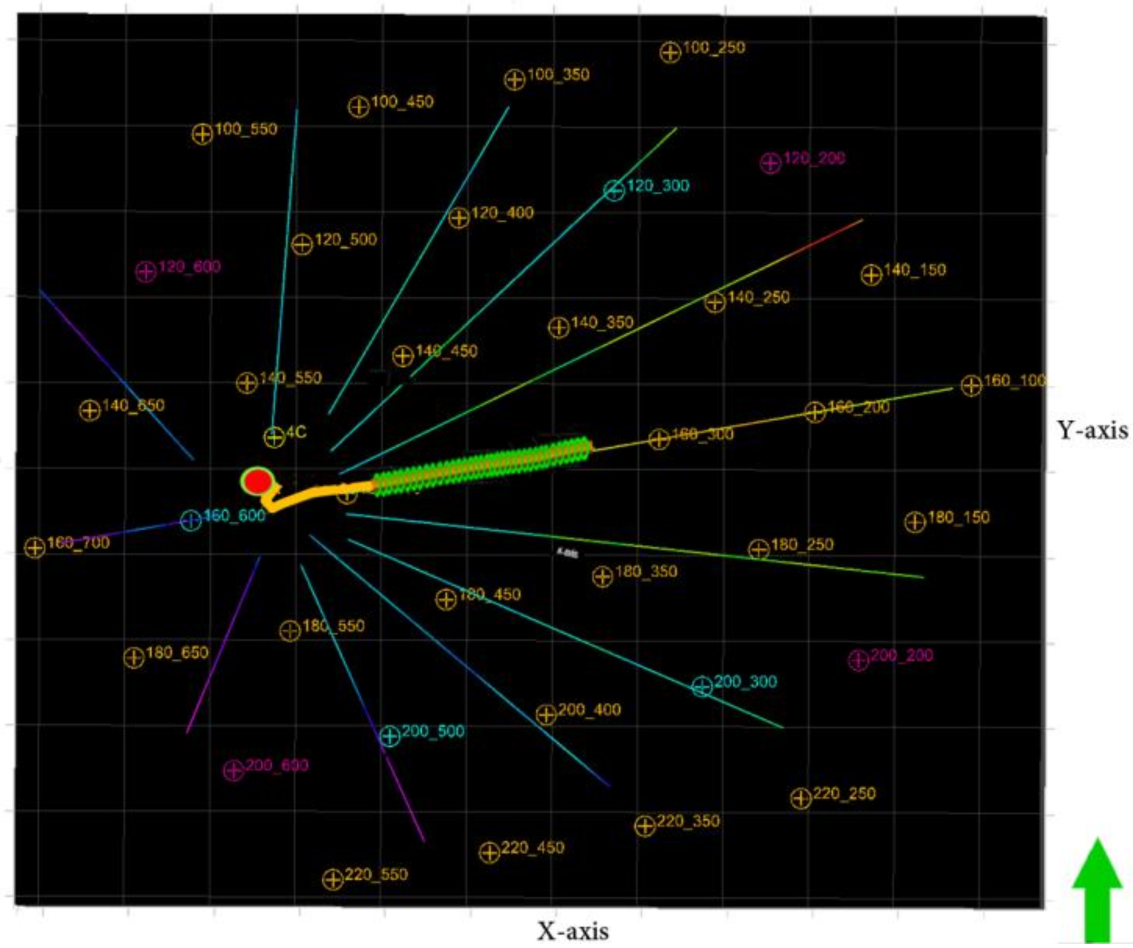

Figure 4-1: Schematic showing the recording geometry of the subject monitoring campaign. The plane view map highlights the receivers at the Earth surface geophones by colored seismic recording lines, and buried array are marked by crossed circles in orange, cyan and magenta color with the last three digits of the borehole names representing the total depth. Also, the projection of the vertical borehole in red, and the perforation shots in green.

The data used in this research thesis project is a Microseismic dataset recorded through a comprehensive monitoring campaign for hydraulic fracturing operations of horizontal shale well in the Arabian Peninsula. The treatment plan consists of 12 stages “Plug and Perf” technique, the monitoring campaign is composed of a downhole array, shallow wells array and surface sensors. The three deployed monitoring systems consist of 12 seismic lines of multi-component geophones at the surface; a grid of multicomponent geophones cemented in 37 shallow vertical wells and a 12-level 3C borehole array in the nearby deep monitoring well. The systems acquired the data independently, but were synchronized by GPS satellite time stamp to allow full data integration. Figure 1, shows the configuration of the entire monitoring program.

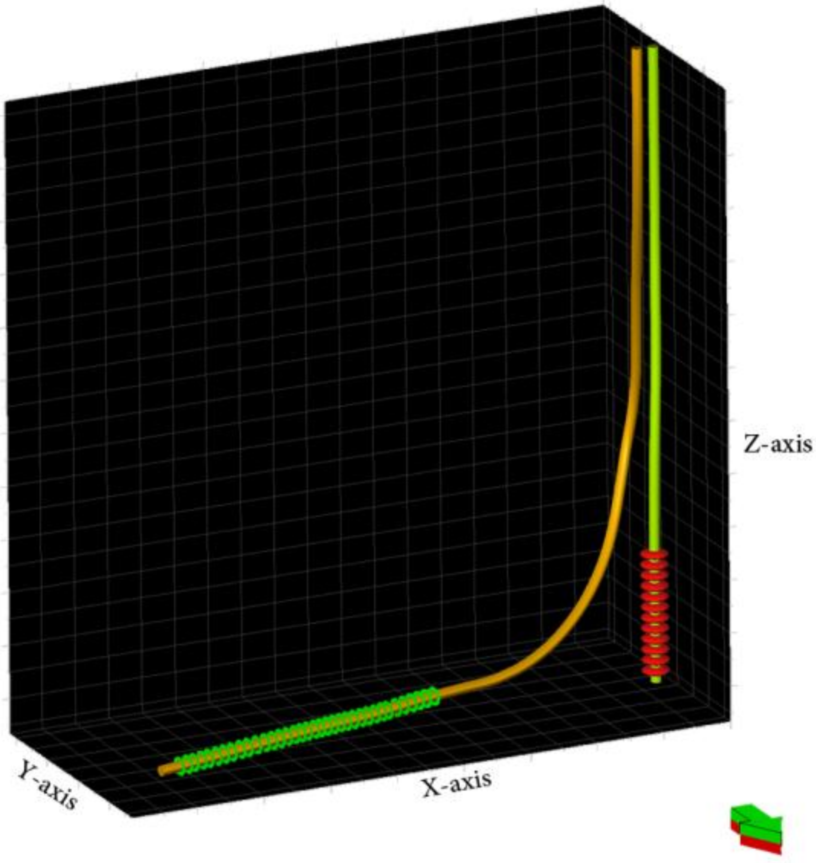

Figure 4-2: The receivers are in the main borehole are depicted by red circles and the location of the perforation shots by green circle

4.1 Shallow Wells Grid

The grid is composed of 37 shallow monitoring wells equipped with 469-cemented geophones. The boreholes were of different depths; there were 27 shallow wells of 200ft, 4 shallow wells of 300ft, and 5 shallow wells of 600ft depth (Figure 4-2). The geophones were grouped into 277 stations, 189 single vertical geophone and 91 3-C geophones. Recorded raw SEGD data included continuous monitoring of 12 frac treatments (stage 1 to stage 12) and monitoring during plug setting & perforation gun firing (3 clusters for each stage).

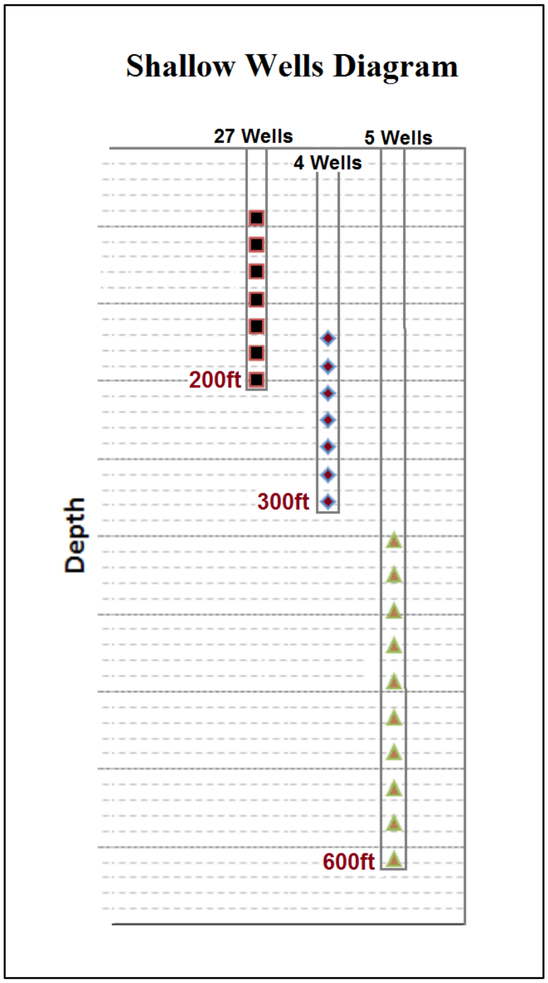

Figure 4-3: The locations of the geophone stations in the 200ft, 300ft and 600ft wells are plotted with the relative depth from the well head. Overall the sensor arrays sample any seismic signal propagating in the subsurface between 20m and 182m (60ft and 550ft) depths.

4.2 Surface Array

The array consists of 12 lines of a total length of 71560ft (gray lines on Figure 4-3). A seismic recording system was used to acquire 5378 surface geophone channels, 3590 stations were grouped into 2696 1–C geophone stations and 894 3-C stations were deployed along the 12 seismic lines. The recorded data included continuous monitoring of 12 frac treatments (stage 1 to stage 12) and monitoring during plug setting & perforation gun firing (3 clusters for each stage).

In addition, 3C surface patches, consisting of a regular grid of 7x7 3C surface geophones, were deployed above the stimulated section of the S-100 lateral.

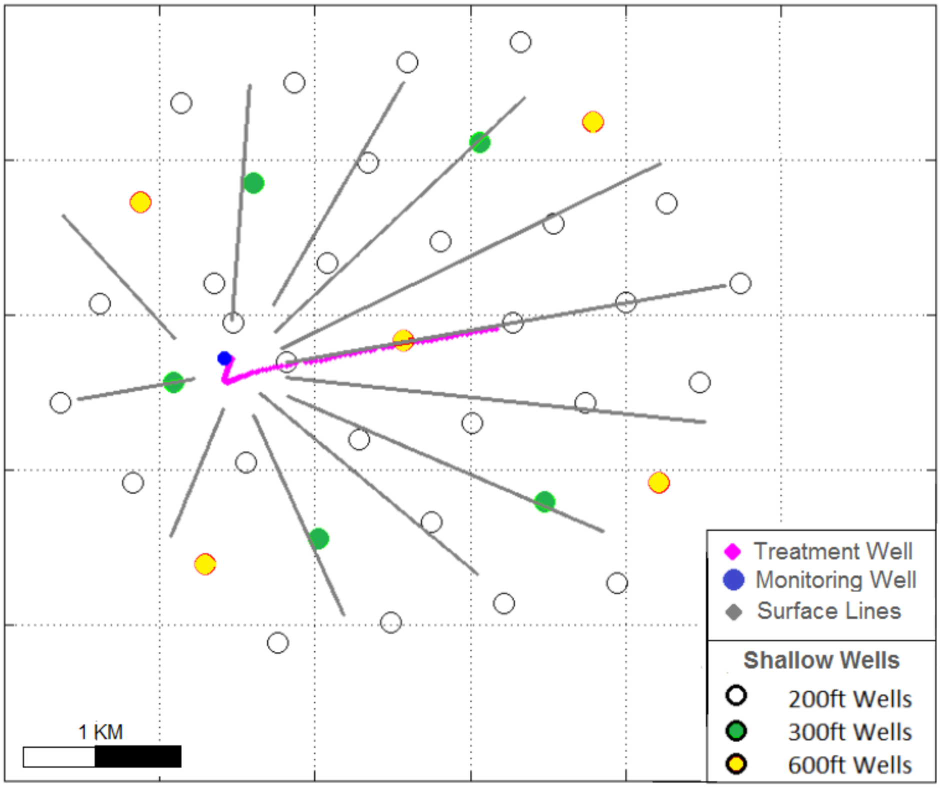

Figure 4-4: Complete map of the monitoring systems deployed for monitoring the treatment of ST-51A_L2. The well head locations are mapped and indicated in the legend. The grey lines are the surface seismic lines. The S10 well, trajectory is indicated in pink and at the center of the figure, is the treatment that was stimulated.

4.3 Downhole Array

Downhole array consists of a 12-level downhole string with 100ft spacing configured for continuous data acquisition at 0.5 millisecond sampling rate. Downhole tool was deployed in the monitoring well to record the 12 frac treatments (stage 1 to stage 12) and the plug setting & perforation gun firing (3 clusters for each stage). Figure 4-4 shows the monitoring well geometry relative to the treatment well.

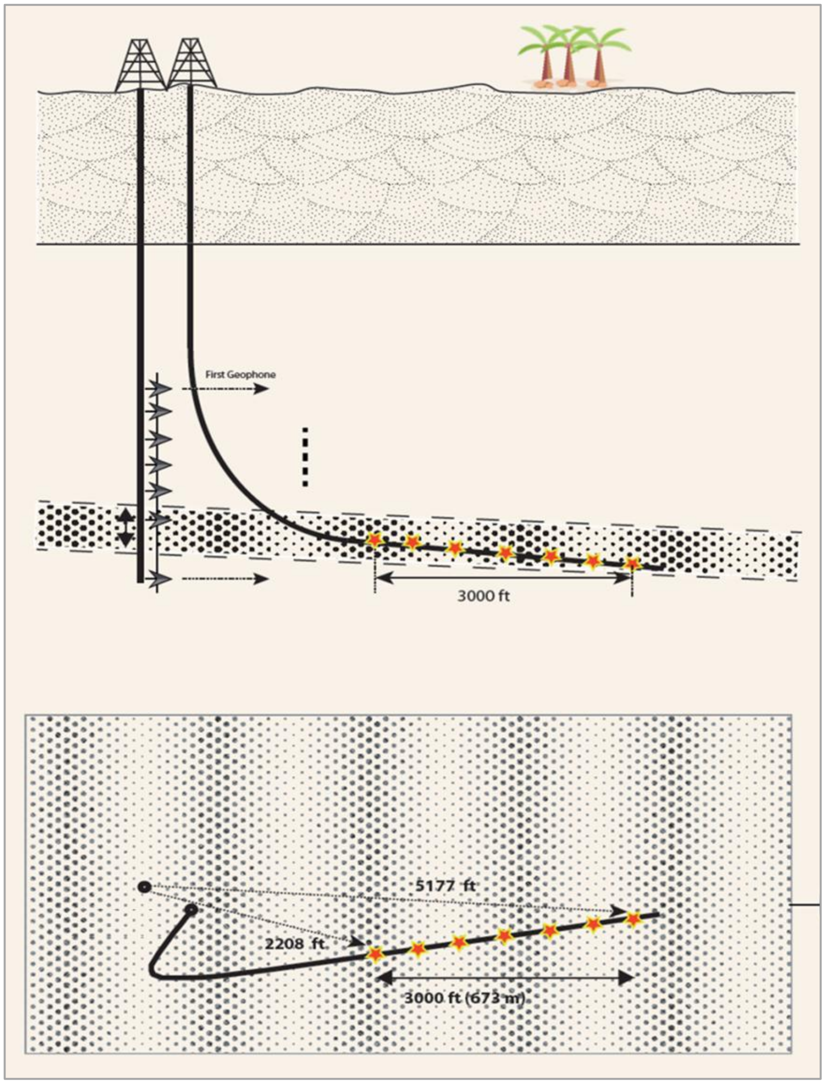

Figure 4-5: A display showing the downhole monitoring system configuration and dimensions. A) X-section showing the geophones and monitoring well relative to the target formation and the treatment well. B) Map view of the treatment well lateral section and proximity to the monitoring well.

Table 4-1: A summary of the specification of each system is provided in the table below.

Microseismic acquisition systems summary	
Surface	
12 seismic lines	Each has a 3C station every 4 standard vertical geophones.
Surface Patch	A regular 2D grid of 7x7 3C stations.
Borehole Shallow	
27 Shallow wells 200 ft	Array length is 42 m with 7 m spacing between levels.
4 Shallow wells 300 ft	Array length is 42 m with 7 m spacing between levels.
5 Shallow wells 600 ft	Array length is 82 m with 9.1 m spacing between levels.
Borehole	
VSI 12 – levels	Array length is 1200 ft with 100 ft spacing between shuttles.

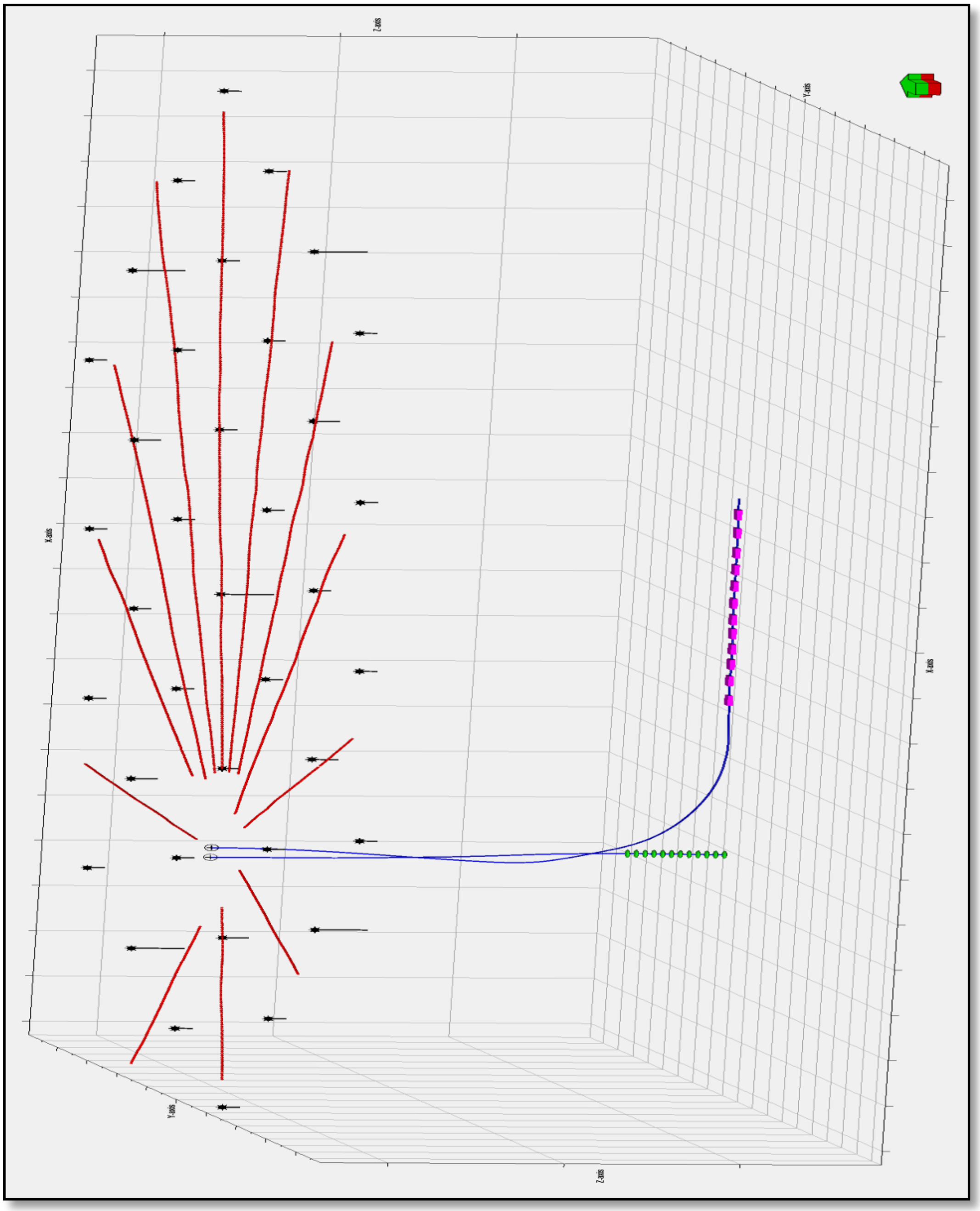

Figure 4-6: view of the comprehensive monitoring system. Downhole geophones are labeled in green. Treatment stages are labeled in purple. Surface seismic line labeled in red. Shallow wells array are labeled in black. Monitoring well and treatment well labeled in blue

CHAPTER 5:
FORWARD MODELING

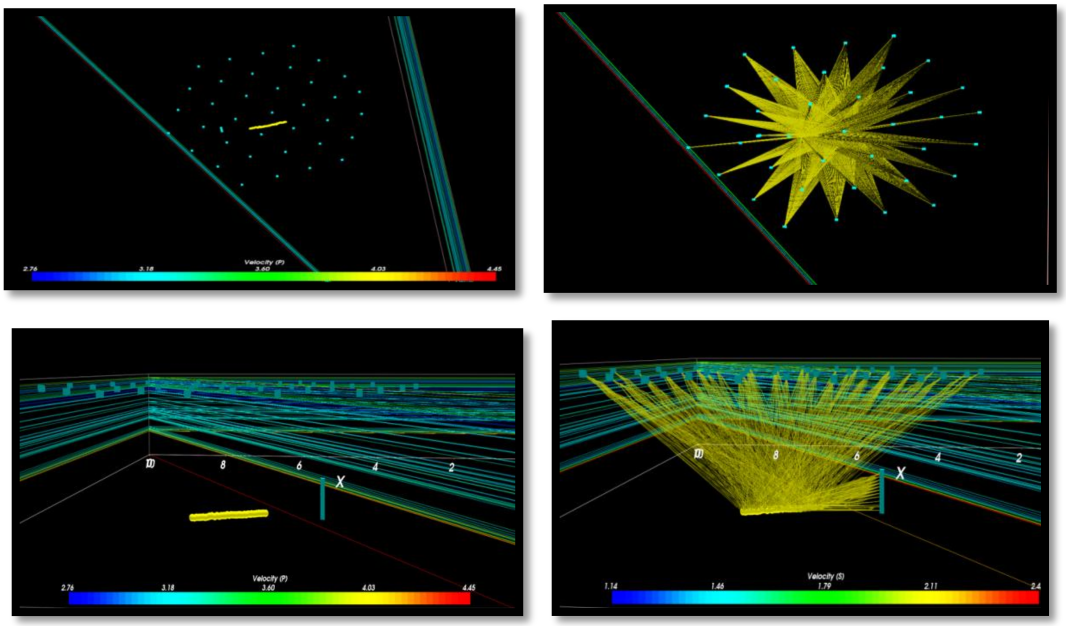

Figure 5-1: Lateral and plane view of the rays traced from both surface and borehole receivers to the perforation shot locations along the horizontal part of the well. Receivers are indicated by blue dots, sources by yellow dots.

We model the travel times in a 3D structural velocity model, which reflects the general geological structure over the target well for stimulation. Then, compare calibration shot (perforation shots, or string shots) observed arrivals times (events), and modeled arrival times. In this way, we can estimate the relocation error based on the adopted velocity model and function parameters. The goal is to compare the accuracy, and precision between different recording geometries for microseismic recording experiment. Fermat's based ray tracing method (Cat3D), and Hypo3D were used for the forward modeling exercise. We constructed two different velocity models, and three different microseismic monitoring configurations. One simplistic velocity model of 12 Layers, and a more complicated velocity model of 62 layers based on Vp, and Vs curve blocking, and the monitoring configuration includes surface only, downhole only, and surface and downhole arrays.

5.1 Fermat's Based Ray Tracing Method

Pierre de Fermat

The time arrivals calculations for forward modeling exercise for this project were done through Fermat's based ray tracing techniques, using a method published by Vesnaver (1996). The method trace rays in an irregular grid based on Fermat's principle of minimum time. Fermat's principle or the principle of least time states the ray path between source and receiver must be of the least travel time, in other words the acoustic energy would travel between any two points along a path where the first-order variation of all nearby paths is zero. Since first arrivals and primary reflections are the focus, the formulation can be restated and simplified by considering ray paths as trajectories for seismic energy to travel from source to receiver. (Vesnaver, 1996)

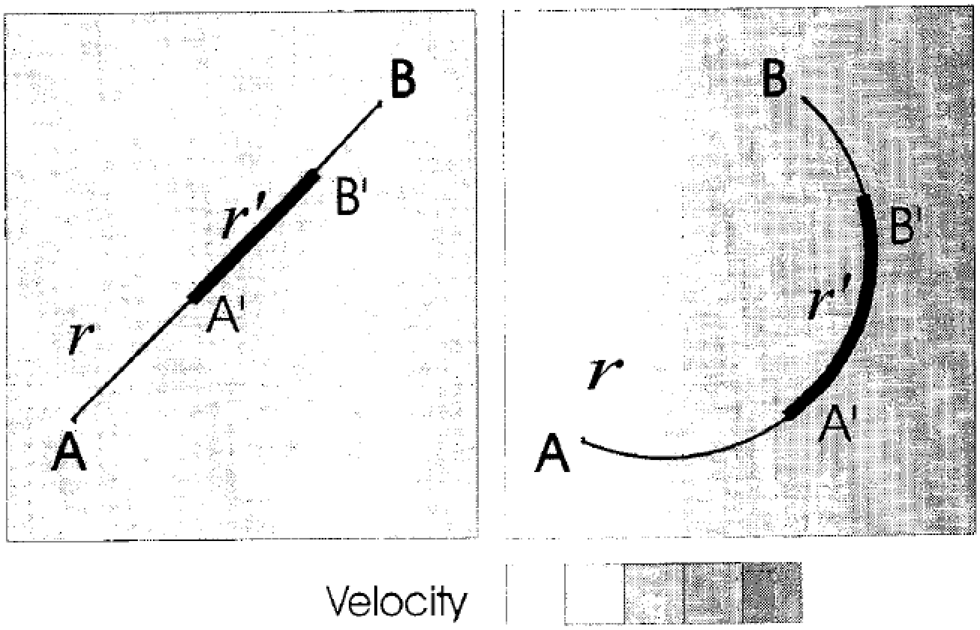

Figure 5-2: The concept behind Fermat's principle of minimum time is that any ray path between two point may be decomposed through additional points along r, which creates a ray r' from A' and B'. Color shading in the background corresponds to velocities variation. (Vesnaver, 1996)

The minimum-time approach is a known for its robust stability and simpler requirements for the velocity field in comparison with the shooting method which is a mathematical solution of DF equations. In addition, irregular grid allows for more flexible representation of the available data especially form seismic in comparison with a regular discretization. (Vesnaver, 1996) Figure 5-3 shows the modeled ray paths, velocity model (colored wireframe), and monitoring geometry (surface, and downhole) of a synthetic model mimicking our subject experiment.

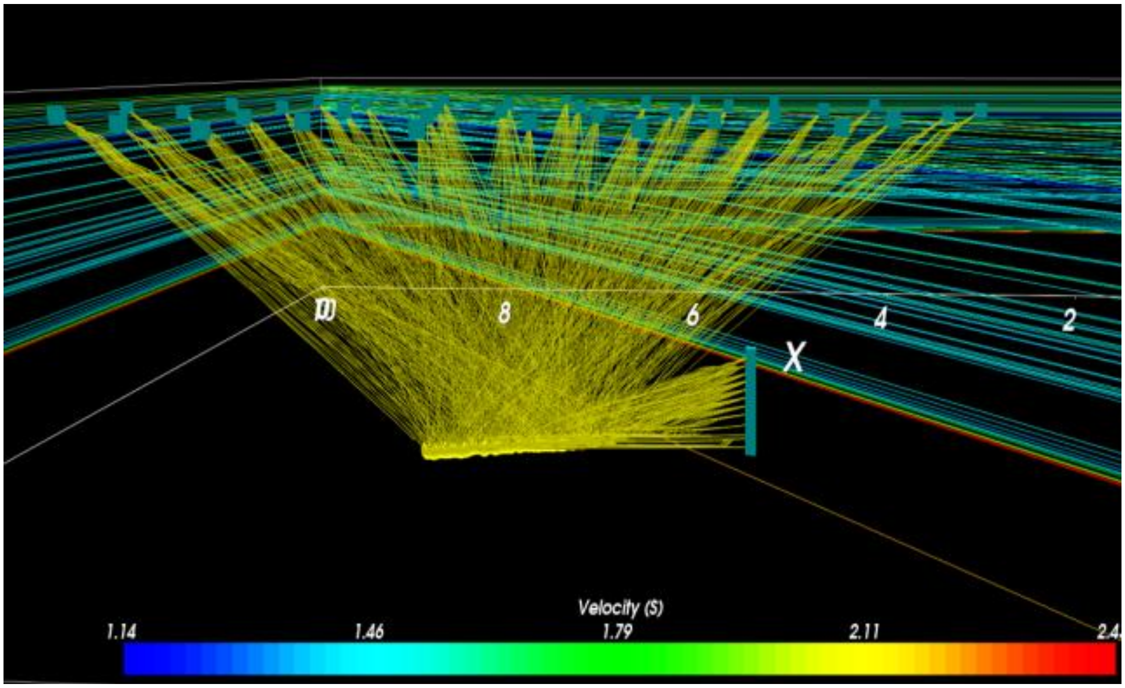

Figure 5-3: 3D Ray tracing based on irregular grid shrinking method based on surface and downhole monitoring configuration. P-wave velocity model reflected as wireframe on the background, Receivers are indicated by blue dots and sources by yellow dots.

5.2 Discrete Wave Number Method

Discrete-wavenumber method is also used as a forward modeling technique. In discrete-wavenumber method, the sum over discrete horizontal wavenumbers, k_x replaces the integral over ray parameter P. (Bouchon and Aki 1977) One of the strengths of this technique is that it includes the zero wavenumber, which can provide a solution for the static displacement near an earthquake source. Spherical wave representation would not be fully representative in shallow surfaces, where layers are almost flat and physical properties are mainly varying with depth. One approach is use a Cartesian based system with a vertical Z-axis. In such a method, the wavefield is described as a double integral over the two components of the horizontal wavenumber, kx and ky through the Weyl integral. (Aki, 1980)

[illegible]

Equation 5-1

$$\nu = \sqrt{\frac{w^2}{\alpha^2} - k_x^2 - k_y^2}, \quad Im(\nu) < 0$$

The source location is assumed as the origin of the coordinate system; and the e^{iwt} dependence is understood. After previous results generalization from 2D to 3D domain, following expression is derived (Bouchon, 1979):

[illegible]

Equation 5-2

$$k_{nx}=\frac{2\pi}{L_x}n_x, \quad k_{ny}=\frac{2\pi}{L_y}n_y$$

The described multiple-source problem is a periodic array of sources distributed at equal intervals Lx in the x direction, and Ly in the y direction. In this study, buried source and receiver model geometry were used for simulation of microseismic application, and synthetic seismograms have been calculated according to the model (Figure 5-4).

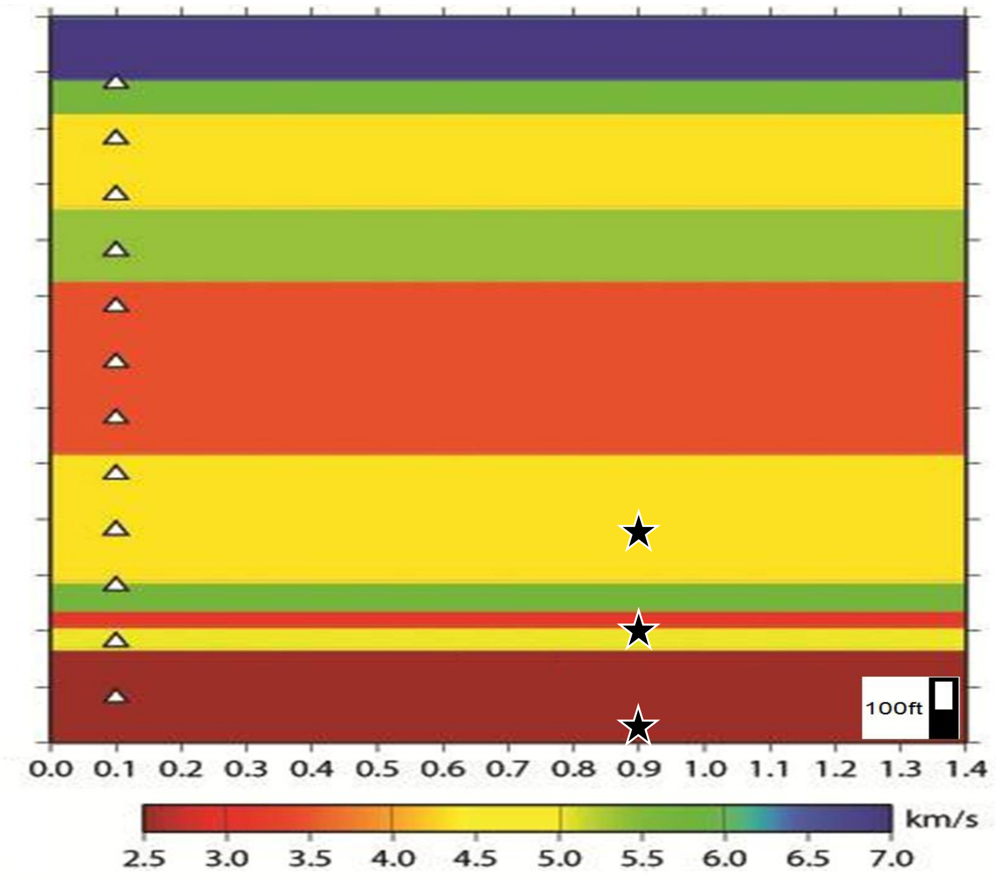

Figure 5-4: Velocity model, similar velocity structure to our subject experiment, which was used to calculate synthetic seismogram based on discrete wave number modeling technique. Black stars represent the proposed microseism source events; white triangles represent the monitoring geophones.

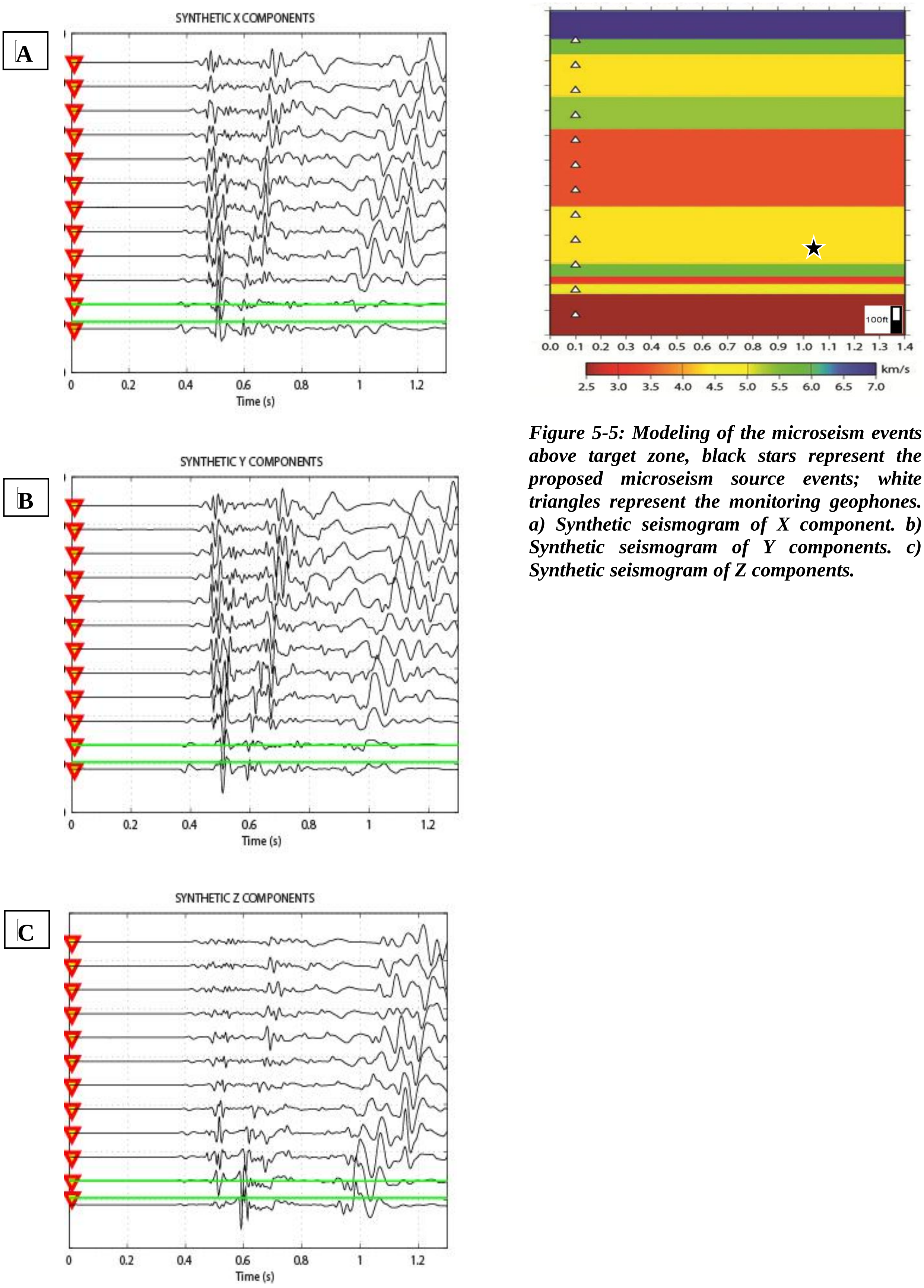

Figure 5-5: Modeling of the microseism events above target zone, black stars represent the proposed microseism source events; white triangles represent the monitoring geophones. a) Synthetic seismogram of X component. b) Synthetic seismogram of Y components. c) Synthetic seismogram of Z components.

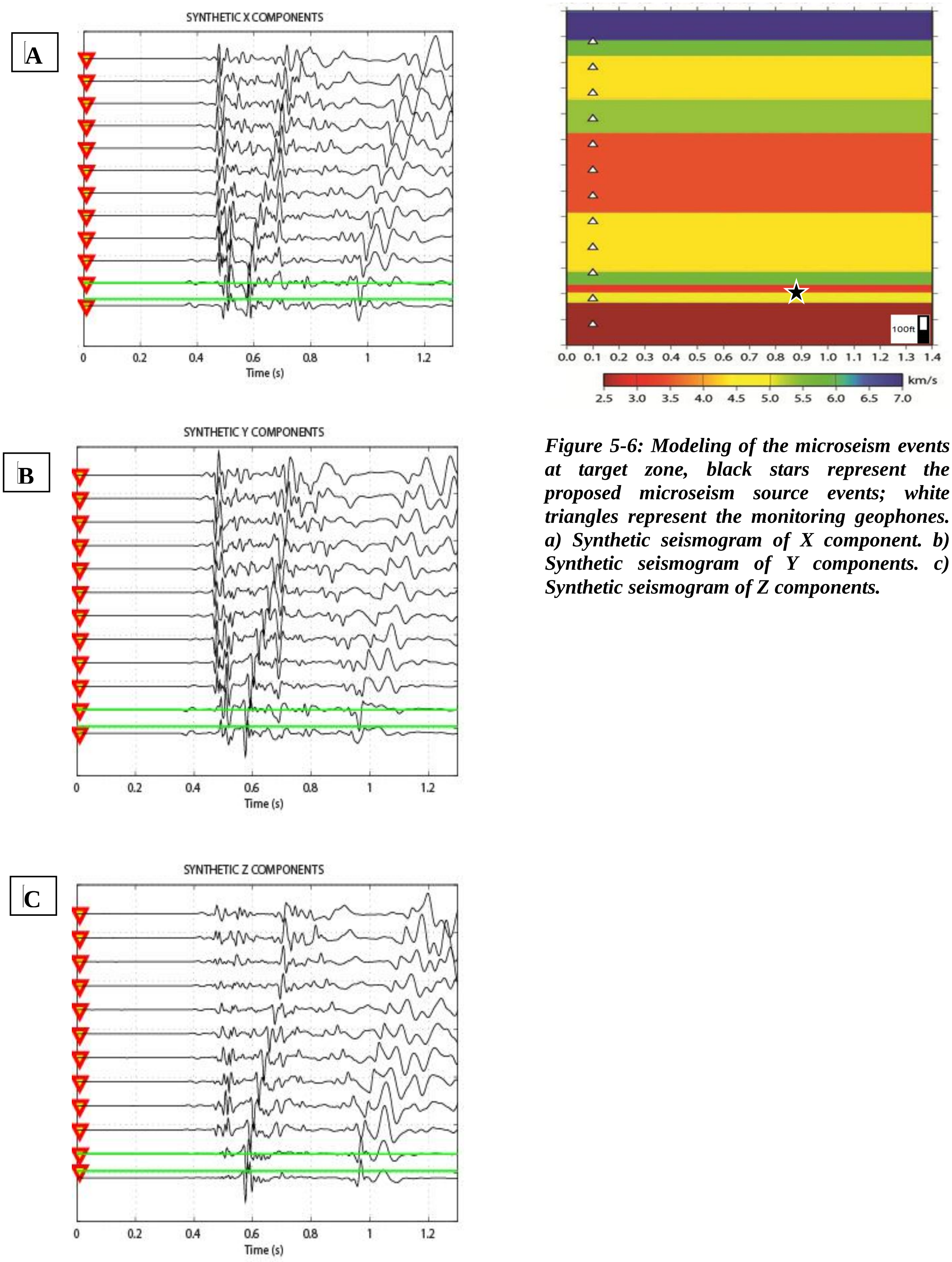

Figure 5-6: Modeling of the microseism events at target zone, black stars represent the proposed microseism source events; white triangles represent the monitoring geophones. a) Synthetic seismogram of X component. b) Synthetic seismogram of Y components. c) Synthetic seismogram of Z components.

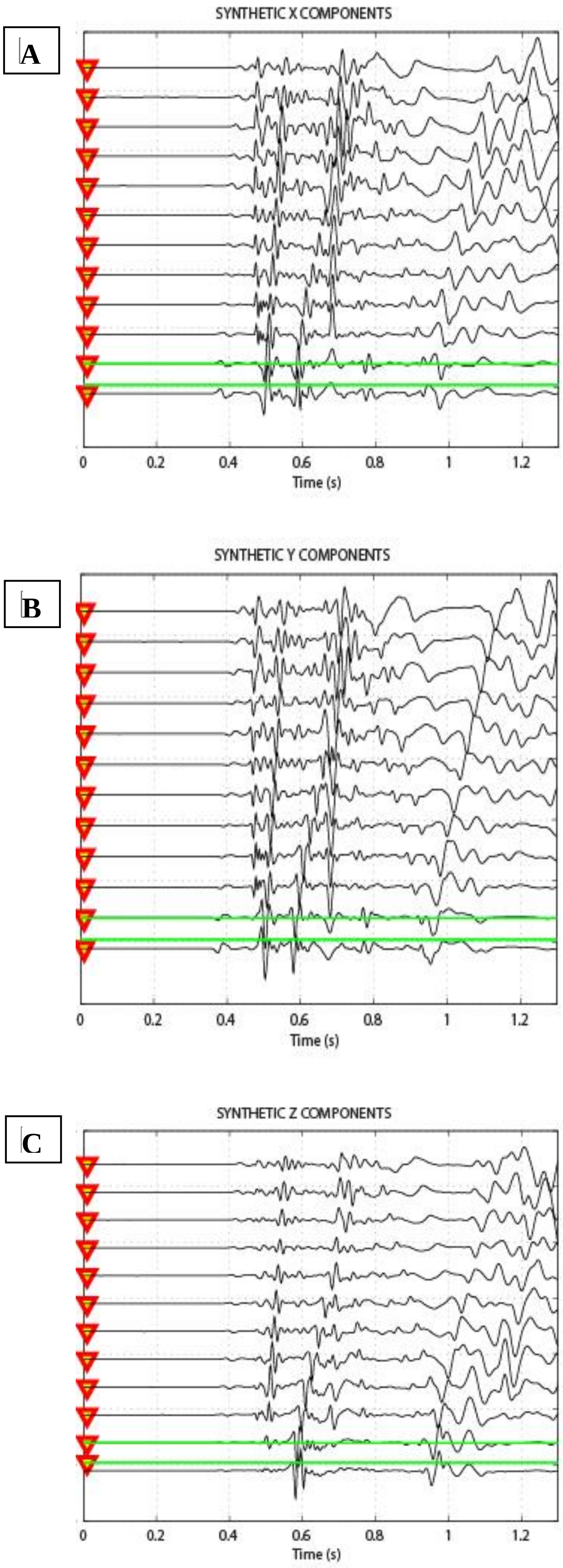

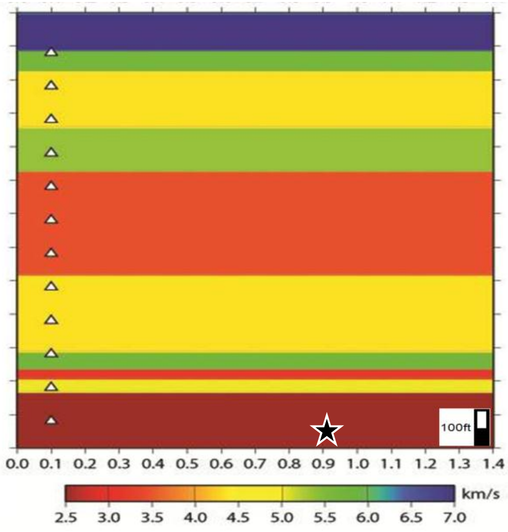

Figure 5-7: Modeling of the microseism events below target zone, black stars represent the proposed microseism source events; white triangles represent the monitoring geophones. a) Synthetic seismogram of X component. b) Synthetic seismogram of Y components. c) Synthetic seismogram of Z components.

5.3 Hypocenter Inversion Algorithm (Hypo3D)

Hypo3D locations inversion algorithm was used to relocate all modeled time arrivals by ray tracing techniques. The Hypo3D is a unique code which can jointly invert recorded waveform arrivals from surface and downhole sensors, using direct, reflected, refracted and converted waves. The hypocenters relocation code for Hypo3D has been defined in details by Vesnaver et al. (2008, 2009, 2010). The location estimation is determined by the shrinking grids technique, which comprises the steps listed below as described by Vesnaver (2009):

i. A first guess for the hypocentral coordinates (x0, y0, z0) is made.
ii. Centered at the current hypocenter guess, a 3D regular grid is defined with points at (x0 ±i Dx, y0 ±i Dy, z0 ±i Dz), where the space intervals Dx, Dy and Dz are chosen arbitrarily (and are not necessarily equal), as are the number of points for each dimension of the grid cells.
iii. The difference between the measured and modeled travel-times is computed at each grid point, and summed into the object function we want to minimize (the norm of this difference can be absolute value or squared, but the results obtained are very similar in most cases).
iv. The grid point where this function is a minimum becomes our new guess for the hypocenter.
v. If the object function is lower than a user-defined threshold, if its decrease-rate approximates to zero, or if we reach a maximum iteration number, we stop the procedure and the current hypocenter guess becomes the final estimate.
vi. Otherwise, we reduce the grid intervals Dx, Dy and Dz by a user-defined shrinking factor, and then return to step (ii).

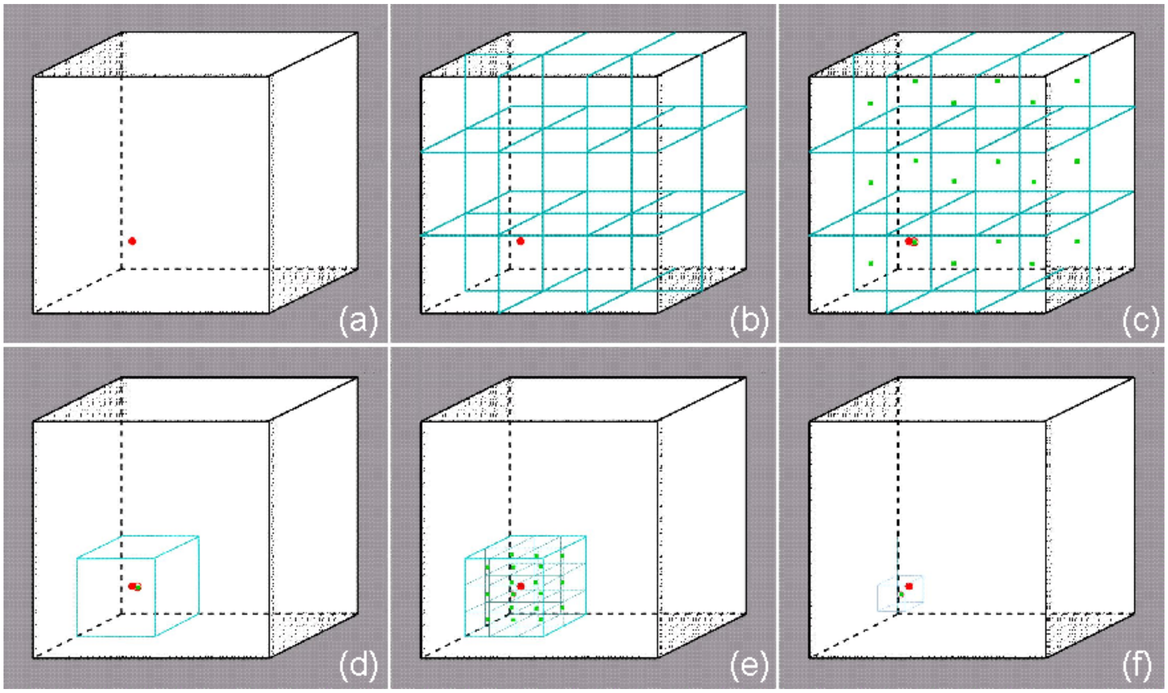

Figure 5-8: An illustration of the shrinking grids technique. The red dot indicates the unknown solution. (Vesnaver, 2010)

5.4 Forward Modeling Analysis

Perforation shots information in monitoring operations improves the accuracy of the hypocenter location, by providing either an empirical depth-travel time relation, or just an average velocity model between sources and receivers. However, as the frac grow away from the target zone, this calibration becomes less reliable. This is mainly due to potential reservoir heterogeneity such as an increase or decrease in the density of natural fractures, change in elastic properties, change in lithology, etc. In addition, the frac itself changes the original rock dynamic and elastic properties which add to the complexity. Therefore, a full 3D Earth model, ideally evolving in time (i.e., 4D), to get accurate hypocenters' locations is needed. An active 3D seismic survey may provide a fairly accurate 3D model in depth, via pre-stack depth migration or reflection tomography.

Table 5-1 summarizes the P-wave and S-wave velocity information at the monitoring well location, along with the relative depth of formation tops. Therefore, homogenous layers are assumed in all of the study's models. Figure 5-9 shows the three models we built with increasing complexity, i.e. a coarse 1D macro-model composed of 7 layers (model A), a finer 1D model with 62 layers (model B) and a 3D model with irregular interfaces but 7 homogeneous layers (Model C), denoted by A, B and C, respectively.

Table 5-1: Depth of formation tops, P and S velocities, and Vp/Vs ratio in Model A and C. Model B is composed of 62 layers and is not reported here for brevity. Depth been referenced from 0-1000 depth unit.

Layer	Formation Top	Vp (m/s)	Vs (m/s)	Vp/Vs
1	0	2830	1415	2.00
2	141	2777	1388	2.00
3	802	3614	1612	2.24
4	857	4087	2351	1.74
5	1000	4801	2660	1.80
6	<1000	4740	2581	1.84

Figure 5-9: Earth models used to test the relocation accuracy: coarse 1D (A, left), fine 1D (B, centre) and coarse 3D (C, right).

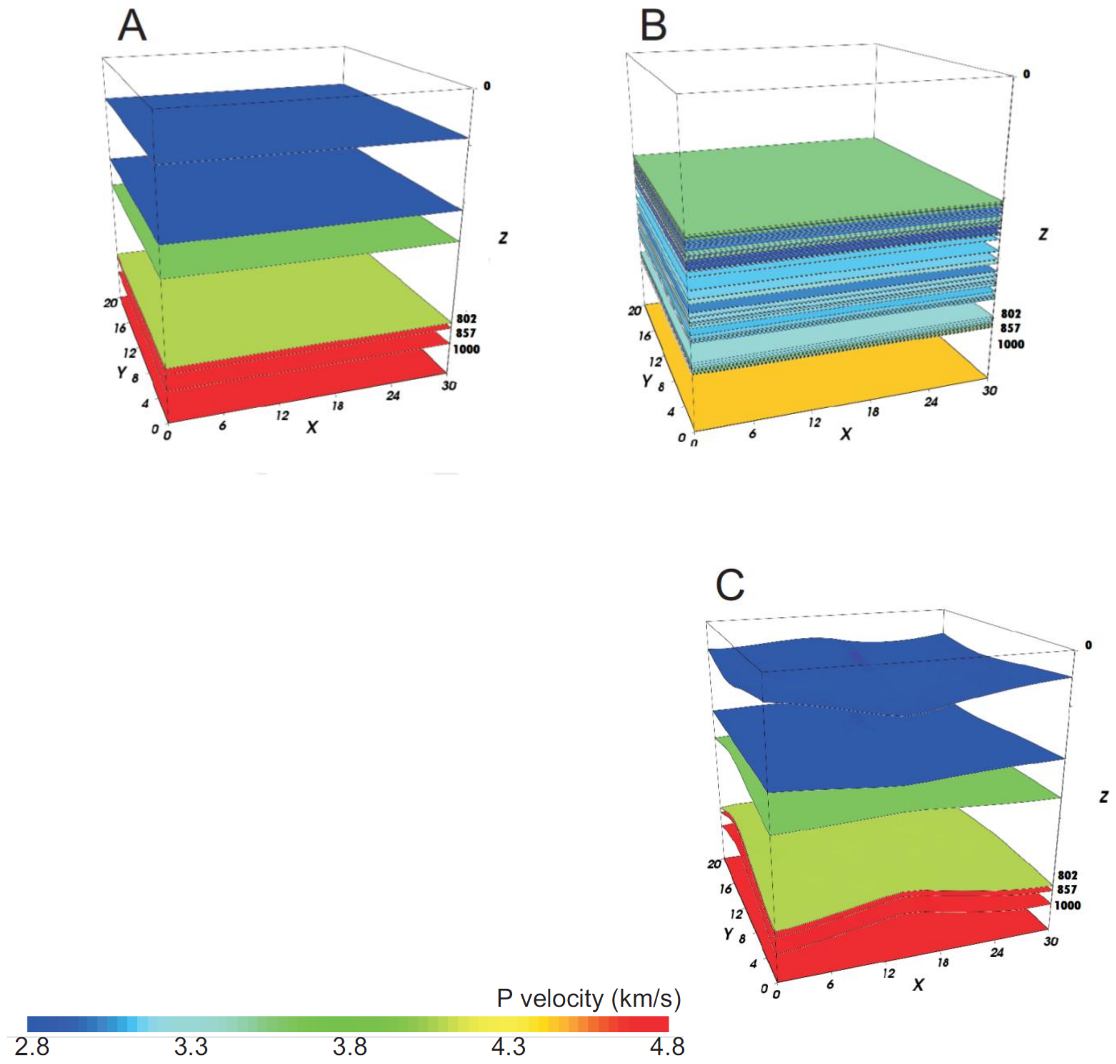

The topography is not flat, as elevation differences exist up to 200 m, and even less flat is the target formation, where such a range exceeds 400 m. The topography changes are taken into account in all our tests for the receivers' coordinates, while the structure variations at the target are allowed for in Model C only. A key feature to be noted is the strong changes in the Vp/Vs ratio at the boundaries of the target formation, i.e., at the interfaces 3 and 4. This feature is the main cause for errors in the time origin estimates (see also Vesnaver et al. (2010)).

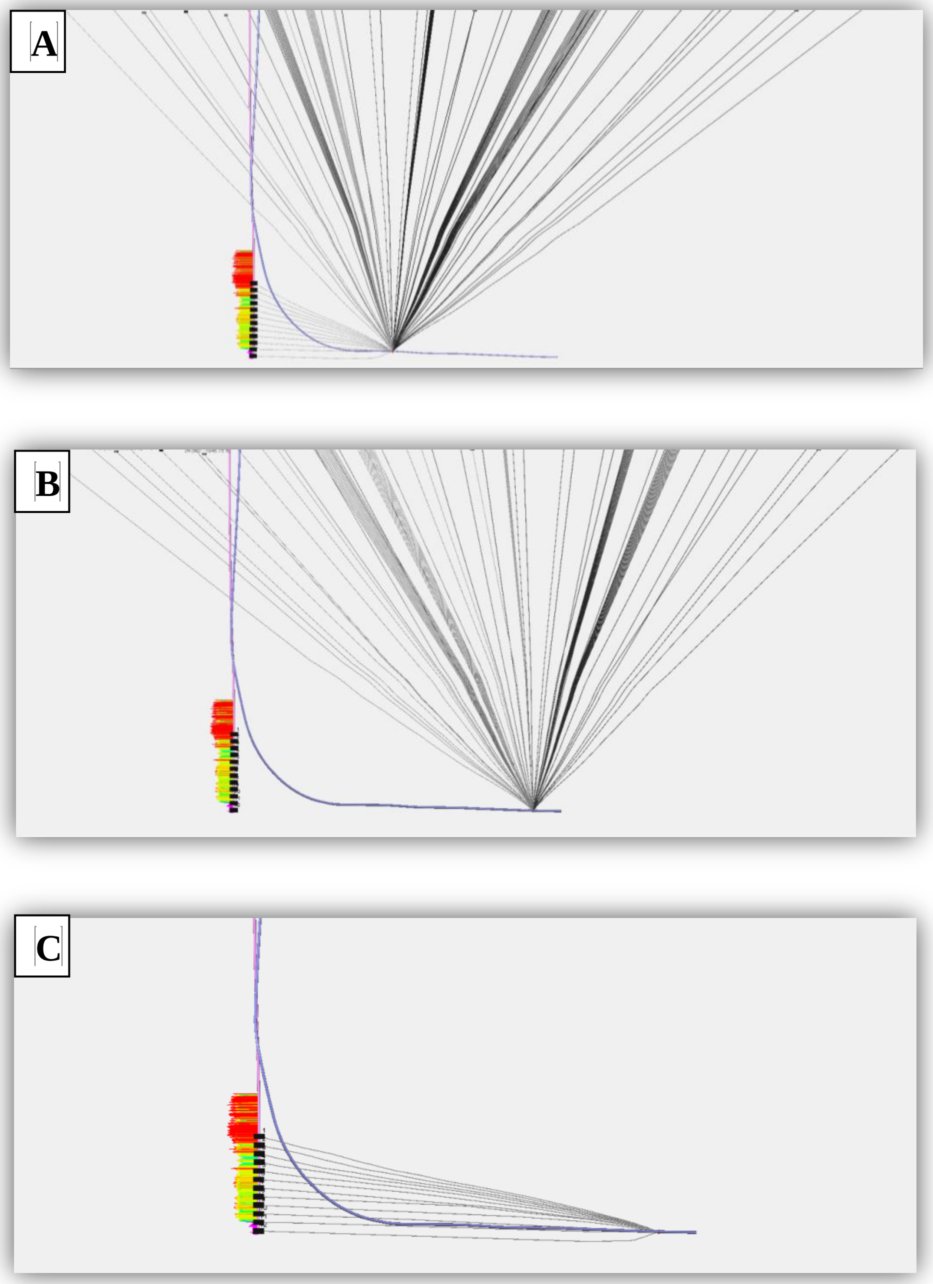

Figure 5-10: Three different monitoring configurations according to our subject experiment geometry. Black lines represent modeled ray path of the different configurations.

The inversion algorithm used adopts the “shrinking grids” (Vesnaver *et al*. 2008, 2010), whose accuracy is comparable to the method of Lomax *et al*. (2000). For all following tests, the dimension of the shrinking grids are 5x5x9 in the *x,y,z* directions, respectively, with an initial search range of 500x500x300 m and 25 iterations. The time origin is estimated initially by the Wadati method, followed by a few small perturbations. When both surface and borehole data are inverted, I used only the surface data for estimating the time origin, as this reduction improves significantly the relocation accuracy.

In the subject experiment that I am mimicking, I know the exact location of the source and the time origin, i.e., the shooting time, for the perforation shots. To assess the precision of the method, I ran first a few tests to locate the perforation points, assuming that both their shooting time and approximate location are known. Table 2 provides some numerical details in the first 3 rows: we see that the coarse models A and C get average errors in the hypocentral coordinates smaller than 20 m in both the Δz vertical and Δr radial directions when the surface receivers are involved, while errors are large when using only borehole receivers or for the very fine Model B, for this and for all following cases.

After the hydraulic pumping starts, micro-earthquakes are generated: initially in the vicinity of the injection point and later, in most cases, within an expanding front that may be described by a diffusion equation (Shapiro and Dinske, 2009). We may assume as an initial guess for our hypocentres the location of the injection point, although we may not assume the time origin as known any more. This case is spanned by the second group of 3 rows in Table 5-2. The errors in *x* and *y* remain marginal, but a certain interdependence shows up between depth and time origin errors.

Model	Borehole only			Surface only			Surface + Borehole			Known time origin	Guessed hypocentre
	Δz	Δr	Δt_0	Δz	Δr	Δt_0	Δz	Δr	Δt_0		
A – 1D coarse	138	462	0	-43	24	0	-43	27	0	Yes	Yes
B – 1D fine	111	672	0	-3	220	0	506	112	0	Yes	Yes
C – 3D coarse	49	415	0	-3	23	0	-3	23	0	Yes	Yes
A – 1D coarse	158	25	-13	196	16	4	158	25	-13	No	Yes
B – 1D fine	510	174	-25	-3	220	-3	-92	1005	-864	No	Yes
C – 3D coarse	150	27	-18	150	27	-18	138	12	-31	No	Yes
A – 1D coarse	88	2083	16	14	194	2	23	158	-15	No	No
B – 1D fine	-92	1097	-863	220	266	-970	-92	1097	-863	No	No
C – 3D coarse	-131	2019	12	159	27	-16	139	13	-30	No	No

Table 5-2: Average errors in relocation (m) and time origin (ms) for different models, recording geometries and information about time origin and guessed hypocentre using the injection locations.

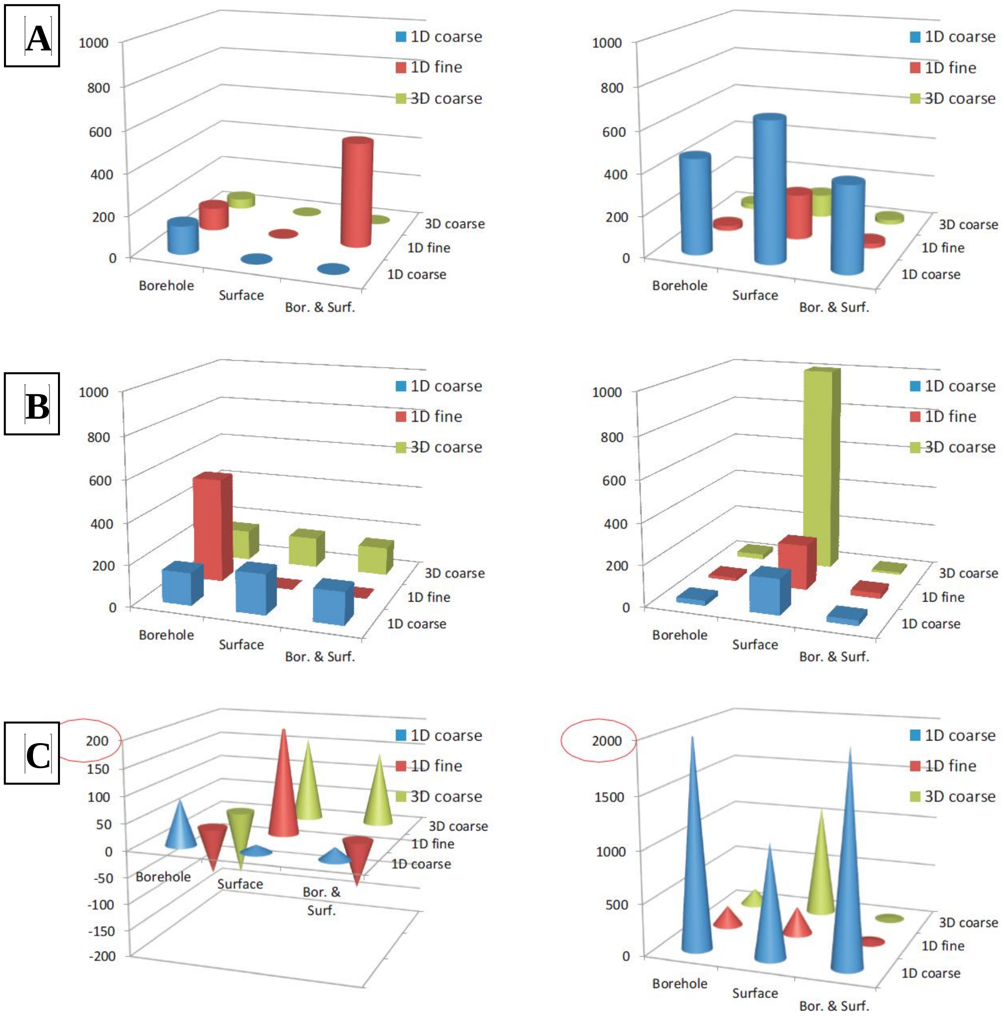

Figure 5-11: a) location errors when assuming the perforation shot location as the initial guess for the hypocenter and a known time of origin. b) Location errors when assuming the perforation shot location as initial guess for the hypocenter and an unknown origin time. c) Location errors without any assumption.

After a significant time from the injection start, the hypocentres may be located at significant distances from the injection point: if there exist preferential flow pathways along reactivated faults, such a distance may exceed several hundred meters. In that case, it makes sense not assuming any initial guess or constraint about the hypocentre, relying only on the available traveltimes. This is the case covered by the last 3 rows in Table 2, where we notice again the same features as for the previous case: errors are large when using borehole receivers only, but are acceptable in the x and y dimensions when the surface receivers are included in the relocation. The borehole receiver contribution, when jointly inverted, is reducing the ambiguity between depth and time origin estimations.

A mismatch exists in real experiments between the actual Earth and the model we adapt to approximate it and estimate the hypocentres. This problem is not addressed here, but we refer the reader to Vesnaver and Urpi (2013); who showed that a simplified macro-model for the Earth provides fairly accurate epicentral locations, when the (micro)-earthquakes are located in an area well covered by the receivers, even when the errors in the velocity model exceed 10%, while the hypocentre depth is affected by major errors. This finding is consistent with the results obtained, although in a different geological framework.

CHAPTER 6:
MICROSEISMIC DATA QC AND PROCESSING

The objective of microseismic optimal processing objective is to calculate source characteristics from the recoded microseismic signal. Basic processing determines the source location of the microseism events along with quality attributes, both represent the foundation for interpreting the hydraulic fracture geometry. The spatial-temporal distribution of the hypocenters is elementary for advance processing workflow that goes beyond “dots-in-the-box” toward more source attributes and information. A typical microseismic processing workflow would include,

1. Overall data QC analysis.
2. Monitoring geometry, and sensor orientation setup.
3. Signal characterization, and enhancement.
4. MS events detection (STA/LTA)
5. Velocity model calibration.
6. Hypocenter Location estimation.
7. Event Analysis and Interpretation.

The scope of this project includes processing of the highest signal to noise (SNR) recorded events for microseismic uncertainty analysis. The following sections will discuss the workflow that I have used throughout this study for microseismic processing.

6.1 Data QC Analysis

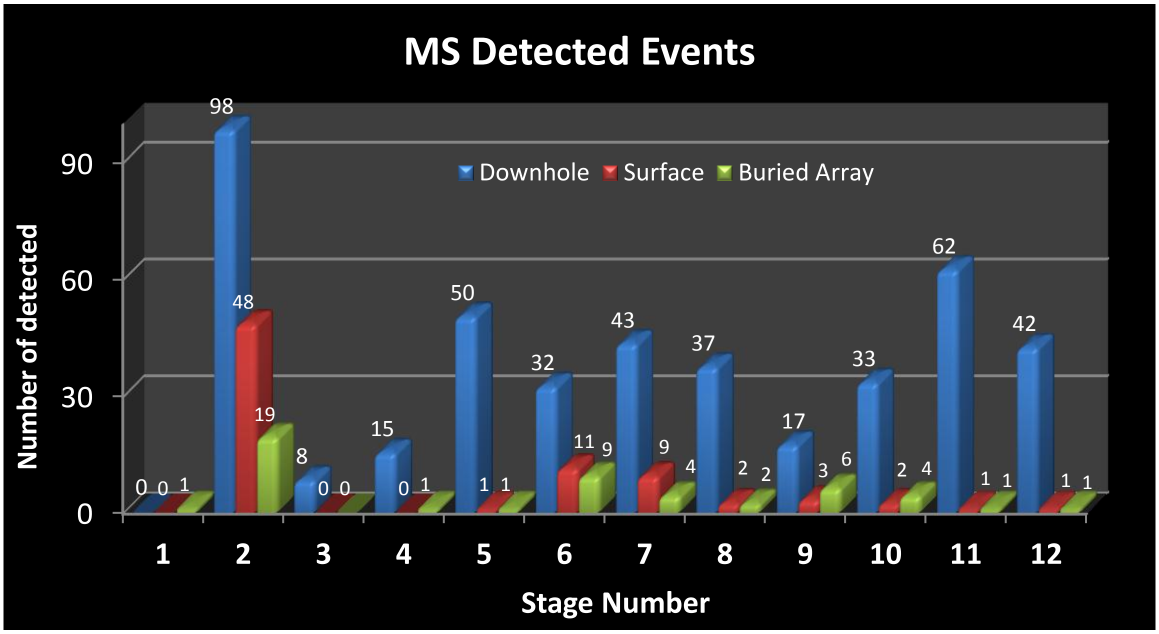

Figure 6-1: a diagram show the total of MS detected events on each monitoring system.

The overall data review shows a challenging data quality especially on surface, and for buried array recorded data. Figure 6-1 shows the number of events that was detected on each monitoring system for every stage. As expected, the number of events detected on the downhole array far exceed the number of events recorded on the surface and buried array. Downhole data have the highest SNR compared to shallow wells and to the surface array, see figure 6-2. It remains unclear the reason behind the low number of detected events on the shallow and buried array. However, elevated background noise during pumping is with no doubts limiting the number of weaker events that can be detected. Figure 6-3 shows the noise recorded during a monitored stage plotted together with other treatment parameters such as pressure, pumping rate and proppant concentration. A correlation of noise variations with the different pumping periods is evident in the across all monitoring components.

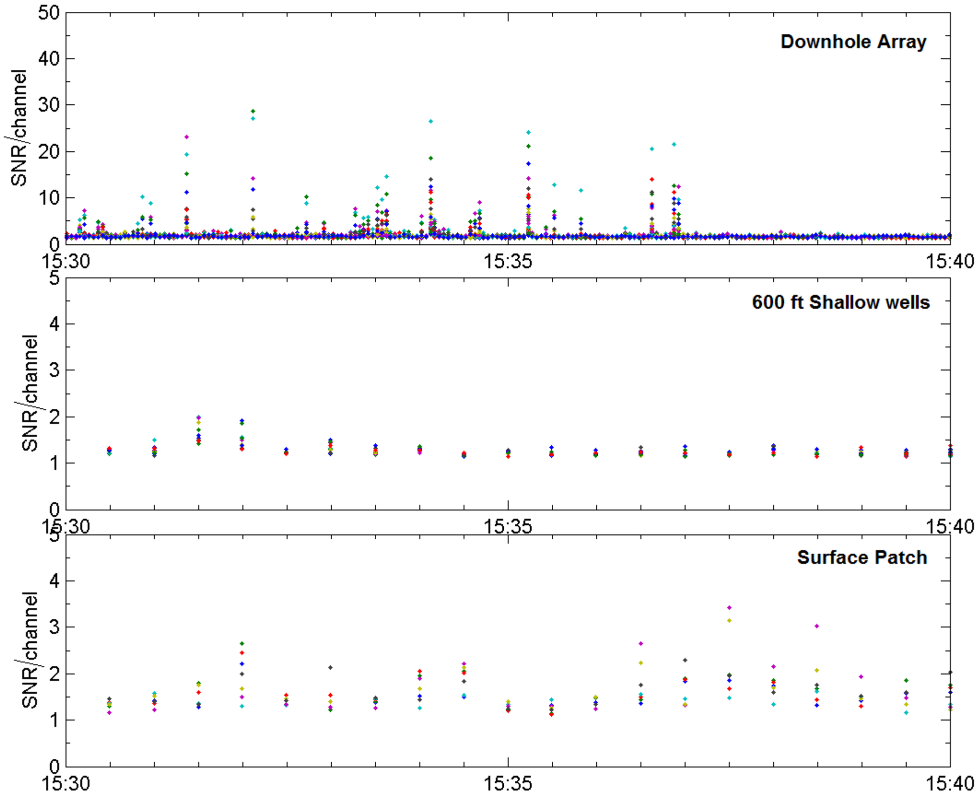

Figure 6-2: SNR plots of the recorded microseismic data of the three different monitoring systems.

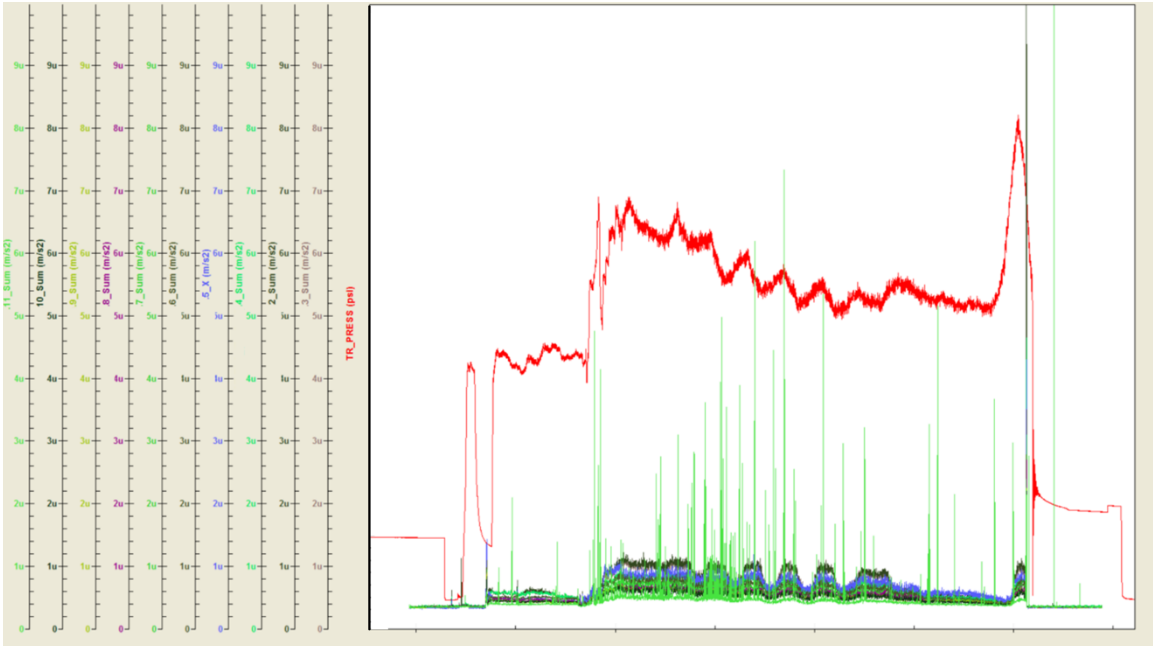

Figure 6-3: Observed noise levels by the down hole monitoring system and the corresponding treatment pressure (r

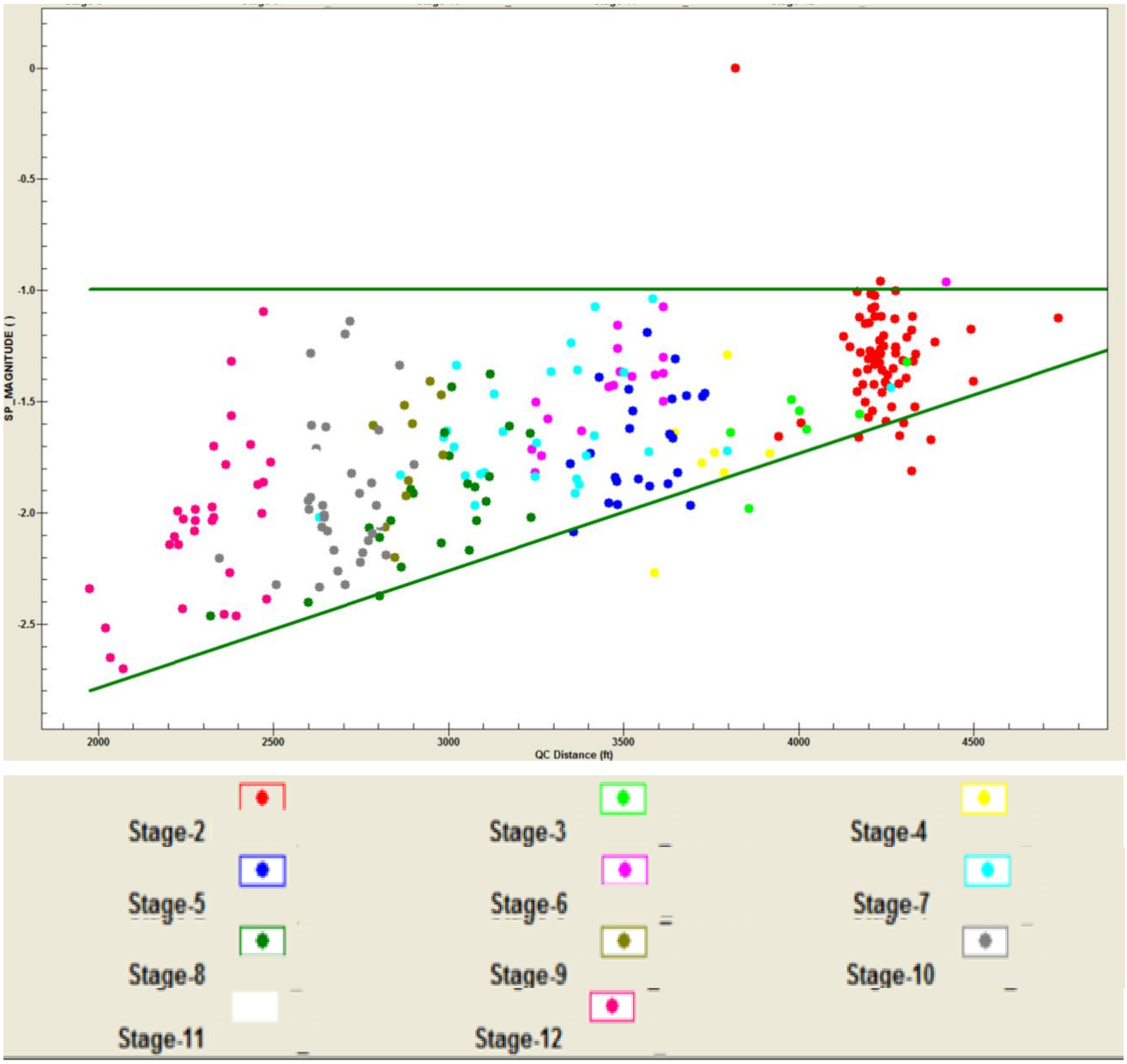

Figure 6-4: A magnitude vs. distance plot for the monitored events. Different colors refer to different monitored stages.

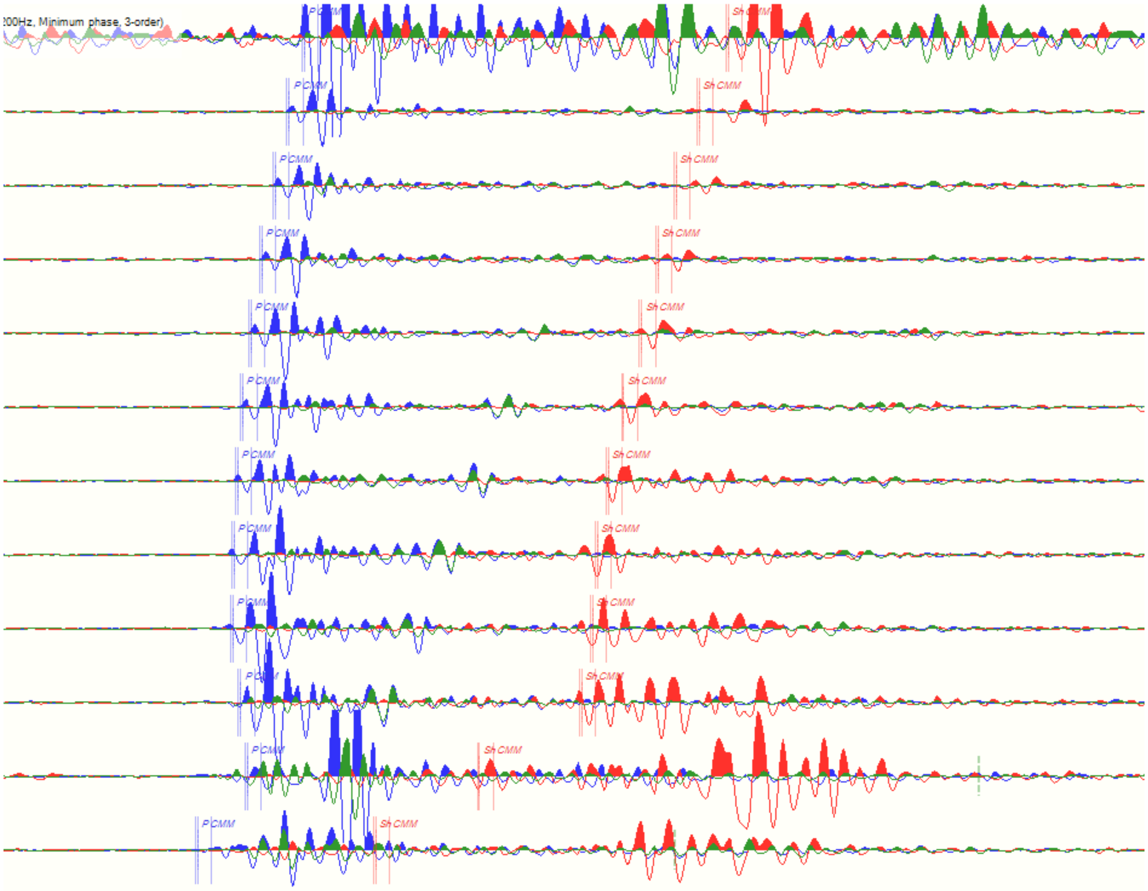

Figure 6-5: An example of a high SNR event recorded on downhole array.

The results of surface data has been challenging in general for both shallow grid and surface lines. A quick analysis of the waveforms shows a clear low SNR with a strong coherent and anomalous background noise in the data hindering potential microseismic arrivals. Monitoring company reports point at the close presence of operating equipment above the well pad as the source of the random noise, however, some attribute it to the near surface complexity. Due to the challenging nature of the recorded surface data, it has been excluded from the scope of this master thesis. It is recommended for future follow up research to incorporate surface data. See figures 6-6, 6-7 for a sample of fairly good events on few stations and seismic surface lines, the anomalous noise, the coherent noise recoded on the surface monitoring systems.

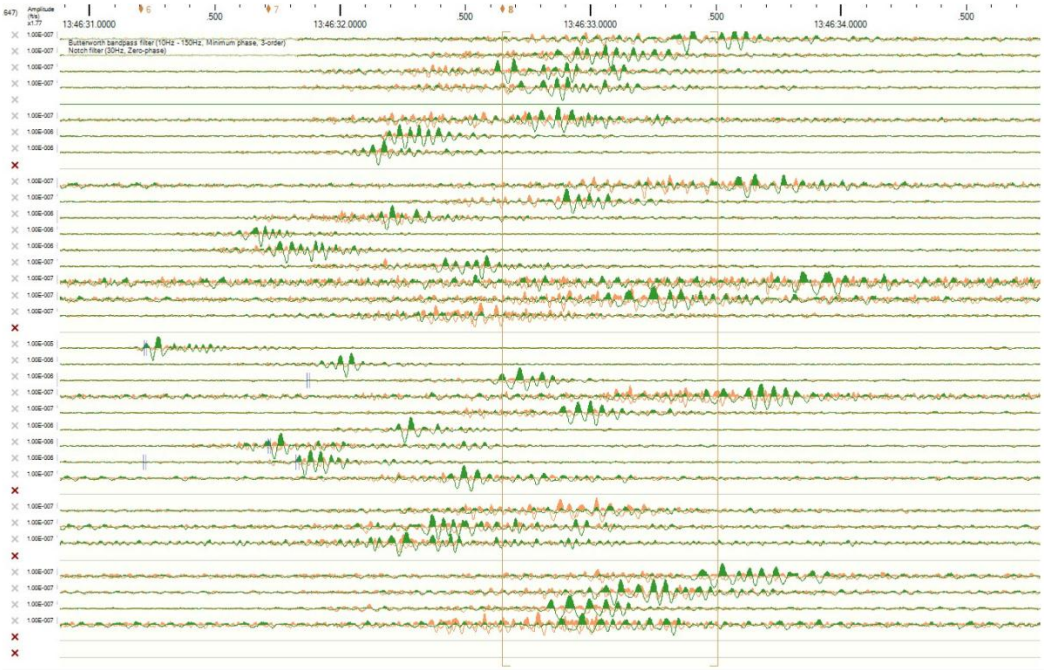

Figure 6-6: A recorded event on the buried array, however spatial distribution of wells introduces interpretation complexity.

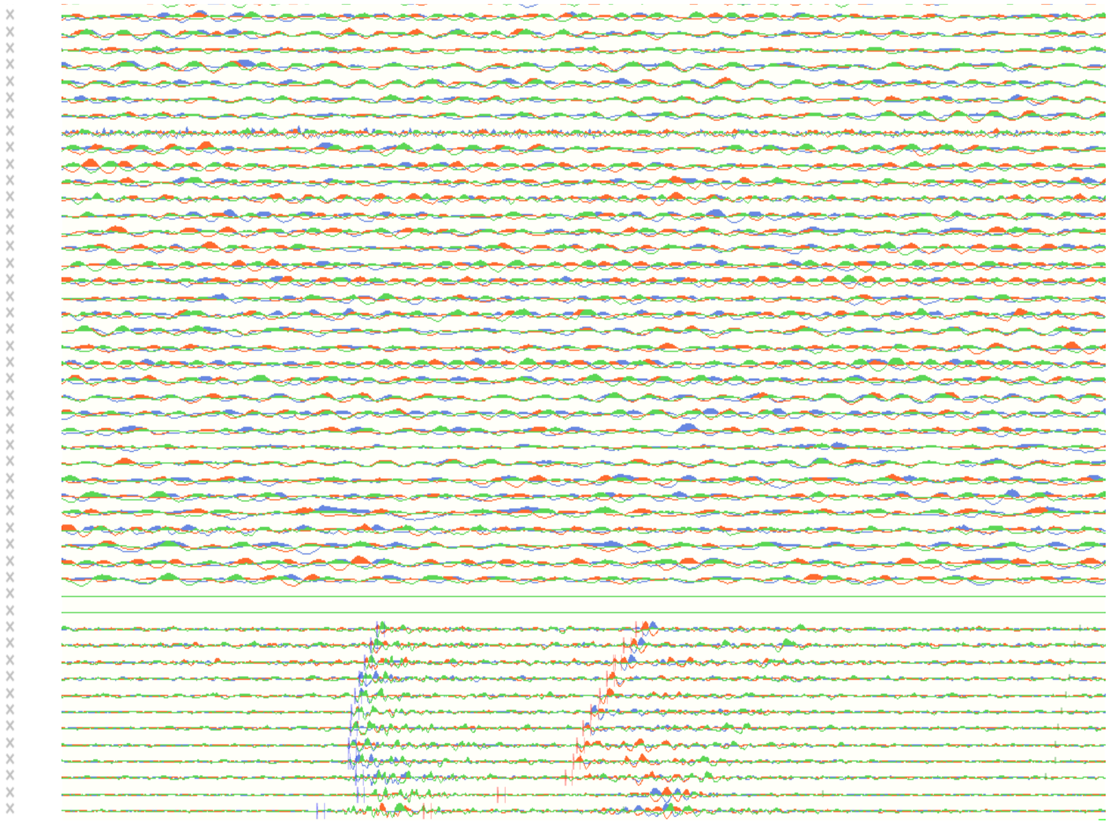

Figure 6-7: a high SNR observed event on downhole array, and the crossponding recorded buried array data.

6.2 Spectral Characteristics and Signal Conditioning

This section will shed the light on the spectral characteristics of recorded microseismic seismic signal. Figures 6-9 6-10 6-11 shows an example data set of raw (unfiltered), high signal-noise ratio (SNR) microseismic event. The main objective is to find the frequency band of the microseismic events to design and apply an optimal Butterworth bandpass filter for noise attenuation.

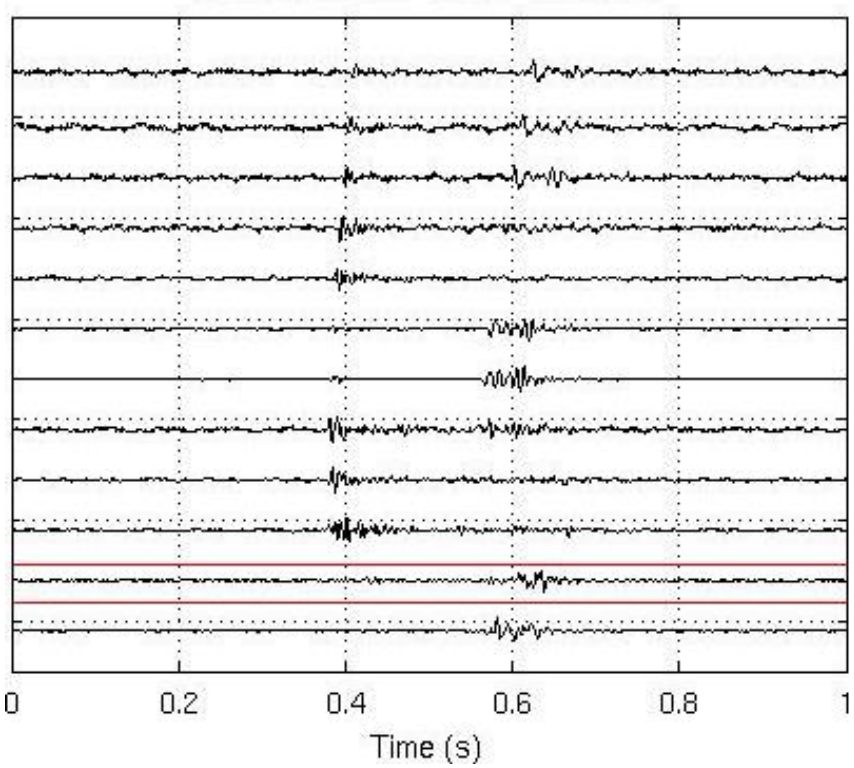

Figure 6-8: X Component of microseismic data. Geophones were orientated arbitrarily on the field and no data processing method have been applied (raw seismic data).

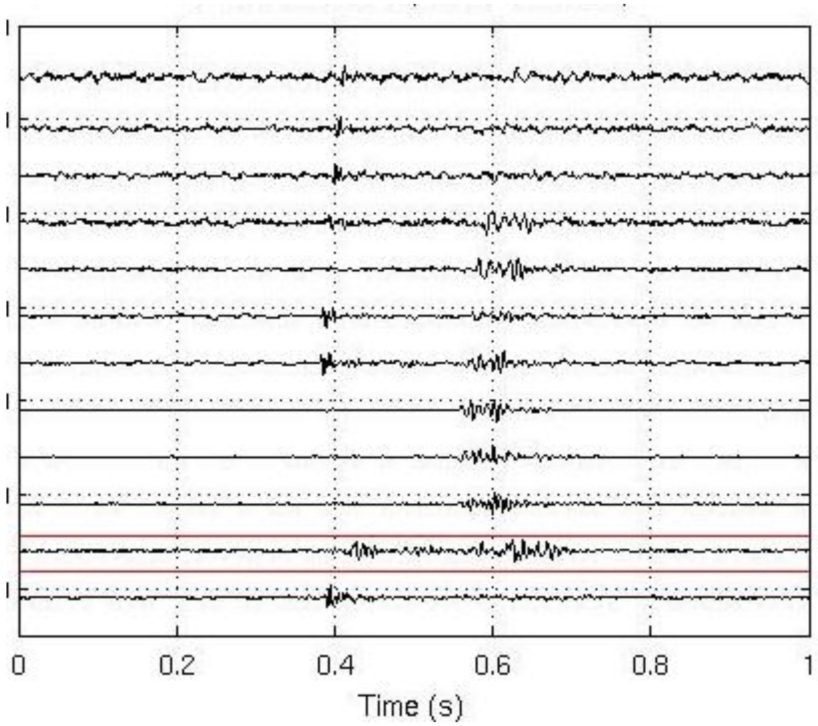

Figure 6-9: Y Component of microseismic data. Geophones were orientated arbitrarily on the field and no data processing methods have been applied (raw seismic data).

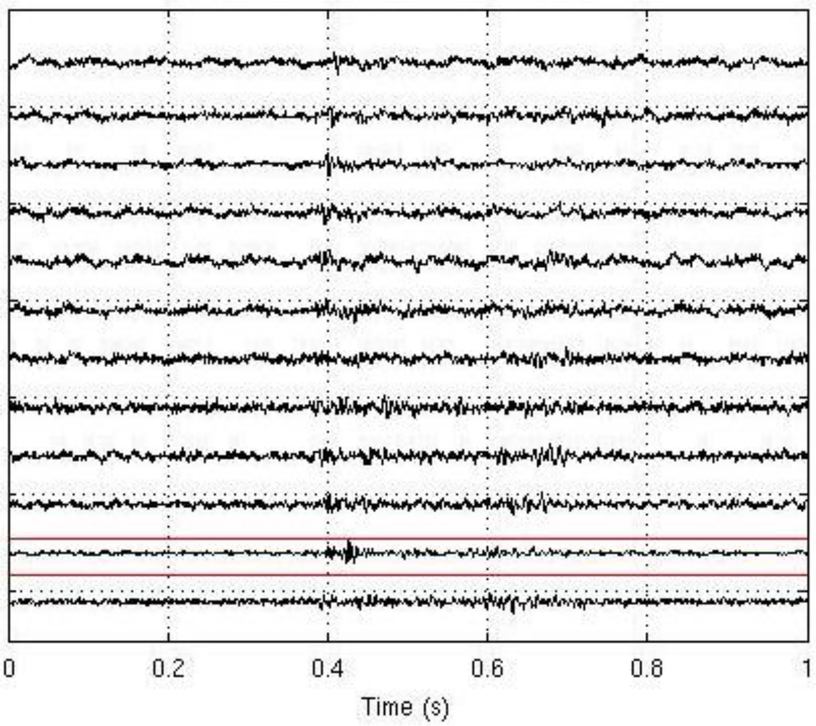

Figure 6-10: Z Component of microseismic data. Geophones were orientated arbitrarily on the field and no data processing method have been applied (raw seismic data).

To analyze the seismic data, I applied a regular Fourier spectral analyses and spectrogram analyses. Figure 6-11 shows amplitude spectrum of the selected microseismic time sequence. Two very high energy peaks in narrow frequency band are clearly dominating the spectrum up to 50 Hz. This spectrum shows clearly that the microseismic signal was contaminated by operational and other microseismic noise. Under the influence of this high spectral energy, microseismic signal has not been clearly identified on the spectra. To identify the frequency content of the microseismic signal, I applied two different methods of the Spectrogram analysis.

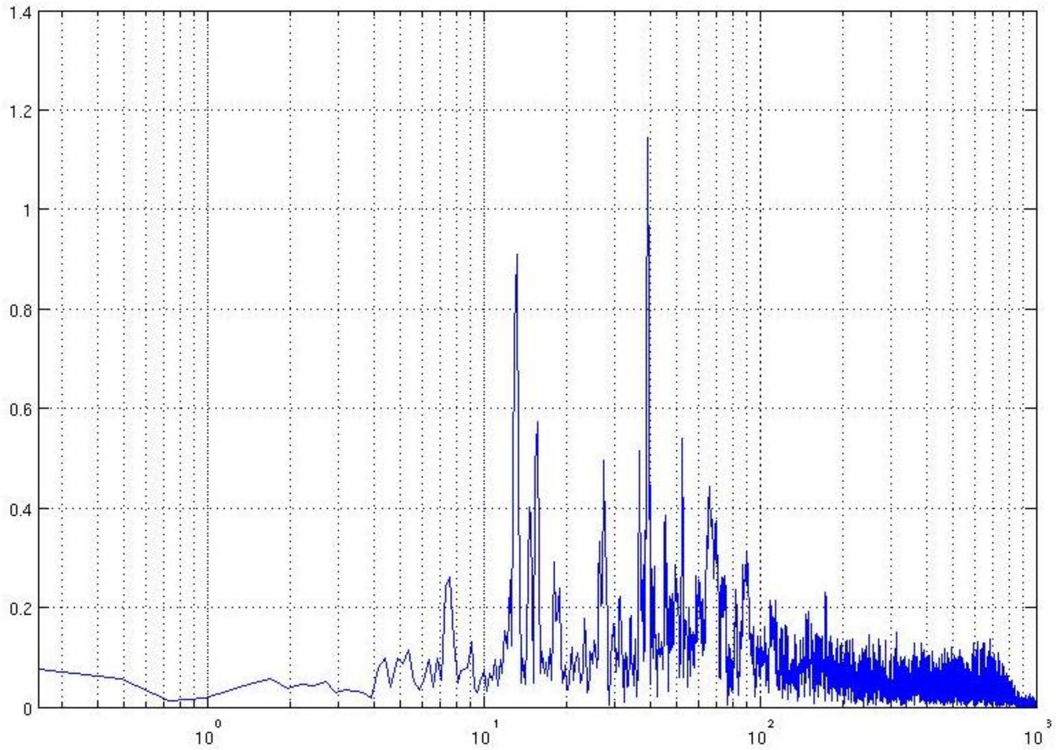

Figure 6-11: Frequency spectrum of selected seismic data of geophone. Note the highest peak of the amplitude around 35 Hz is indicating one of the operational noise effect.

Spectrogram analysis is a unique spectral method, based on the display of instantaneous frequency concept of the seismic data. A spectrogram analysis and associated characteristic function were used to pick weak seismic events on microseismic data (Song et al. 2010). This method has been implemented as transformed spectrum “S”. The main benefit of transformed spectrogram based phase detection is that besides the current energy term, it incorporates an “energy jump term” to capture high energy contrast (Figure 6-13 6-14). Main formulation of the transformed spectrum will be discussed in the next section 6.3 of this thesis.

Transformed and log-transformed spectrograms are based on the moving windows operator. Therefore, they present an average energy in the frequency - time domain. They are not affected by sharp instantaneous frequency peaks. Figures 6-13 and 6-14 clearly show the frequency contents of the P and S arrivals which are located between 50-200 Hz intervals on both figures (Figure-2b and c).

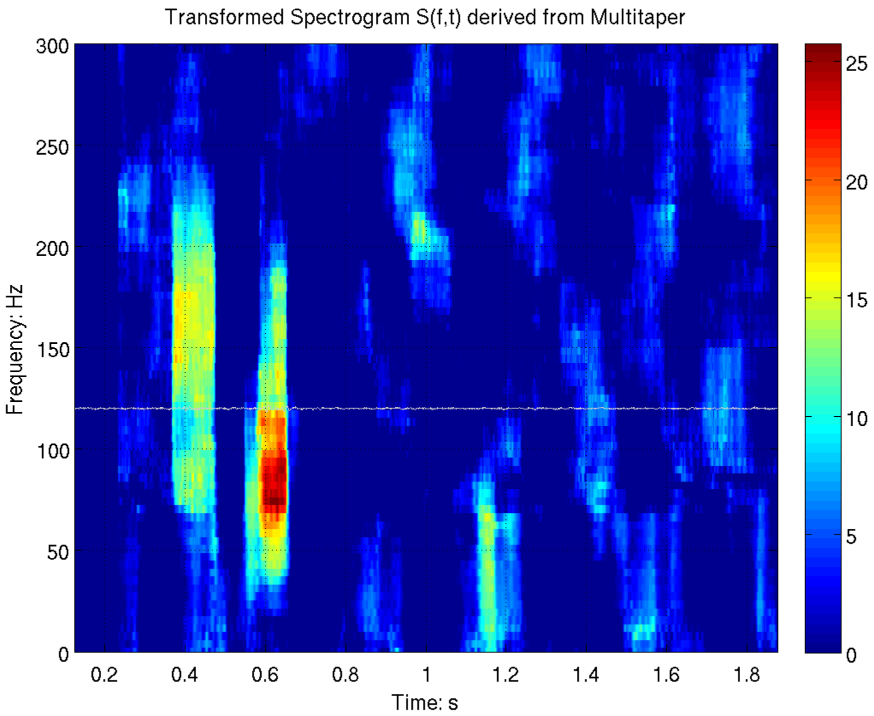

Figure 6-12: Spectogram (Song et all, 2010) of the selected seismic data. P and S wave seismic frequencies are clearly identified according to their arrival times.

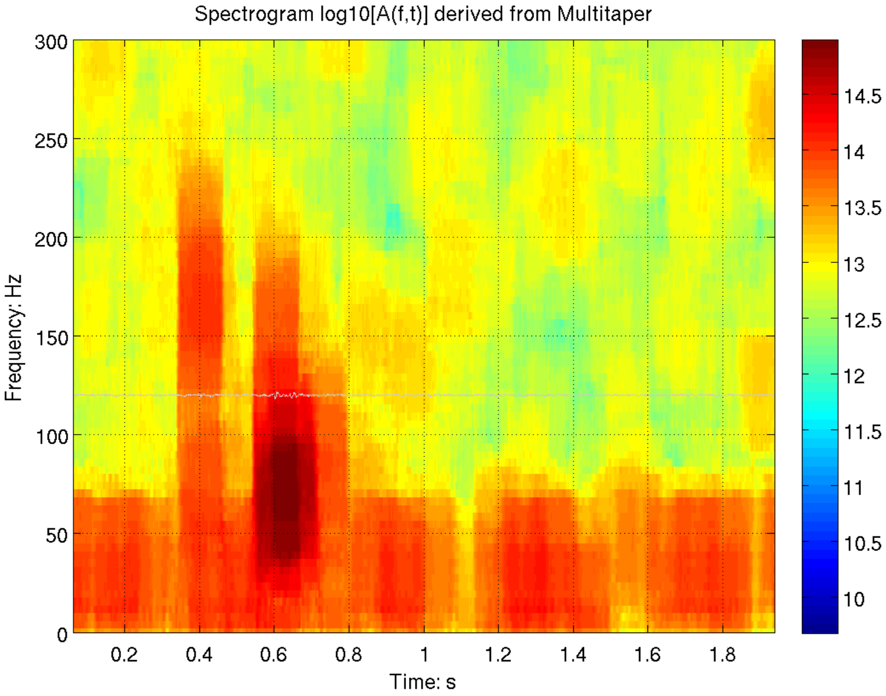

Figure 6-13: Logarithmic display of the Transformed Spectrogram of the selected seismic data provides different display for P and S wave energies.

After determining the frequency content of the P and S wave arrivals, I designed a Butterworth Band-Pass filter. All seismic data was filtered by a 35-200 Hz Band-Pass Butterworth type filter. Filtering was applied in time domain for all seismic data. Figures 6-15, 6-16, 6-17 show the filtered versions of the same data which was given in Figure 6-9, 6-10, 6-11. The P and S wave forms and arrivals are clearly identified on the X, Y and Z components. Filtered seismic traces were used for location estimation of the seismic events. If P or S arrivals were not clearly identified, a wave enhancement process was applied. The wave enhancement process is described on the next section 6.3.

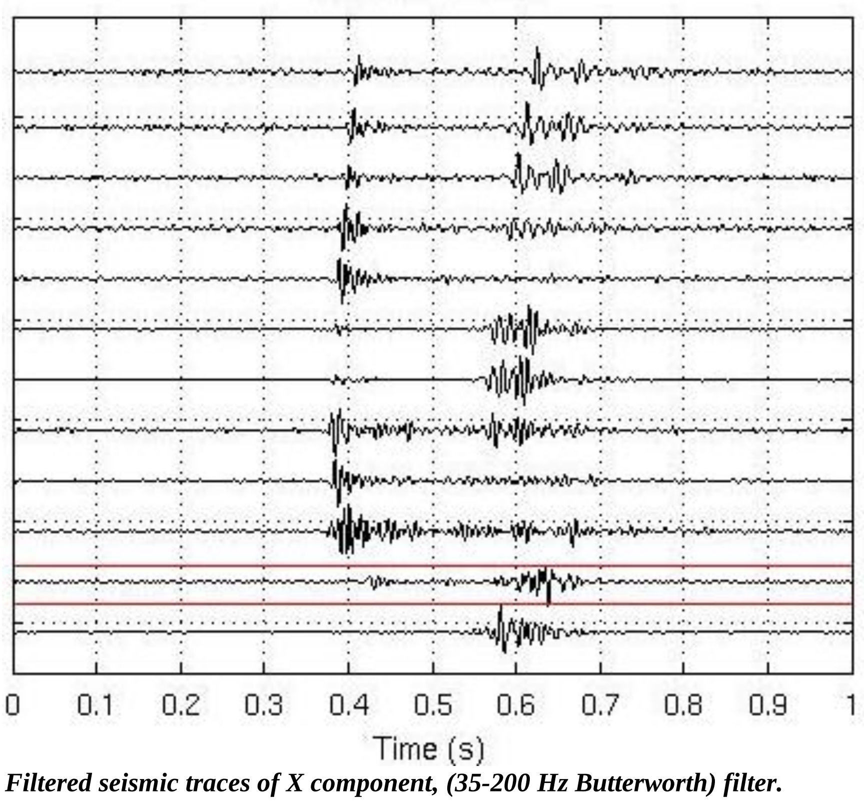

Figure 6-14: Filtered seismic traces of X component, (35-200 Hz Butterworth) filter.

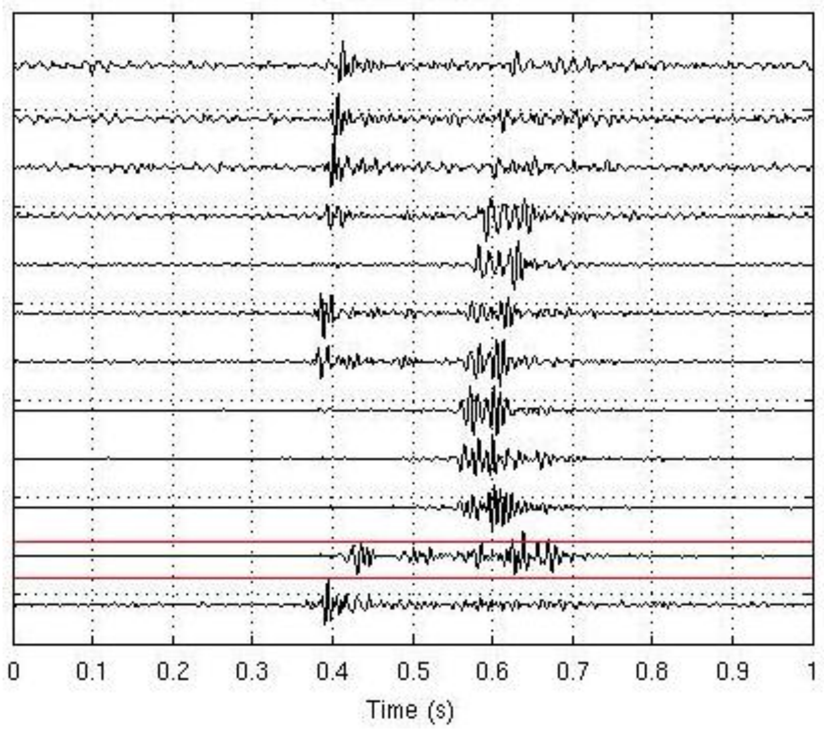

Figure 6-15: Filtered seismic traces of Y component, (35-200 Hz Butterworth) filter.

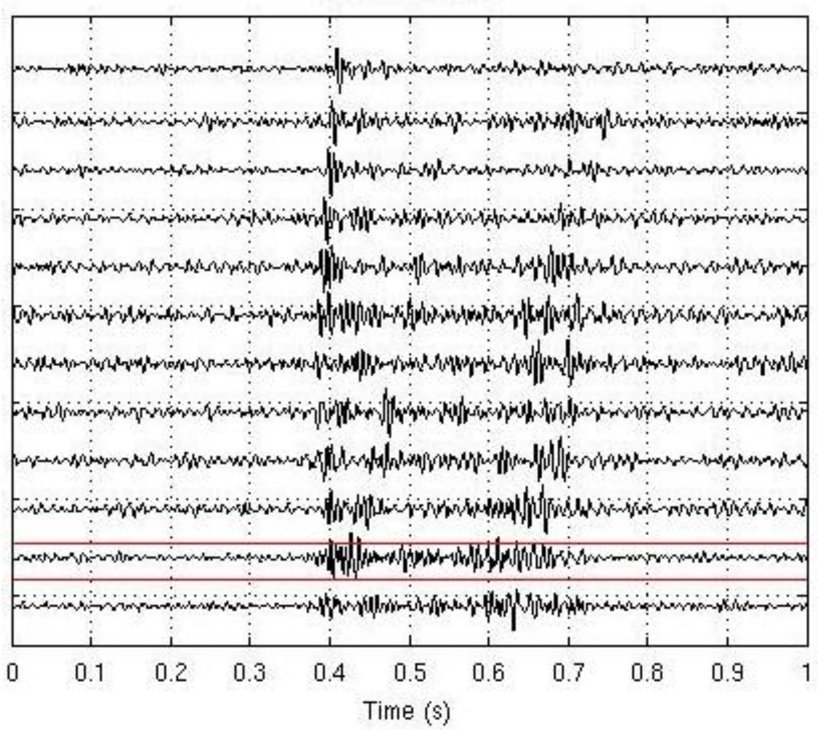

Figure 6-16: Filtered seismic traces of Z component, (35-200 Hz Butterworth) filter.

6.3 Signal Enhancement Operator

In many cases the seismic signal (event) and background noise occupy the same frequency band and have similar energy levels in microseismic data. As a result, frequency filtering and traditional “Short Term, Long Term Averaging” (STA/LTA) methods are not optimal for detection of the weak phases of a microseismic event. I used a cross product operator “M” and transformed spectrogram methods “S’ in time and frequency domain, for detection and enhancement of the microseismic events. These two operators are sensitive for linear polarization and high energy contrast of the seismic phase in microseismic events.

Several filter operators have been defined (Shimshoni and Smith 1964, Phinney and Smith 1963) in the time domain of the seismogram. In this study, I used an operator “M”, proposed by Shimshoni and Smith, (1964). This operator calculates as cross product of vertical and horizontal components of microseismic signal. This “cross product” operator gives a measure of the rectilinearity and total signal power of the seismic signal that can be expressed as:

$$M_j = \sum_{i=-n}^{n} H_{i+j} V_{i+j}$$

............***Equation 6-1***

In the frequency domain, a new spectrogram analysis and associated characteristic function are used to pick weak seismic events on microseismic data. This method has been implemented as transformed spectrum “S”, as describe by Song (2010). The main benefit of the transformed spectrogram based phase detection is that besides current energy term, it incorporates an “energy jump term” to capture high energy contrast (Fig 6-17, e and f). The transformed spectrogram can be expressed as:

$$\boldsymbol{S(f,t) = (log[B(f,t,L)] - log[B(f,t-L,L)log[B(f,t,L)]}$$

and,

$$\boldsymbol{B(f,t,L) = A(f,t,L)/min\{f,t\}A(f,t,L}$$

The characteristic function of this transformed spectrogram is defined over the signal frequency range $[f_1, f_2]$ as,

$$\boldsymbol{S([f_1,f_2]t) = max\left\{\frac{1}{N_f}\sum_{f_1}^{f_2} S(f,t), 0\right\}}\text{............}\textit{\textbf{Equation 6-2}}$$

Where N_i is the number of frequency points over the microseismic signal frequency range $[f_1, f_2]$.

Figure 1, a,b,c shows the vertical and horizontal seismograms selected from recorded data. The cross product operator “M” calculated by the time averaged cross product of two seismic traces in time domain (Fig 6-17, d).

In frequency domain, the transformed spectrogram based characteristic function can be used to choose an optimal frequency range to reduced noise in poor signal/noise ratio examples are represented (Fig 6-17, e,f).

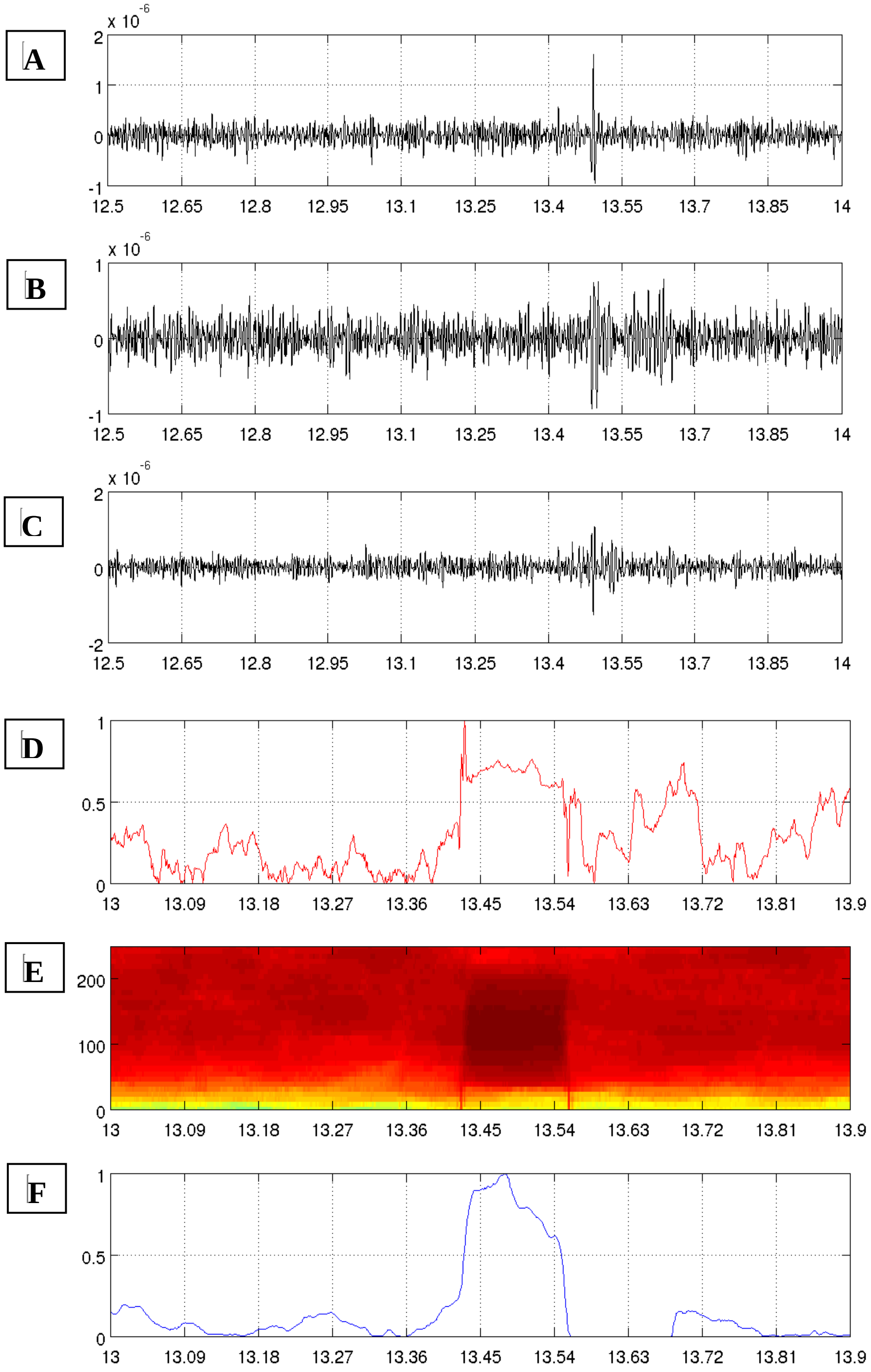

Figure 6-17: Three component (Vertical, Horizontals) microseismic data include a weak seismic event (a,b,c), Operator "M" calculated by cross product of the vertical and horizontal of seismic traces (d) and transformed spectrogram "S" calculated according to equation 6-2, (e, f).

The functions “M” and “S” (Figure 6-18) show a good indication of the presence of groups of signals but less time resolution for long window length. To obtain a more familiar form of display in which the individual phases can be recognized, the calculated “M” and “S” operators are multiplied by the original signal, where microseismic signal (event) is enhanced. In figure 6-18, “M” & “S” are multiplied by original seismograms calculated on figure 6-17.

No phase shift was observed in the short window length for both operators. In both methods, the uncertainly in picking the first arrival of signal energy is directly proportional to integration time. Trial and error procedures were used to establish a reasonable compromise for the integration time such that noise was suppressed but large time uncertainties were not introduced. The enhancement operator (M) was later applied to the previously filtered seismic waveforms. Figures 6-20, 6-21, 6-22 show an enhanced seismogram after applying the (M) operator.

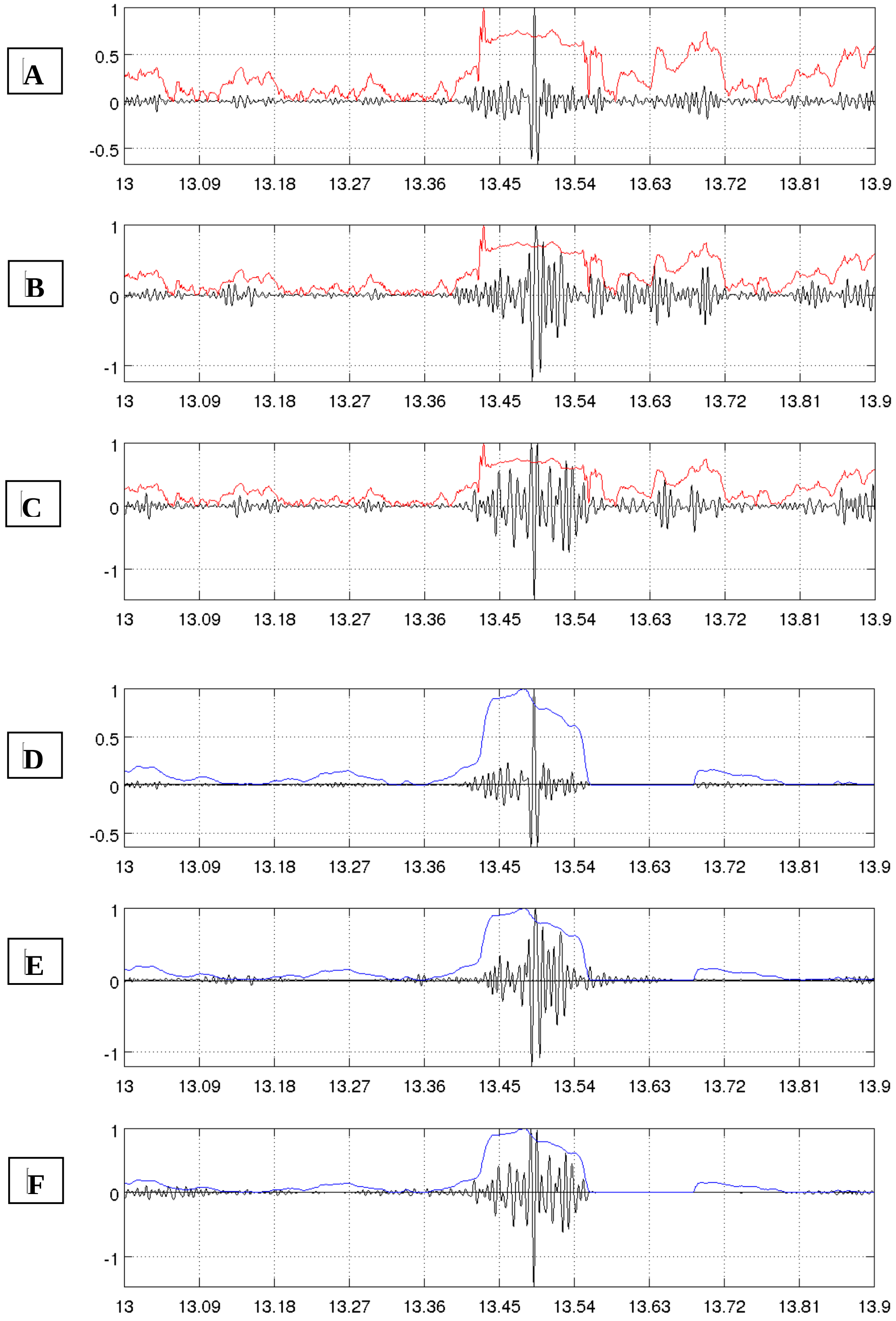

Figure 6-18: The vertical and horizontal components of enhanced microseismic event. Cross Product operator (red color) and transformed spectrogram (blue color) plots are superimposed on enhanced data.

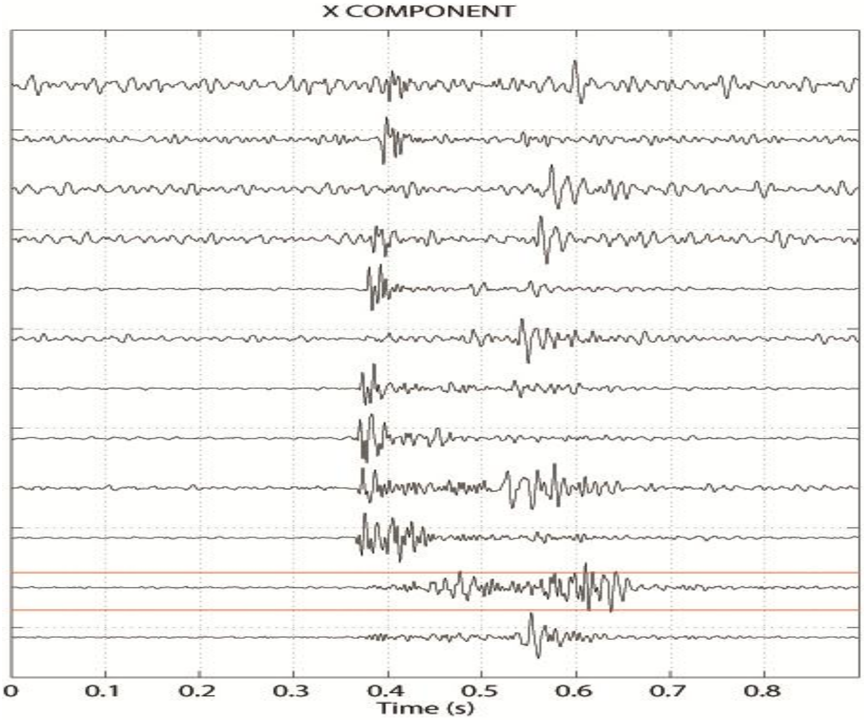

Figure 6-19: Filtered seismic traces (35-200 Hz Butterworth) and enhanced using enhancement operator on X component.

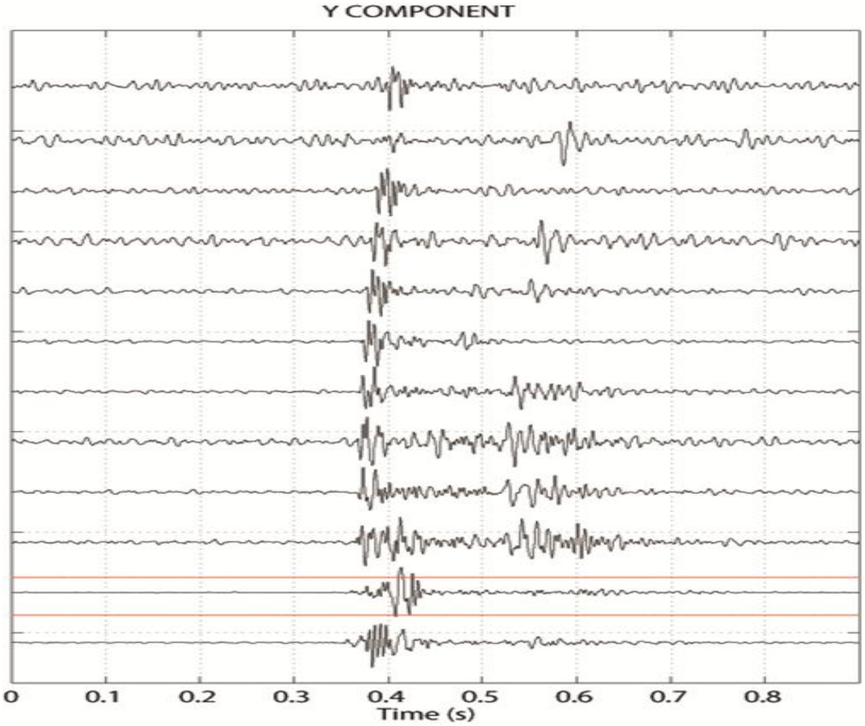

Figure 6-20: Filtered seismic traces (35-200 Hz Butterworth) and enhanced using enhancement operator on Y component.

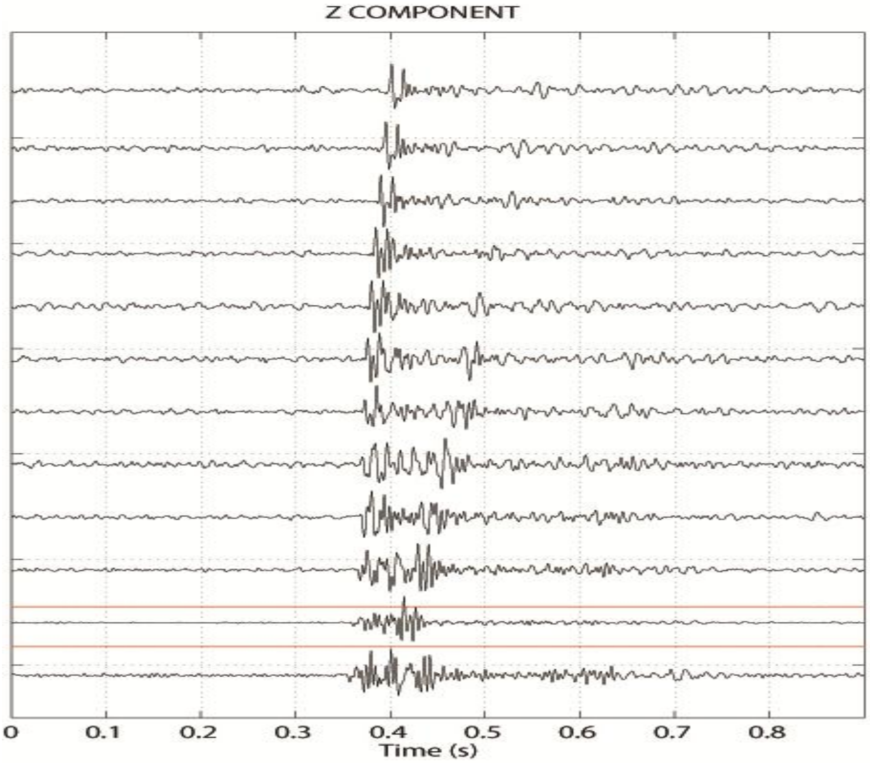

Figure 6-21: Filtered seismic traces (35-200 Hz Butterworth) and enhanced using enhancement operator on Z component.

6.4 STA-LTA event detection

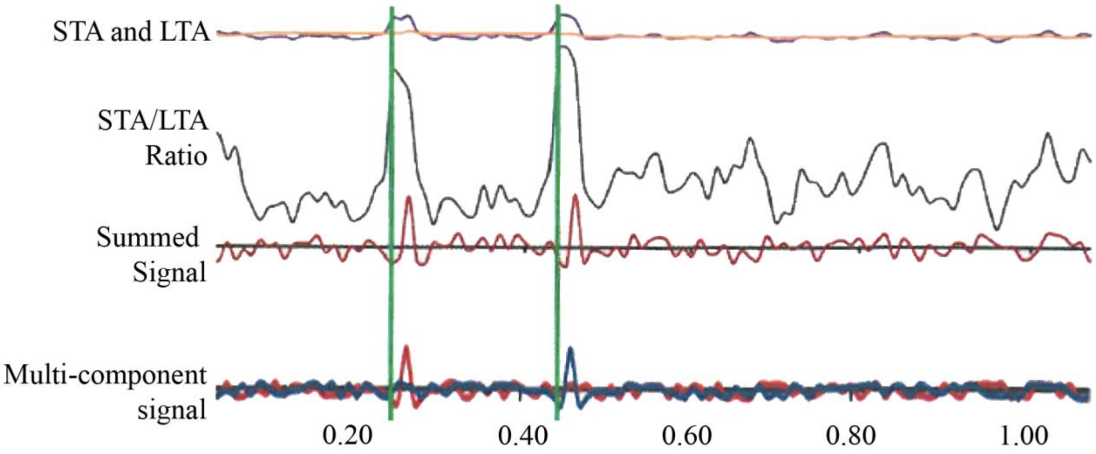

Figure 6-22: Demonstration of STA/LTA detection. Long term average (LTA) is the orange line overlaying short term average (STA) curve (blue). STA/LTA ratio showing in black, green vertical line represents the points where the ratio exceeds the specified flagging value. Original Synthetic signal at the bottom, with P-wave (red) and S-Wave (blue). (Maxwell, 2014)

First step in processing workflow is events detection. Numbers of common detection technique could be applied to preconditioned traces. One of the most common approaches is Short-term Average over Long-Term Average (STA/LTA. The purpose of this technique is to detect events based on amplitude spikes. Average amplitude is calculated over two different time windows, short term and long term windows, and the average between the two windows is called (STA/LTA). Once the ratio between the two windows exceeded certain value an event time is registered (figure 6-22). In this method there are five parameters to set:

- STA- window length in time
- LTA- window length in time
- STA/LTA events trigger threshold level
- STA/LTA events detrigger threshold level.
- Relative position between the STA and the LTA windows

The first two parameters are the two time windows over which the averages of the amplitudes are calculated. STA is an average over a short time window and LTA is an average over a long time window. The second two parameters are the value of ratios that trigger and detrigger the registration of an event. When the STA/LTA exceeds a certain value (the trigger threshold level), the time is registered as the beginning of an event. When the STA/LTA reaches a value below detrigger threshold level, the time is registered as the end of an event. The parameters need to be chosen carefully to fit the type of waveforms that are the target events. The STA time window needs in general to be a few periods longer than the expected dominant period of a target event (Trnkoczy, 1998). By choosing a short LTA we make the trigger more sensitive to short lasting local events with high frequency. If you were to be interested in long period low frequency earthquake signal, the LTA would need to be longer (Trnkoczy, 1998).

When the LTA is much longer than the longest duration of an event it represents the average background noise level, and will not be very sensible to sudden changes in the amplitude (Ambuter & Solomon, 1974). The STA will quickly respond to an increase in amplitude. As you move in steps across the seismogram, continuously calculating the STA and the LTA, the STA/LTA will have a value close to one when there are no events, but it will increase suddenly when an event occurs and the value of STA increases while the LTA stays close to the same.

6.5 Velocity Calibration

I selected a transverse isotropy velocity model as an initial model. The model parameters were driven from the anistropic parameter estimation analysis described in section 7.4. Figure 6-23 shows the recorded perforation shot and the modeled time arrivals based on the Transverse Isotropy intial velocity model (refer to chapter 7). The use of anisotropic initial velocity model has improved significantly the misfit between the observed and modeled time arrivals compare to isotropic velocity models, however it has not led to a full match (Figure 6-23.)

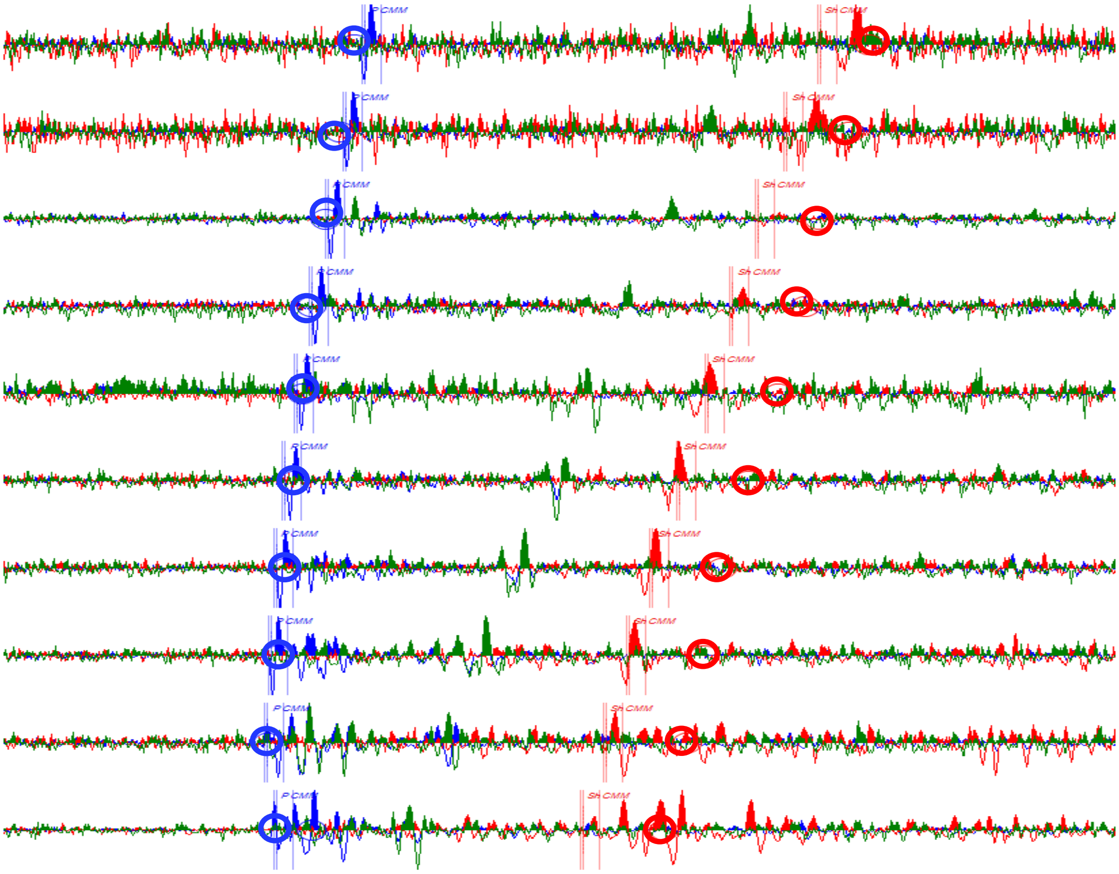

Figure 6-23: An example of recorded perforation shot from hydraulic fracture stage #9. P events picks are labeled in blue and Shear events are labeled in red. Modeled arrival time, based on un-calibrated transverse isotropic velocity model, are labeled in circle (   ) based on Picked events are labeled in lines (   ).

The usual assumption that the VTI model with the three Thomsen parameters would fully describe the subsurface is not accurate. Any triggered events, in general, travels a significant distance through a reservoir and non-reservoir rocks, each with its own anisotropic behavior. My experiment ray paths travel mainly through shale and sandstones formations. Sandstones are more likely to be quite isotropic, whereas the shale is generally highly anisotropic, which has been observed on section 7.4, due to its intrinsic layered texture. Also, incorrect geometry between the treatment and monitor wells is another common source of time differences which is contributing in our case. To overcome those sources of error, initial velocity model is calibrated using the perforation shot information Figure 6-24, 6-25.

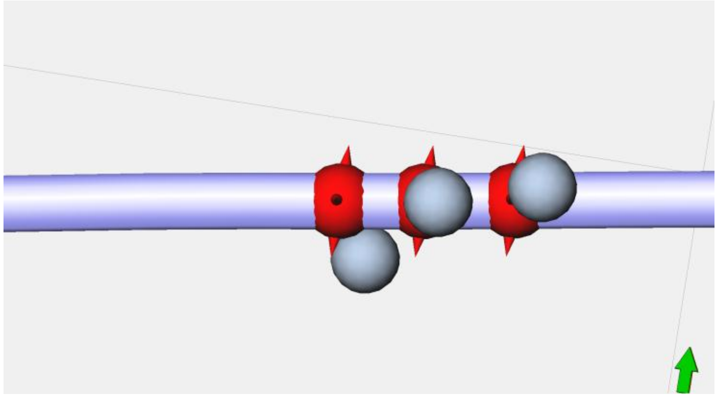

Figure 6-24: shows a relocated perforation shot after velocity model calibration in blue, actual perforation shot in red.

.

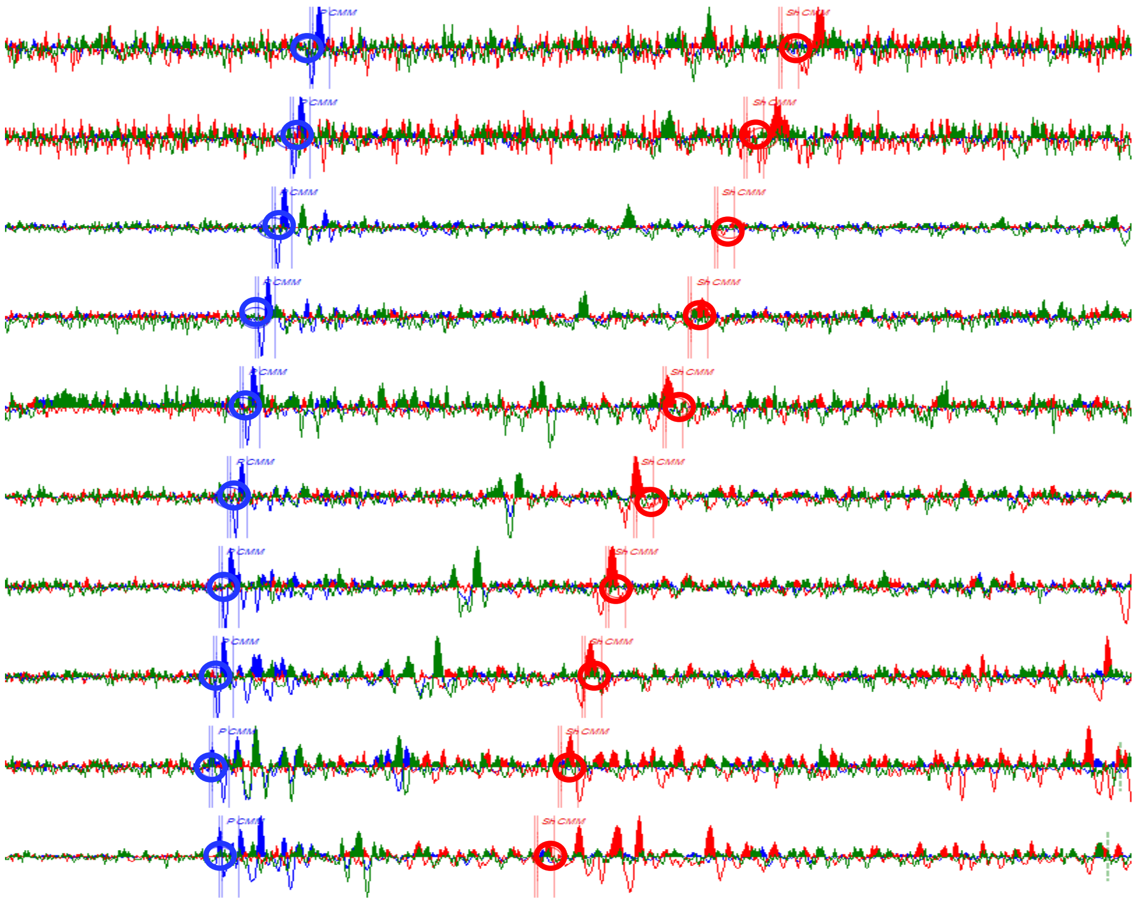

Figure 6-25: An example of recorded perforation shot from hydraulic fracture stage #9. P events picks are labeled in blue and Shear events are labeled in red. Modeled arrival time, based on calibrated transverse isotropic velocity model, are labeled in circle ( ) and picked events labeled in lines ( ).

The more calibration shots information utilize the better the velocity model. One key challenge with this dataset was the limited number of recorded/ perforation shots information. Stage 9 was the only stage where a high S/N, clear perforation shots information were observed. Monitoring geometry and its implication on waveform propagation pattern could the main reason in this case.

6.6 Hypocenter Locations Method

There are two approaches to solve hypocenter location problem, through either iterative or non-iterative algorithm. The main restriction and limitation with non-iterative methods is the assumption of a single velocity model, the assumption is necessary to keep the hypocenter location equation in the simplest form, which can be solved non-iteratively. Eq. 6-3 the simplest form of hypocenter location problem.

$$\sqrt{(x_i - x)^2 + (y_i - y)^2 + (z_i - z)^2} = v(t_i - t)$$

…. Equation 6-3

x, y, and z are the coordinates of the source, t is the origin time of the event, t_i is the arrival time at the i^{th} sensor, v is the wave propagation velocity.

Though, non-iterative methods are, in general, simple and easy to apply, in most cases their over-simplicity is not suitable, and then the alternative is the iterative method. The iterative approach covers a large variety of algorithms, from empirically based sequential searching to highly sophisticated derivative methods. One of the most common hypocenter location iterative approaches is the Geiger's method which I implemented and included in the scope of this project.

Geiger Method:

Geiger's method (Geiger, 1910, 1912) was developed in the early 1900s and has become as the classical source location method. It is an example of the Gauss-Newton's method (Lee and Stewart, 1981), a classical algorithm for solving nonlinear inverse problems. Geiger's method is the most common and widely used technique for hypocenter locations problem. Its solution is a location that has minimum error between observed (measured) and modeled travel times.

Geiger Algorithm:

In simple terms, the solution of the hypocenter location problem can be considered as an estimation of the spatial parameters, and time of origin (model parameters) from observed time arrivals from recorded events. We have a microseism source (hypocenter), with source parameters (**X, Y, Z and t_o**) and set of arrival times "**T_k, k= l, 2… m**" on "**m**" stations. Where, **"t_o"** is origin time of the source; and the seismic velocity model is assumed known. First, let x represent source parameters:

$$x = (t, x, y, z)^T$$

A trial model vector is assumed, where X* is a trial solution, conventionally called initial guess. X* is either assigned or estimated from previous iteration, it is always known at the beginning of each iteration.

$$x^* = (t^*, x^*, y^*, z^*) \text{ ….. } \textbf{\textit{Equation 6-4}}$$

The theoretical arrival time $t_k(x^*)$ can be calculated from source to station using a given trial model vector with a known velocity model. Then the theoretical arrival time at the kth station is:

$$t_k(x^*) = T_k(x^*) + t^* \text{ …..} \textbf{\textit{Equation 6-5}}$$

Where $\mathbf{t^*}$ is the trial origin time.

If we assume the observed arrival time is $\mathbf{t_k}$, then the travel-time residual “$\mathbf{r_k}$” is calculated at the $\mathbf{k}^{\text{th}}$ station as:

$$r_k(x^*) = \tau_k - t_k(x^*)$$ ….. ***Equation 6-6***

$$= \tau_k - T_k(x^*) - t^*$$ ….. . ***Equation 6-7***

for k = 1, 2,…. m

This definition of the residual follows the convention established by Geiger.

As before, we define the residual vector:

$$r = [r_1(x^*), r_2(x^*), \ldots, r_m(x^*)]^T$$ …… ***Equation 6-8***

for k= 1, 2, …., m

$$\delta x = (\delta t, \delta x, \delta y, \delta z)^T$$ ….. ***Equation 6-9***

Throughout the iterative process we try to solve the equation:

$$A^T A \delta x = -A^T r$$ ….. ***Equation 6-10***

Here A is the Jacobian matrix which expressed as:

$$\boldsymbol{A} = \begin{bmatrix} \frac{\partial r_1}{\partial x} & \frac{\partial r_1}{\partial y} & \frac{\partial r_1}{\partial z} & \frac{\partial r_1}{\partial t} \\ \vdots & & & \vdots \\ \frac{\partial r_m}{\partial x} & \frac{\partial r_m}{\partial y} & \frac{\partial r_m}{\partial z} & \frac{\partial r_m}{\partial t} \end{bmatrix}$$ …… ***Equation 6-11***

Using the arrival time residuals $\mathbf{r_k}\,(\mathbf{x}^*)$ and evaluating the partial derivatives, the Jacobian matrix becomes:

$$A = \begin{bmatrix} 1 & \frac{\partial T_1}{\partial y} & \frac{\partial T_1}{\partial z} & \frac{\partial T_1}{\partial x} \\ & & & \vdots \\ 1 & \frac{\partial T_m}{\partial y} & \frac{\partial T_m}{\partial z} & \frac{\partial T_m}{\partial x} \end{bmatrix}$$

……Equation 6-12

we can write the generalized solution of the least square equation:

$$A\delta x = r$$ ***……Equation 6-13***

This formula for the adjustment (solution) vector "δx" will be used repeatedly until the change in the solution become less than some specified amount, or until a certain number of iterations have been completed.

Summary of Geiger's Method: (from Lee, and Dodge, 1992).

I. Guess a trial origin time t", and a trial hypocenter (X*, Y*, Z*).

II. Compute the theoretical travel time and its spatial partial derivatives evaluated at (x*, y*, z*) from the trial hypocenter to the kth station for all k.

III. Compute matrix A and vector r

IV. Solve the system of linear equations for the adjustments δt, δx, δy, δz.

V. An improved origin time is then given by t*+ δt, and an improved hypocenter by (x* + δx, y* + δy, z* + δz).

VI. Repeat steps 2 to 5 until some stopping conditions are met. At that point, set t0 = t", x0 = x*, y0 = y*, and z0 = z* as the solution to the problem.

Geiger's method is sensitive to the initial guess of model parameters. If we start the search for the proper initial guess, adjustments vector will move to direction where the solution will converge to solution space.

CHAPTER 7:

VELOCITY MODEL CALIBRATION

Microseismic spatial location strongly depends on the accuracy and suitability of the velocity model used for arrival time analysis. In most cases, velocity models are typically built from measured sonic velocities acquired through number of sonic logging tools that can determine compressional and shear velocities. However, those tools are measuring along the wall of the borehole, which crossponds to either the vertical velocity as in most the wells, or horizontal in others. Meanwhile most of sedimentary rocks especially shale, driven by layering, mineralogy, and natural fracturing, exhibit a significant degree of velocity transverse isotropy (Thomsen 1986) resulting in a more complex velocity structure. As a result, vertical velocity models (sonic based) give a good initial model for microseismic processing, but are inappropriate for final microseismic location estimations as they will result in large errors in the estimated microseism source locations.

One approach is to include estimated anisotropy parameters on the initial model, which would partially minimize large errors but not fully resolve the observed time arrivals misfit. The optimal solution is to calibrate based on the calibration shot which is usually a perforation or string shot; calibration can be done based on isotropic or transverse isotropic parameters model. Velocity Calibration’s main concept is to invert for effective velocity model that would relocate perforation shot to its actual know location and minimize the arrival times misfit between observed and model times. The following sections will cover isotropic and transverse isotropic media parameters, and their applications on microseismic velocity calibration.

7.1 Isotropic Media Parameters

The main assumption of isotropic models is that all directions are equivalent. Such materials are characterized by only two independent elasticity constants for compressional and shear, and all other coupling terms of the stiffness matrix are null (Figure 7-1)

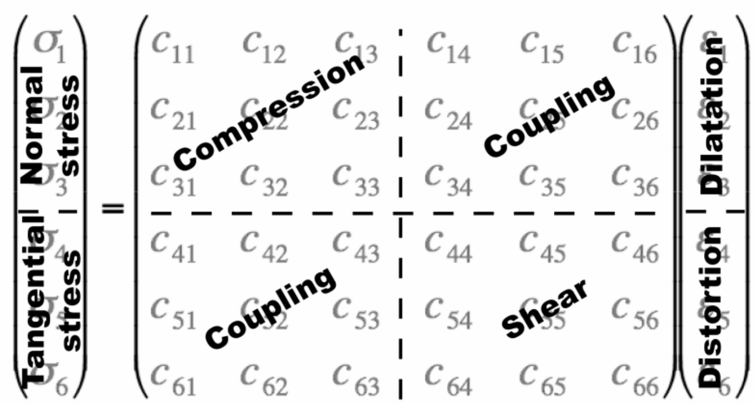

Figure 7-1: Stiffness matrix parameters describing an isotropic medium.

Rocks would behave as an isotropic media, if they are uncracked, intrinsically isotropic, randomly cracked, or with random crystals or grains orientations (Crampin, 1989).

$$C_{ISO} = \begin{pmatrix} C_{11} & C_{11}-2C_{66} & C_{11}-2C_{66} & 0 & 0 & 0 \\ C_{11}-2C_{66} & C_{11} & C_{11}-2C_{66} & 0 & 0 & 0 \\ C_{11}-2C_{66} & C_{11}-2C_{66} & C_{11} & 0 & 0 & 0 \\ 0 & 0 & 0 & C_{66} & 0 & 0 \\ 0 & 0 & 0 & 0 & C_{66} & 0 \\ 0 & 0 & 0 & 0 & 0 & C_{66} \end{pmatrix}.$$

Equation 7-1

C_{IJ} can be expressed in term of the Lamè constants:

$$\lambda = C_{11} - 2C_{66}\,, \quad \text{and} \quad \mu = C_{66}\,,$$

P- and S-wave velocities of the isotropic media are expressed in term of the Lamè parameters as follow:

$$V_P = \sqrt{\frac{\lambda + 2\mu}{\rho}} \quad \text{and} \quad V_S = \sqrt{\frac{\mu}{\rho}}\,.$$

Vp and Vs of an isotropic model are determined by most of the sonic logging tools.

7.2 Effective Isotropic Velocity Calibration

Effective isotropic velocity model calibrations are one of the common techniques for velocity model calibration in microseismic processing. An adjustment of the vertical compressional (Vp) and shear velocities (Vs) is applied to relocate the calibration event (string shot, or perforation shot) to the right spatial location, adjustment can be either a bulk shift or variable adjustment to the velocity profile. Though this type of calibration can relocate perforation shots with a sufficient accuracy; inaccuracies will be a challenge upon significant growth away (either in height or distance) from the treatment borehole, or when the model is used for another treatment stage away from where it was calibrated, unless multiple calibrated models are used for each stage.

Though this method does not directly account for the anisotropic nature of shales, using a repeatedly calibrated effective isotropic velocity model in every stage can account, in certain array designs, for the effects of anisotropy. The main advantage of this approach is simplicity; however, the main concern is that it could give rise to unrealistic formation velocities to overcome time discrepancies that are usually inherited from anisotropy and acquisition geometry.

7.3 Hexagonal Anisotropic Media Parameters

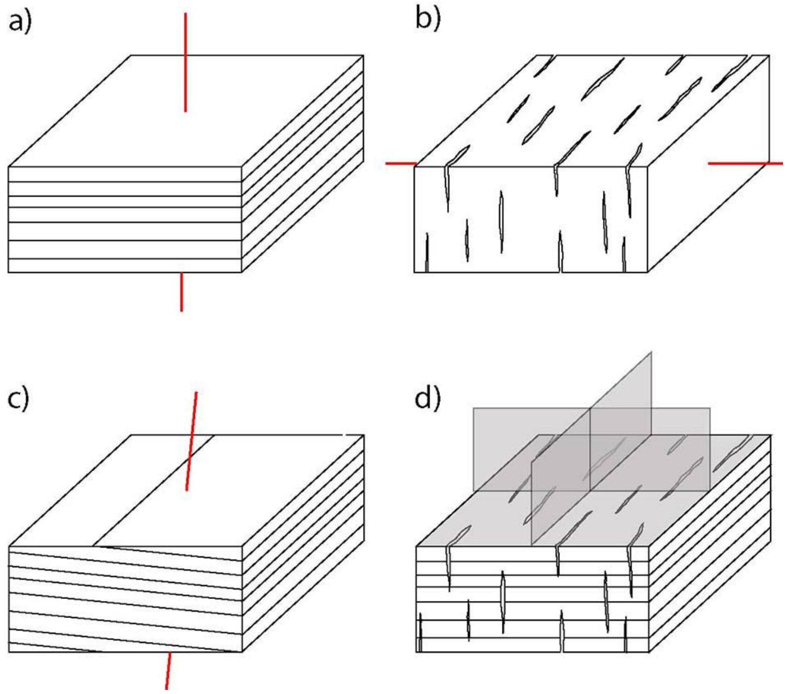

Figure 7-2: a) VTI anisotropic model (fine layered rocks); b) HTI anisotropic model (vertical parallel fractures in a homogeneous medium); c) TTI anisotropic model (tilted thin layering); d) Orthorhombic symmetry system (vertical fractures in a VTI medium lead). Axes of symmetry are depicted in red.

An axis of rotational symmetry characterizes hexagonal anisotropic media. Since all directions in a plane orthogonal to the symmetry axis are equivalent, this plane is called symmetry-axis plane (Grechka, 2009). Transversely isotropic (TI) media belong to the hexagonal symmetry system. In TI media, velocities are rotationally invariant around the symmetry axis. The orientation of the symmetry axis defines different TI media, i.e. vertical transverse isotropy (VTI), horizontal transverse isotropy (HTI), and tilted transverse isotropy (TTI). Examples of VTI, HTI, and TTI media are depicted in figure (7-3). In geophysical contexts, TI is the simplest anisotropic mechanism.

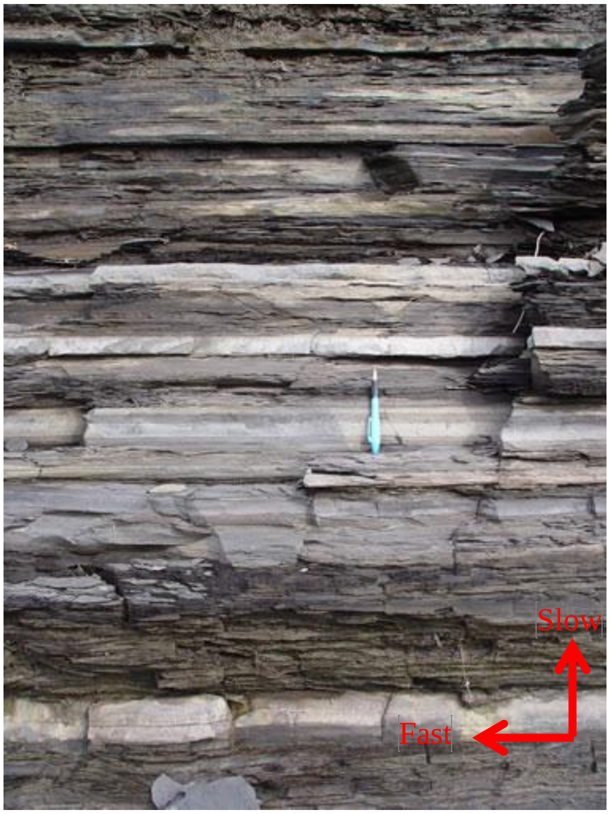

Figure 7-3: Utica Shale outcrop as an example of a fine-layered shale formation. Writing pen is for scale. (after National Energy Board, 2009)

VTI is, unarguably, the most common anisotropic model considered by the hydrocarbon industry. In fact, it is often a suitable mechanism to describe the properties of sedimentary basins, which are the most typical geological structure in hydrocarbon settings (e.g. Winterstein and De, 200). Elastic stiffness coefficients are conveniently used to define the material properties in forward modeling algorithms.

$$C_{VTI} = \begin{pmatrix} C_{11} & C_{11}-2C_{66} & C_{13} & 0 & 0 & 0 \\ C_{11}-2C_{66} & C_{11} & C_{13} & 0 & 0 & 0 \\ C_{13} & C_{13} & C_{33} & 0 & 0 & 0 \\ 0 & 0 & 0 & C_{44} & 0 & 0 \\ 0 & 0 & 0 & 0 & C_{44} & 0 \\ 0 & 0 & 0 & 0 & 0 & C_{66} \end{pmatrix}.$$

Equation 7-2

Seismic velocities of a VTI media is described by 5 independent elasticity constants, and the phase velocities of the three wave modes which are well approximated by (Daley and Hron, 1977; Thomsen 1986) VTI media are completely described by five independent elastic constants and the stiffness matrix is:

$$v_{\mathrm{P}}^2(\theta) = \frac{1}{2\rho}\left[C_{33} + C_{44} + \left(C_{11} - C_{33}\right)\sin^2\theta + D(\theta)\right],$$

$$v_{SV}^2(\theta) = \frac{1}{2\rho}\left[C_{33} + C_{44} + \left(C_{11} - C_{33}\right)\sin^2\theta - D(\theta)\right],$$

$$v_{\mathrm{SH}}^2(\theta) = \frac{1}{\rho}\left[C_{66}\sin^2\theta + C_{44}\cos^2\theta\right],$$

Equation 7-3

Where

$$\begin{aligned} D(\theta) = \Big\{&(C_{33} - C_{44})^2 + \\ &+2\left[2(C_{13} + C_{44})^2 - (C_{33} - C_{44})(C_{11} + C_{33} - 2C_{44})\right]\sin^2\theta + \\ &+\left[(C_{11} + C_{33} - 2C_{44})^2 - 4(C_{13} + C_{44})^2\right]\sin^4\theta\Big\}^{1/2}, \end{aligned}$$

Equation 7-4

ρ is the bulk density of the rock and θ is the phase angle, being the angle between the wave front normal and the axis of symmetry.

The stiffness matrix notations are suitable for descriptions of seismic modeling theories and algorithms but inconvenient for seismic processing and inversion. In 1986, Thomsen has shown that complex systems of equations for the general case of transverse isotropy could be simplified based on weak anisotropy assumption. Based on that, formations can be described based on P-wave, S-wave velocities and three anisotropy parameters (γ , ε , and δ). The three Thomson parameters are convenient notations to describe wave propagations in a linearly elastic, hexagonal medium with the axis of symmetry in the vertical direction (VTI).

P wave vertical velocity: $v_{P0} = \sqrt{\frac{C_{33}}{\rho}}$

S-wave vertical velocity: $v_{S0} = \sqrt{\frac{C_{44}}{\rho}}$

Thomsen Parameters:

$$\varepsilon = \frac{C_{11} - C_{33}}{2C_{33}}, \quad \gamma = \frac{C_{66} - C_{44}}{2C_{44}} \quad \text{and} \quad \delta = \frac{(C_{13} + C_{44})^2 - (C_{33} - C_{44})^2}{2C_{33}(C_{33} - C_{44})^2}.$$

Equation 7-5

Then velocity equations can be described as:

$$\begin{aligned} V_P(\theta) &= \alpha_0\left(1 + \delta\sin^2\theta\cos^2\theta + \varepsilon\sin^4\theta\right) \\ V_{SV}(\theta) &= \beta_0\left(1 + \frac{\alpha_0^2}{\beta_0^2}(\varepsilon - \delta)\sin^2\theta\cos^2\theta\right), \\ V_{SH}(\theta) &= \beta_0\left(1 + \gamma\sin^2\theta\right) \end{aligned}$$

Equation 7-6

Where,

V_P : P-wave velocity.

V_{SV} and V_{SH} : Orthagnal shear components.

α_0 : Vertical compressional vleocity (V_{P0}).

B_0 : Vertical shear velocity (V_{S0}).

γ , ε , and δ : Thomsen’s parametres,

θ : Phase angels for each of the velocity componenets.

7.4 Transverse Isotropy Parameters Estimation

The most commonly observed anisotropy in shales is vertical transverse isotropy (VTI), or polar anisotropy. Those type of anisotropy can be described by Thomsen parameters delta (δ), gamma (γ), and epsilon (ε) (Thomsen, 1986). Estimation of Thomsen parameter can be done through VSPs, Advance sonic tools, and core plugs. For long time, walk-a-way or multi offset VSPs have been used to estimate delta and epsilon parameters, and more recently it has been shown that gamma also can be estimated by advance sonic tools through cross dipole and stoneley analysis (Walsh et al., 2007). Core plugs, also, can be used to estimate Thomson's parameters but with higher uncertainty and sampling limitation compare to the other two methods.

Advanced sonic data and Walk-a-away VSP were available for my thesis. Anisotropy analyses of full waveform sonic logs (compressional, dipole, and Stoneley shear data) yielded continuous estimation of the Thomsen's gamma parameter (see Figure 7-5), and offset VSP data yielded estimation of Thomsen's epsilon and delta parameters (see table 7-1).

$$C_{33} = \rho_b V_P^2$$
$$C_{44} = \rho_b V_{S-slow}^2$$
$$C_{55} = \rho_b V_{S-fast}^2$$
$$C_{66} = \rho_b V_{S-stoneley}^2$$

$$\varepsilon = \frac{C_{11} - C_{33}}{2C_{33}}, \quad \gamma = \frac{C_{66} - C_{44}}{2C_{44}}$$

$$\delta = \frac{(C_{13} + C_{44})^2 - (C_{33} - C_{44})^2}{2C_{33}(C_{33} - C_{44})^2}$$

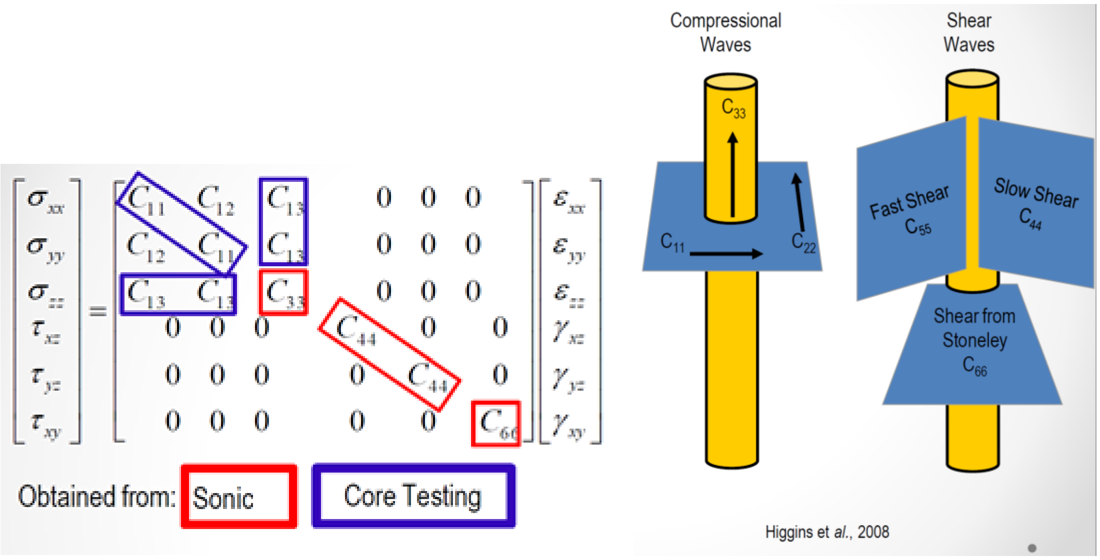

$$\begin{bmatrix}\sigma_{xx}\\ \sigma_{yy}\\ \sigma_{zz}\\ \tau_{xz}\\ \tau_{yz}\\ \tau_{xy}\end{bmatrix}=\begin{bmatrix}C_{11} & C_{12} & C_{13} & 0 & 0 & 0\\ C_{12} & C_{11} & C_{13} & 0 & 0 & 0\\ C_{13} & C_{13} & C_{33} & 0 & 0 & 0\\ 0 & 0 & 0 & C_{44} & 0 & 0\\ 0 & 0 & 0 & 0 & C_{44} & 0\\ 0 & 0 & 0 & 0 & 0 & C_{66}\end{bmatrix}\begin{bmatrix}\varepsilon_{xx}\\ \varepsilon_{yy}\\ \varepsilon_{zz}\\ \gamma_{xz}\\ \gamma_{yz}\\ \gamma_{xy}\end{bmatrix}$$

Figure 7-4: A schematic showing the measured parameters by a sonic tool in a vertical well, and the crossponding stiffness matrix.

.

Referenced Depth (0-1000)	**VP0, ft/s**	**Vp/Vs**	**Delta**	**Epsilon**
0 (Surface)				
580	10241	2.48	0.096	0.218
655	10525	2.61	-0.056	0.342
847	10121	2.81	-0.004	0.498
930	10661	2.67	-0.045	0.47
963	10050	2.58	0.019	0.392
988	12968	1.83	0	0

Table 7-1: Thomsen parameters estimated from a walk-a-way VSP data. Target zone is shaded in grey.

Shales are generally intrinsically anisotropic due to layering, mineralogy, and natural fracturing (Thomsen 1986), which result in a more complex velocity structure. Anisotropy data of target zone exhibit a very high gamma (γ) as estimated by advance sonic data (Figure. 7-5) which explains the large horizontal shift when processed with an Isotropic velocity model (Figure 7-12).

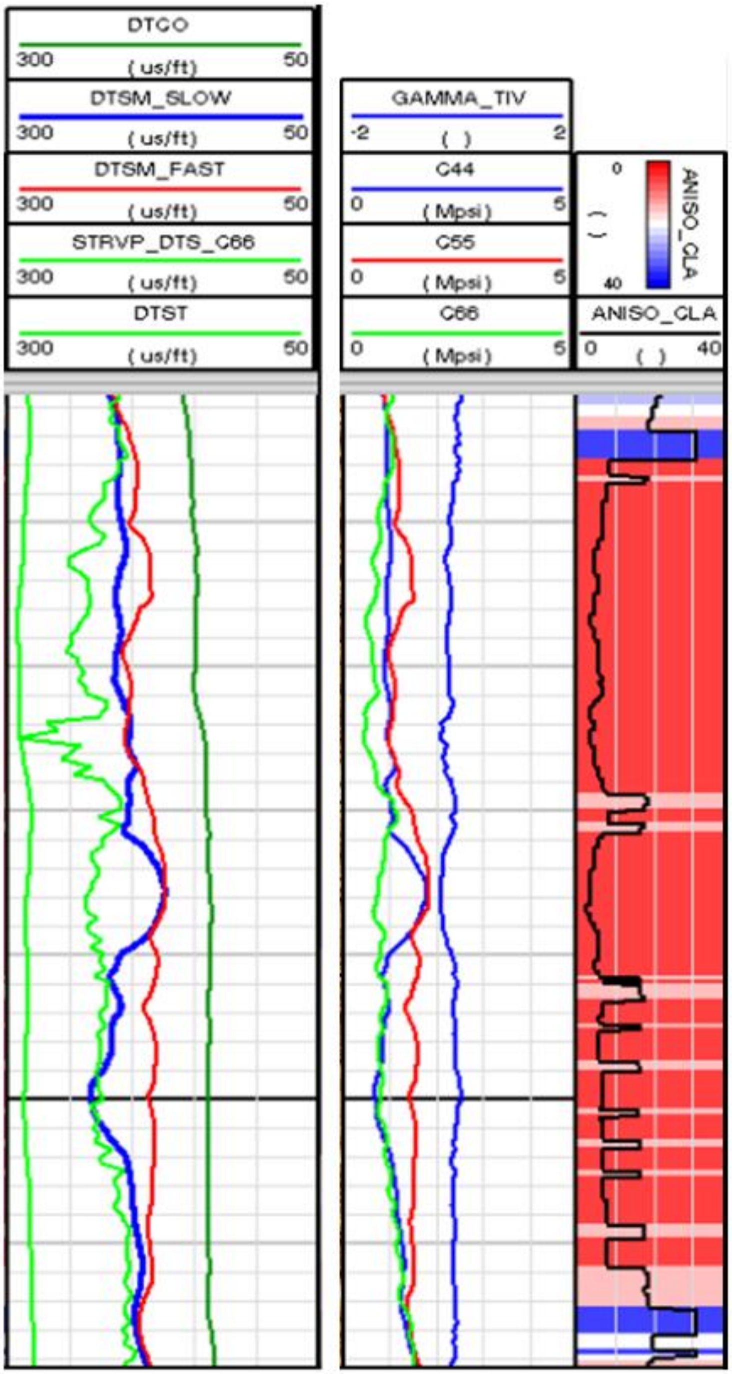

Figure 7-5: Sonic estimated stiffness matrix and Thomson's anisotropy parameter (Gamma) across the target zone.

7.5 Effective Transverse Isotropy Velocity Calibration

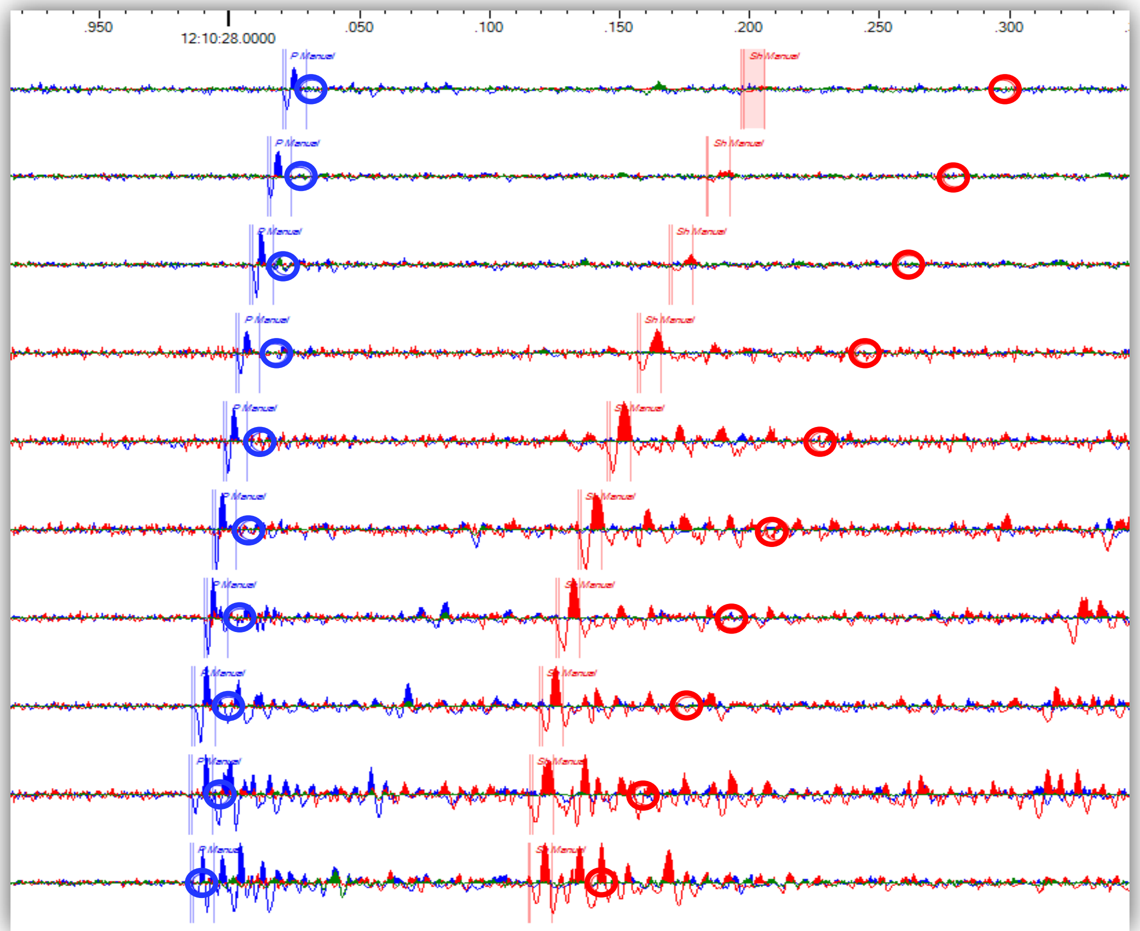

Figure 7-6: An example of recorded perforation shot from hydraulic fracture stage #9. P events picks are labeled in blue and Shear events are labeled in red. Modeled arrival time, based on un-calibrated isotropic velocity model, are labeled in circle (○) based on Picked events are labeled in lines ( ). |

Anisotropy has major implications on microseismic processing; number of approaches has been used to account for velocity anisotropy effects. These approaches include replacing vertical velocities with horizontal velocities-(if measured), modifying monitoring geometry to minimize anisotropy effects on ray path propagation, and assuming elliptical anisotropy. All those methods do not explicitly treat anisotropy, to correctly account for anisotropy; an anisotropic ray-tracer with calibrated anisotropy measurement must be incorporated into the velocity models (Warpinski et al., 2009). If an isotropic velocity model is used, then calibration efforts will treat both anisotropy effects, and incorrect geometry given rise to unrealistic formation velocities. The complete solution is to include anisotropy in the analysis through measurement of the anisotropy parameters, as done in section 7.4, and incorporate it in the initial velocity model. (Mizuno, 2010) Figure 7-9 shows the perforation shot of stage#9 with the estimated arrival times based on the anisotropic initial model.

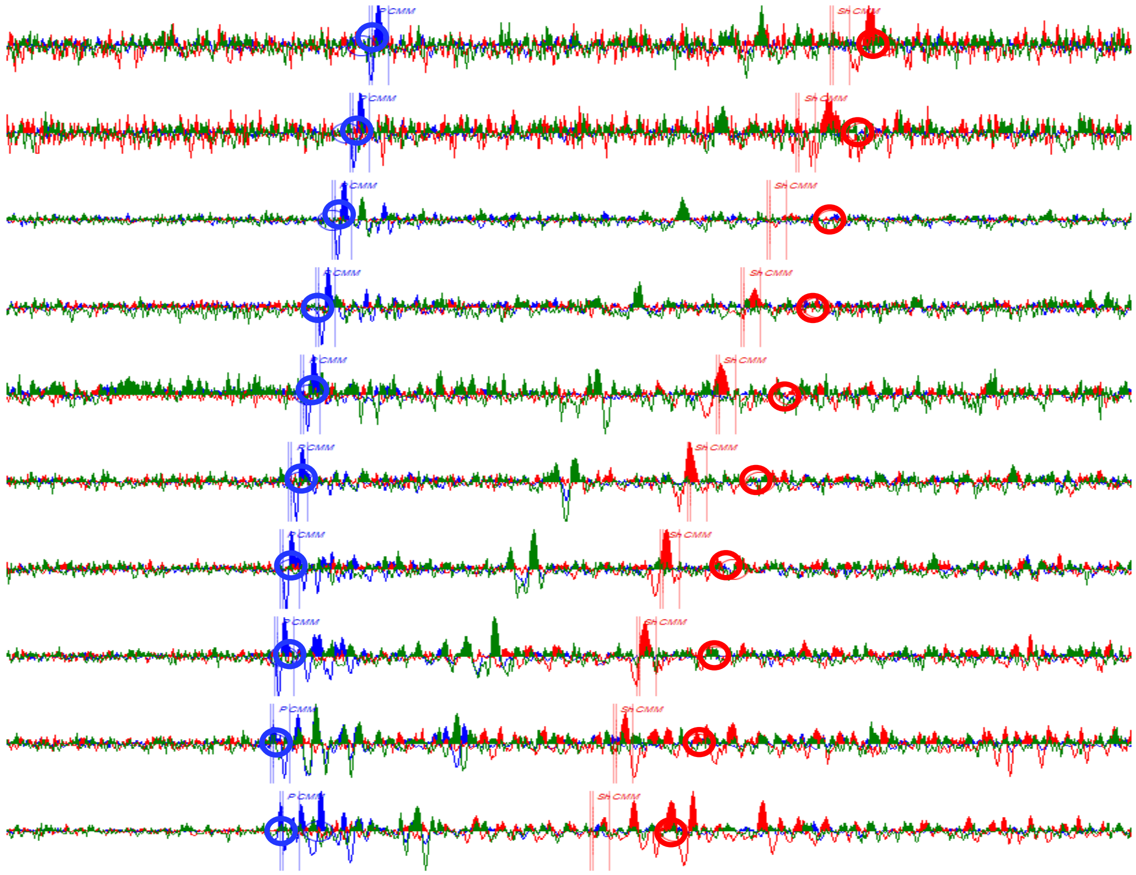

Figure 7-7: An example of recorded perforation shot from hydraulic fracture stage #9. P events picks are labeled in blue and Shear events are labeled in red. Modeled arrival time, based on un-calibrated transverse isotropic velocity model, are labeled in circle (○) based on Picked events are labeled in lines (❙).

The use of an anisotropic initial velocity model has reduced significantly the misfit between the observed and modeled time arrivals, however as expected it still didn't fully match the observed arrivals. The assumption that the VTI model with the three measured Thomsen parameters will fully describe the subsurface is not accurate. Any triggered events, in general, travels a significant distance through a reservoir and non-reservoir rocks, each with its own anisotropic behavior. My experiment ray paths travel mainly through shale and sandstones formations. Sandstones are more likely to be quite isotropic, whereas the shale is generally highly anisotropic due to intrinsic texture, which has been observed on section 7.4. Though the Qusaiba source rock is mainly shale, which is VTI in nature, it is populated with vertical natural fractures which complicates the situation and introduces a certain degree of an HTI to an orthotropic transverse isotropy system. Even if a VTI model will fully describe the velocity field, anisotropy remains one of the explanations of time discrepancies, incorrect geometry between stimulation and monitoring wells is another common source of time discrepancies. (Eisner, 2006)

The approach to overcome and correct for time arrivals misfit is to use an effective transverse anisotropy model. Perforation shots information are used to calibrate the initial TI velocity model. TI parameters are re-estimated after calibration based on the horizontal and vertical velocities. For the general case of vertical transverse isotropy (VTI), which typical found in massive shales, and in a nearly horizontal ($\theta = \pi / 2$) ray paths two of Thomson parameters (ε and γ) can be directly re-calculate based on the calibrated vertical and horizontal velocities as given by the equation (7.7).

$$\gamma = \frac{v_{SH}(\pi/2)}{\beta_0} - 1 \qquad \text{and} \qquad \varepsilon = \frac{v_P(\pi/2)}{\alpha_0} - 1 \ .$$

Equation 7-7

Where,

α_0 is the vertical compresional vleocity , & B_0 is the vertical shear velocity

In a nearly horizontal ray paths ($\theta = \pi/2$), δ has no impact on the horizontal velocity and only come into play as the $\cos^2(\theta)$ (Refer to Eq. 7-5 and 7-6).

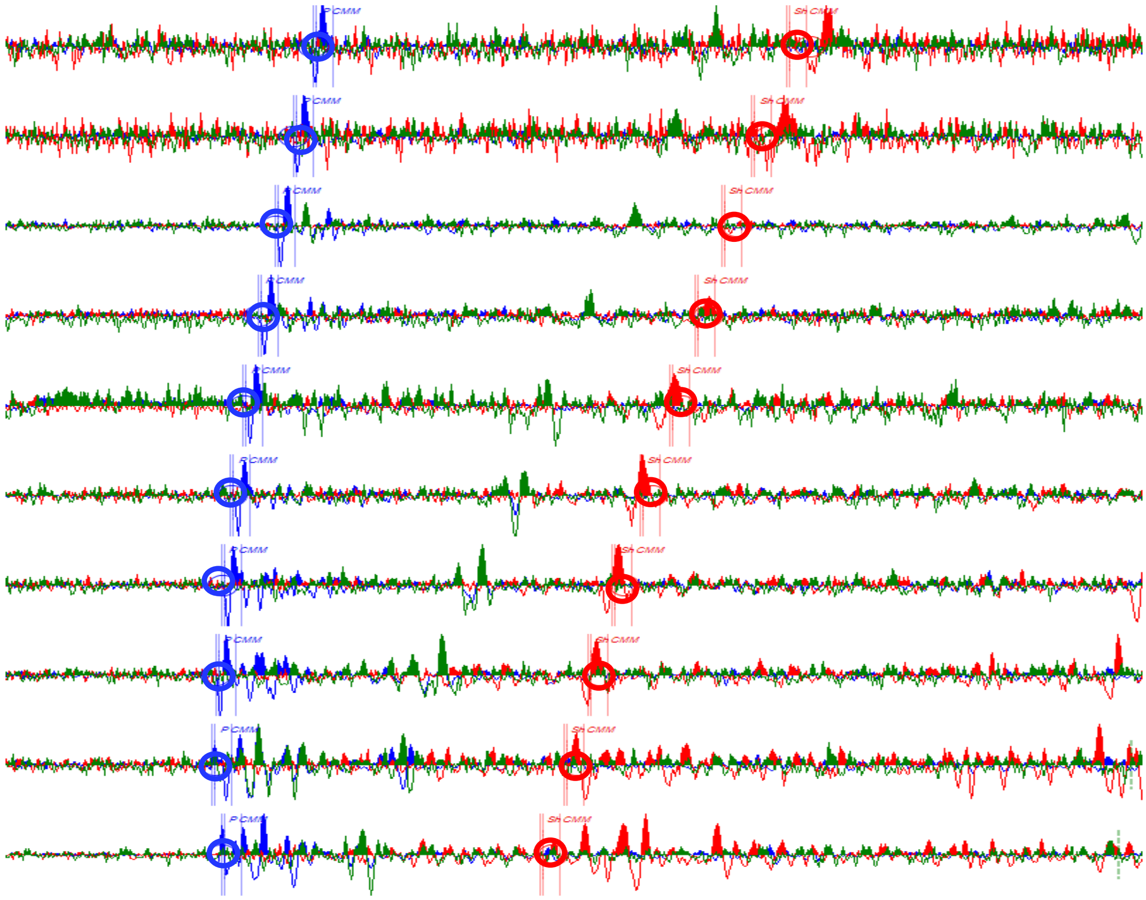

Figure 7-8: An example of recorded perforation shot from hydraulic fracture stage #9. P-wave events picks are labeled in blue and Shear events are labeled in red. Modeled arrival time, based on calibrated transverse isotropic velocity model, are labeled in circle (○) based on Picked events are labeled in lines (|).

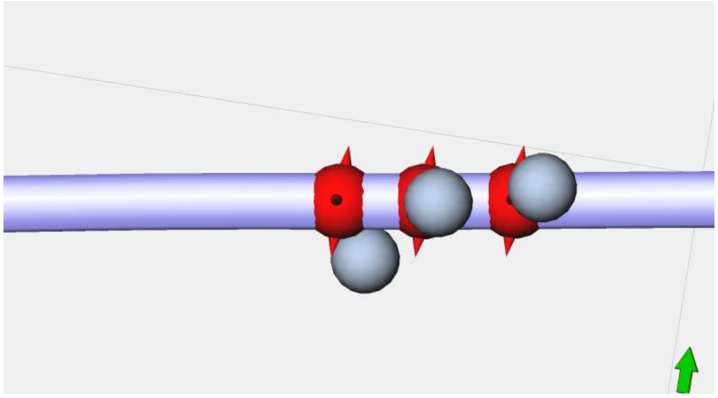

Figure 7-9: shows a relocated perforation shot after velocity model calibration in blue, actual perforation shot in red.

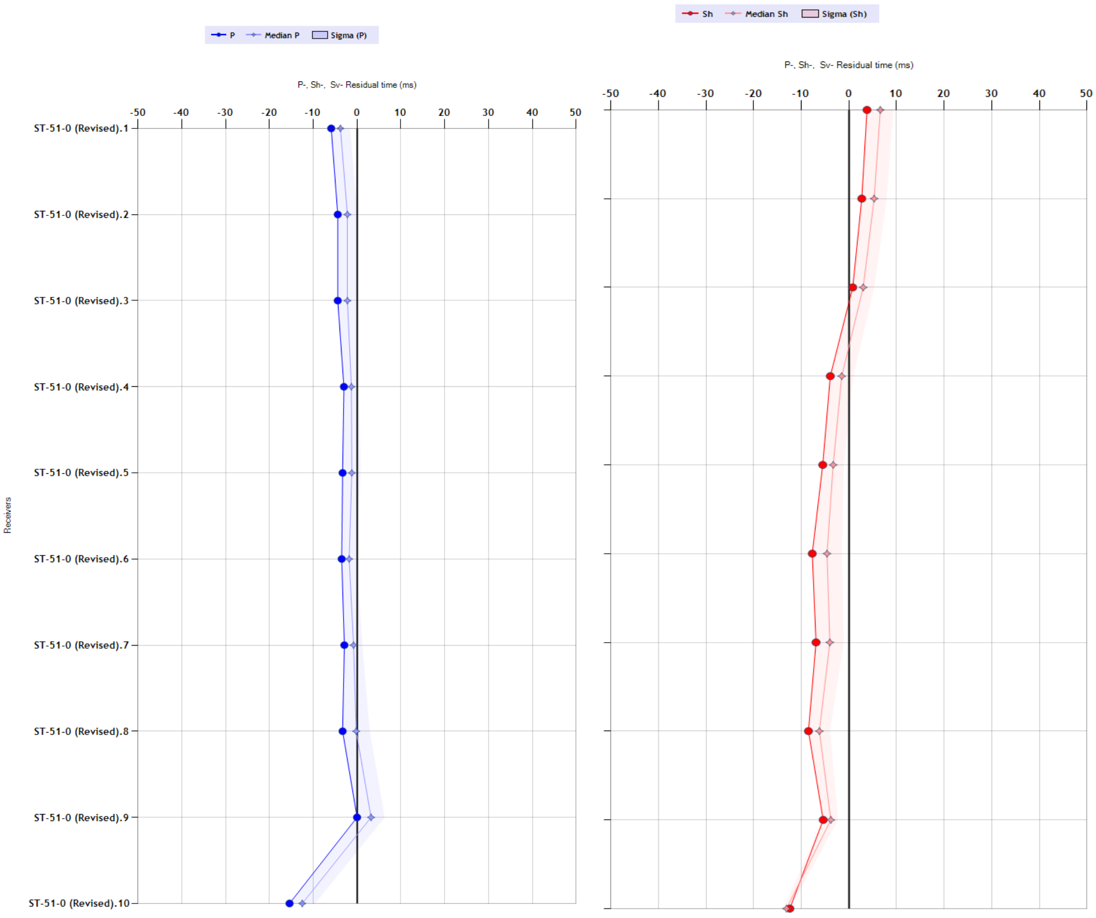

Figure 7-10: Residual time misfit analysis/plot of the P (blue), and Sh (red) between modeled and observed time arrivals for all sensors of the calibrated TI model.

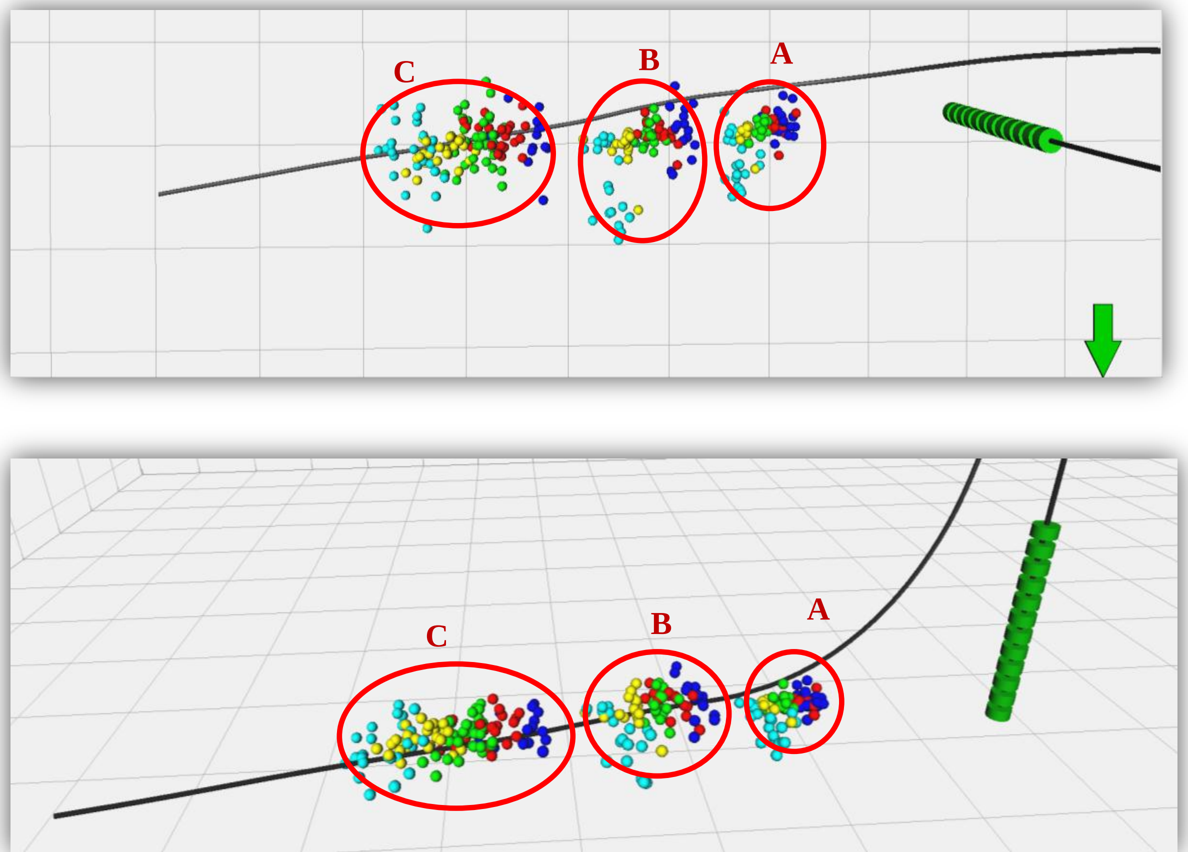

Figure 7-11: Hydraulic frack stages 5-10 recorded MS data processed with A) isotropic initial velocity model, B) transverse isotropic initial velocity model, C) calibrated transverse isotropic velocity model

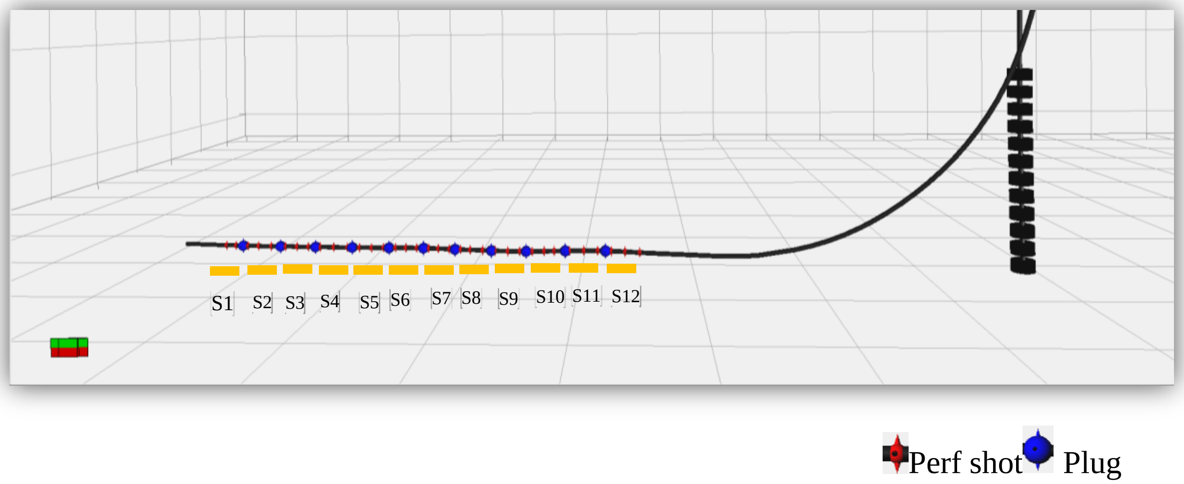

Figure 7-12: A cross-section view showing the geometry of downhole monitoring array relative to the perforation shots and frac stages.

Similar observations were reported by Erwemi et al., 2010, shows different hypocenter locations based on isotropic vs. anisotropic velocity models. Figure 7-13, show the hypocenter distribution of hypocenters locations based on both calibrated Anisotropic vs. uncalibrated Isotropic models. Lack of horizontal velocities in the isotropic model (red) results in an events distribution bias toward the monitoring well.

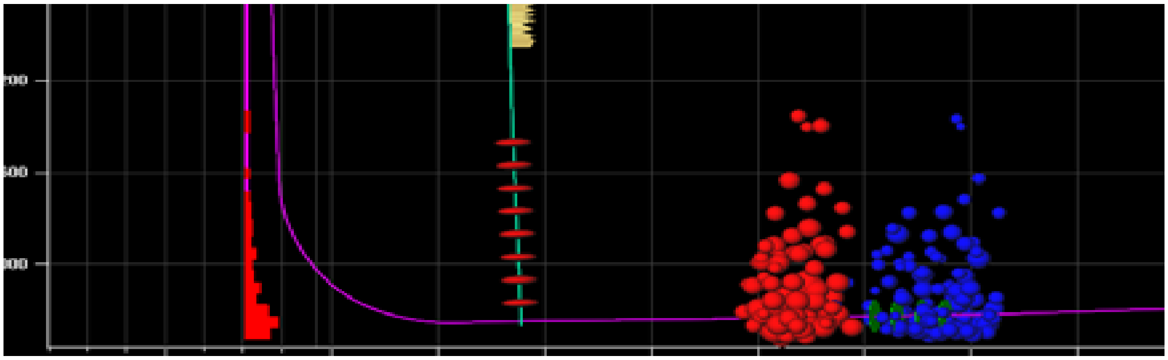

Figure 7-13: Microseismic locations for one stage of a multi-stage horizontal well stimulation, before (red) and after (blue) anisotropic calibration. After Erwemi et al., 2010

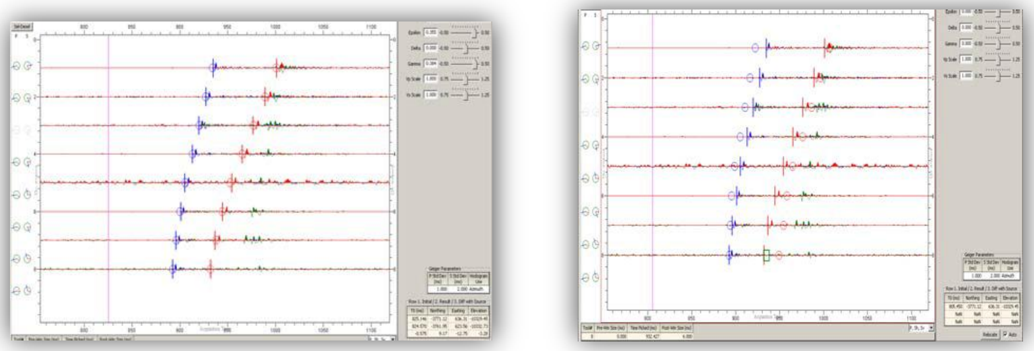

Figure 7-14: Modelled perforation shot arrival-time (circles) and observed arrival times (Vertical lines) using (a) initial istropic model (b) after VTI calibration. After Erwemi et al., 2010.

CHAPTER 8:

MICROSEISM LOCATION UNCERTAINTIES

8.1 Waveforms Picking Error Implications

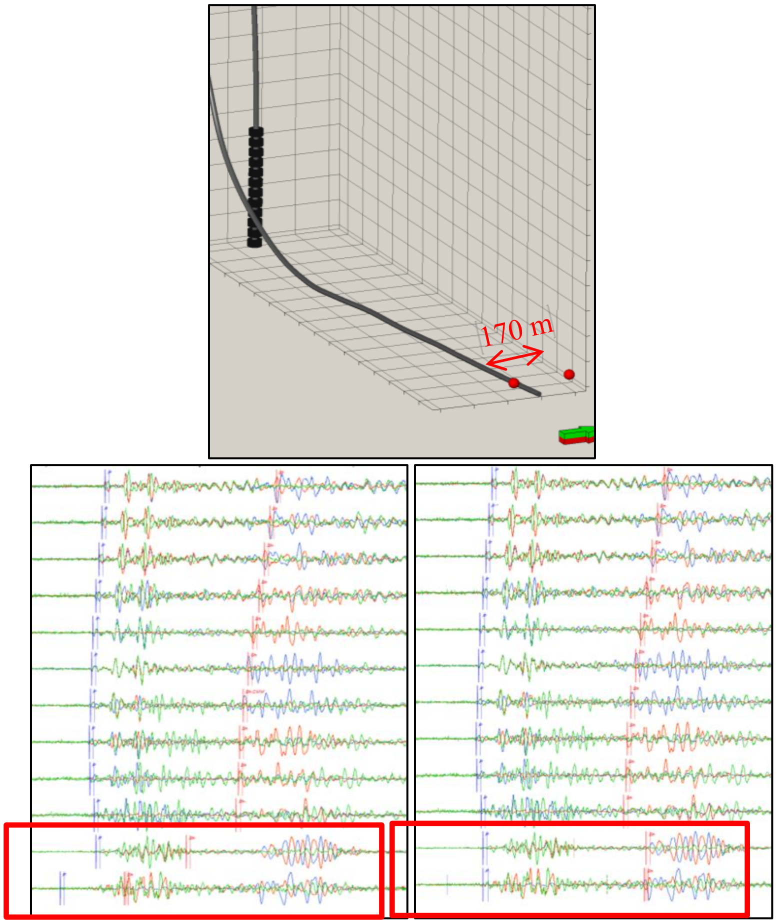

Figure 8-1 : Re-picked P and S for receivers #11 and #12 and relocated the event accordingly.

Waveform picking is a critical for accurate hypocenter location estimation. Figure 8-1 show a waveforms of one of the events on stage 2 located twice prior and post manual waveform pick correction and the associated implications on hypocenter location. The associated offset was over 170m in microseism location. Microseism location are sensitive to picking errors, however, it’s a manageable source of error with careful manual review and repacking of waveforms.

8.2 Geometry Uncertainity Analysis

Microseismic monitoring for hydraulic fracturing operation, often, utilizes a single observation well, in which case seismic polarization analysis is used to help constrain the source location estimation. Uncertainties in the arrival times and polarization analysis lead to a location uncertainty ellipsoid, defining how predicted uncertainties vary with direction. In this section, I investigated event location uncertainties for various source/ receiver configurations. I modeled three different monitoring configurations and estimated the associated errors on hypocenter locations. I made the assumption that the errors or uncertainties follow a normal distribution characterized by a certain standard deviation (σ). Thus, from a statistical population point of view there is a 68% probability of the location falling in particular direction within one (σ) either side of the hypocenter of 95% probability for it falling within two (σ), defining a Gaussian probability density function (PDF). Nevertheless, the simplified location errors assumed here serve to illustrate several issue related to defining the underlying fracture geometry that results in a diffuse cloud of microseismic locations. PDF and half-axis have been calculated for each morning configuration setting (refer to figures 8-2, 8-3, 8-4, 8-5). Results have shown that vertical monitoring setting is the optimal setting with the least geometry introduces uncertainties. Vertical monitoring has shown a superior control on the vertical component with the least uncertainties; however, horizontal monitoring has a very good control on the horizontal components. Also, the analysis has shown that our subject dataset have a large margin of errors introduces by geometry.

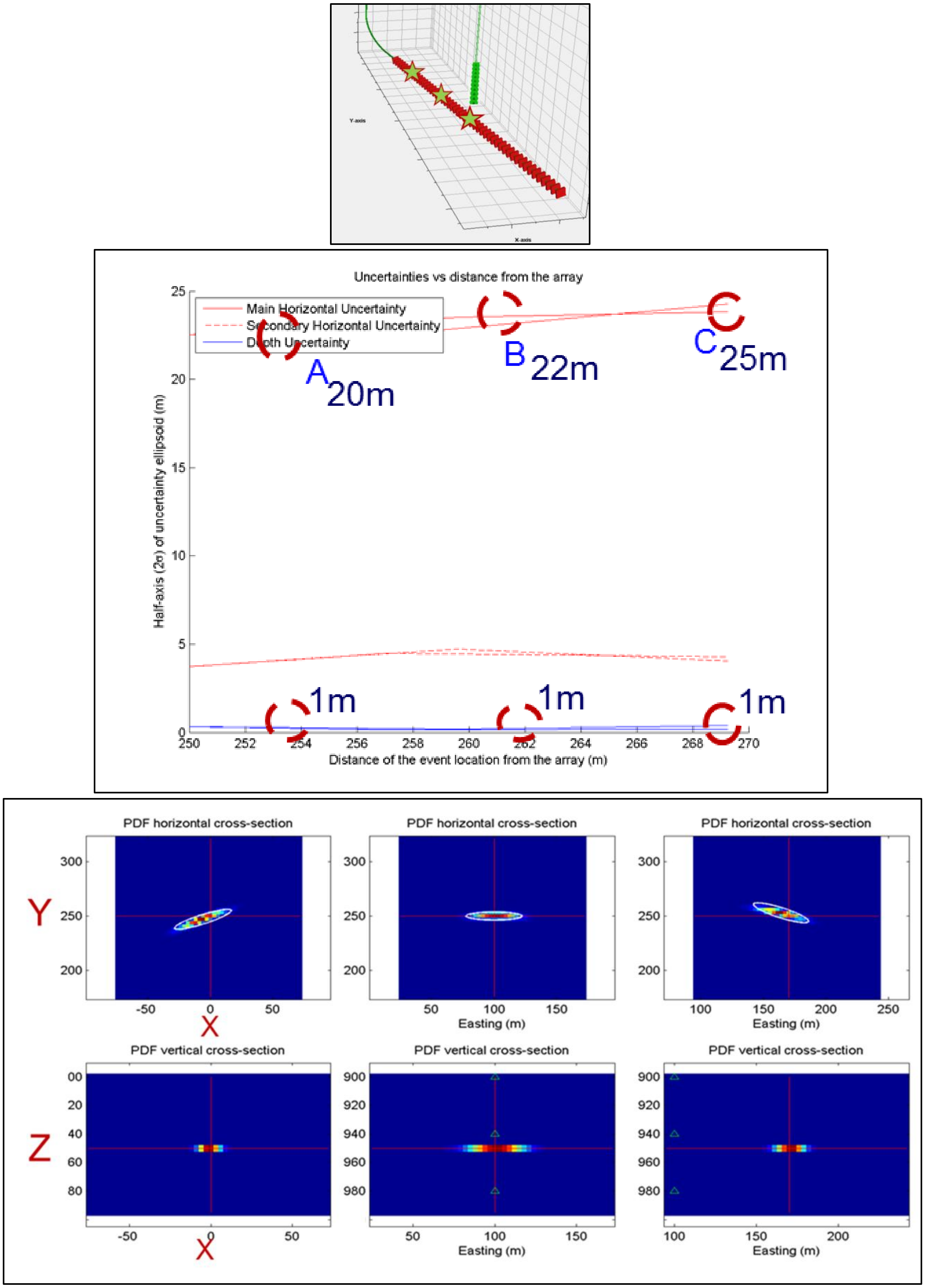

Figure 8-2: A vertical monitoring setting with a well placed at close proximity to the stimulation stages. For optimal monitoring, same numbers of sensors are deployed above and below the target zone. Cross plot above indicate a superior control on the vertical components on the vertical monitoring setting.

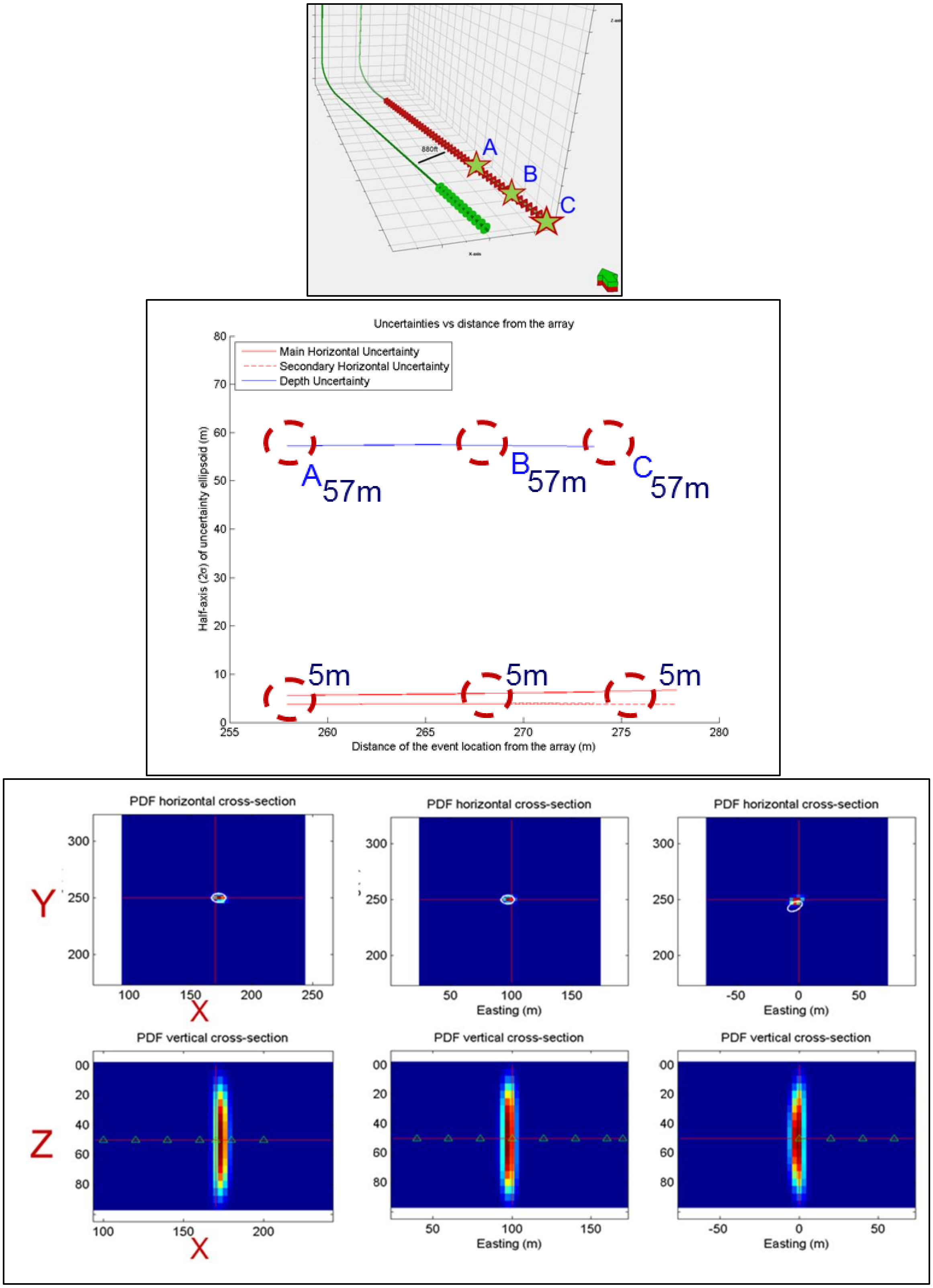

Figure 8-3: A horizontal monitoring setting with a borehole positioned horizontally at close proximity to the stimulation stages. For optimal monitoring, the array is deployed parallel to the stimulation stages. Cross plot above indicate a very good control on the horizontal components on the horizontal monitoring setting.

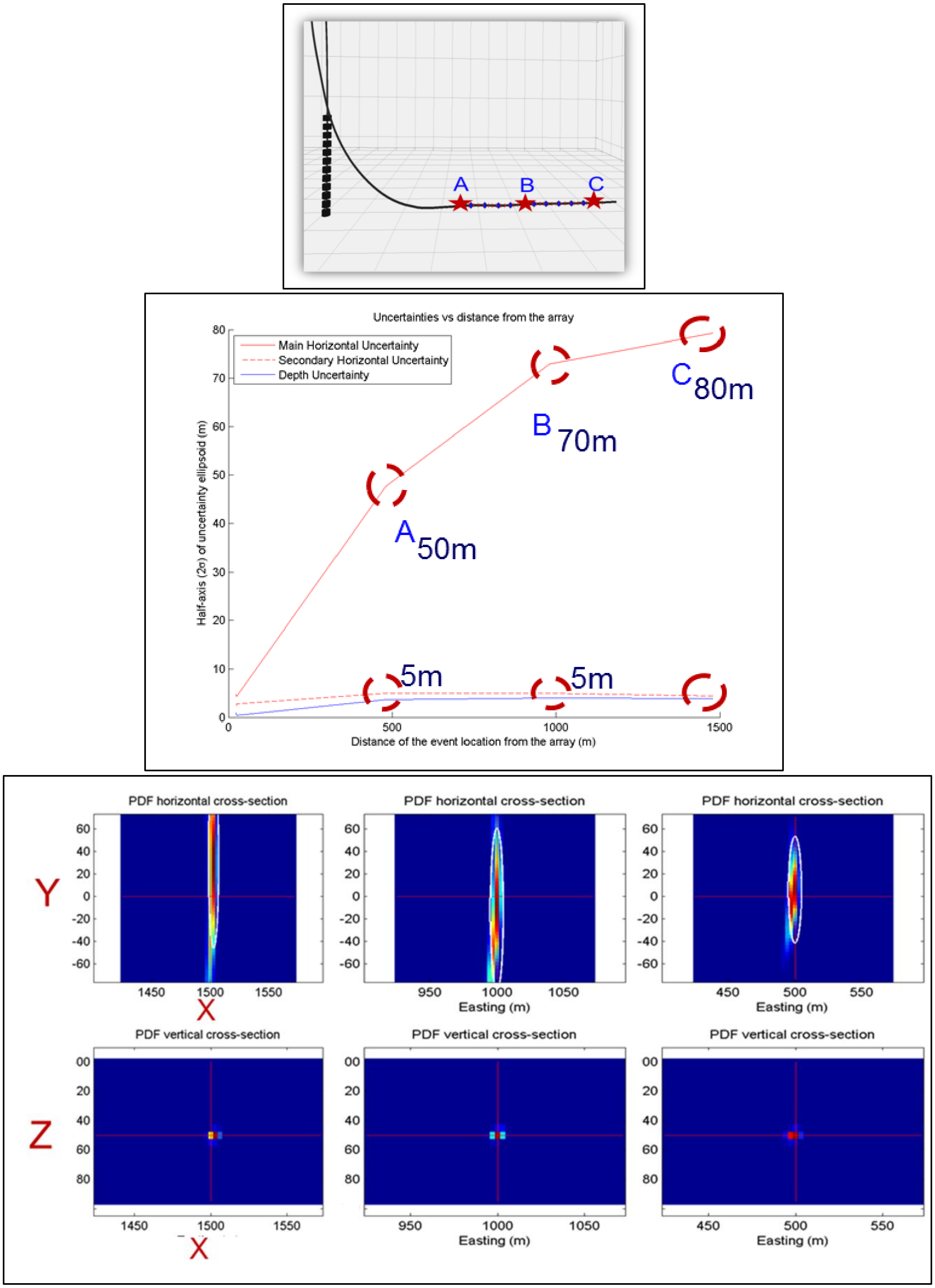

Figure 8-4: A monitoring setting mimicking our subject dataset experiment, the monitoring borehole right behind the heel of the stimulated well. Events from stages 12, 6, and 1 were modeled in this geometry configuration introduced error. Cross plot indicates a fairly good control on the vertical component but no so much on the horizontal components.

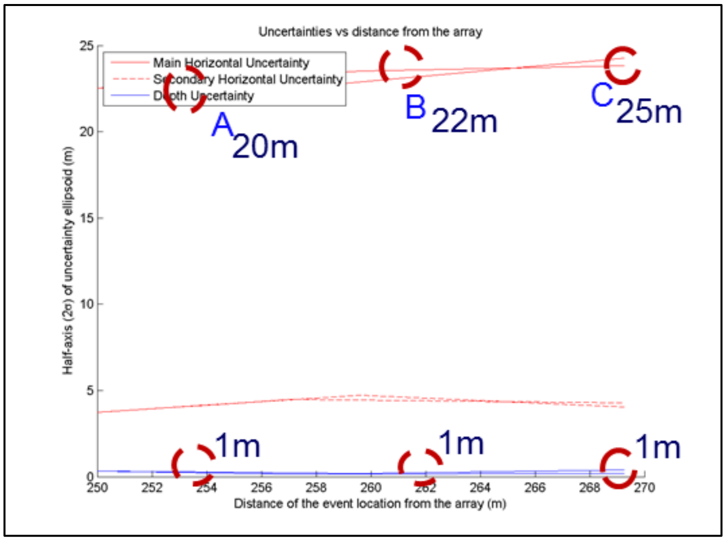
Uncertainties vs distance from the array
Main Horizontal Uncertainty
Secondary Horizontal Uncertainty
Depth Uncertainty
Half-axis (2σ) of uncertainty ellipsoid (m)
Distance of the event location from the array (m)
25
20
15
10
5
0
250
252
254
256
258
260
262
264
266
268
270
A 20m
B 22m
C 25m
1m
1m
1m

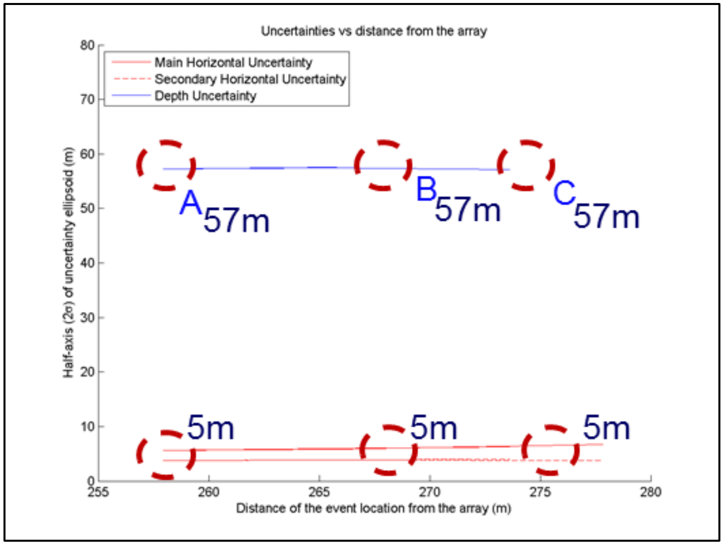
Uncertainties vs distance from the array
Main Horizontal Uncertainty
Secondary Horizontal Uncertainty
Depth Uncertainty
Half-axis (2σ) of uncertainty ellipsoid (m)
Distance of the event location from the array (m)
80
70
60
50
40
30
20
10
0
255
260
265
270
275
280
A 57m
B 57m
C 57m
5m
5m
5m

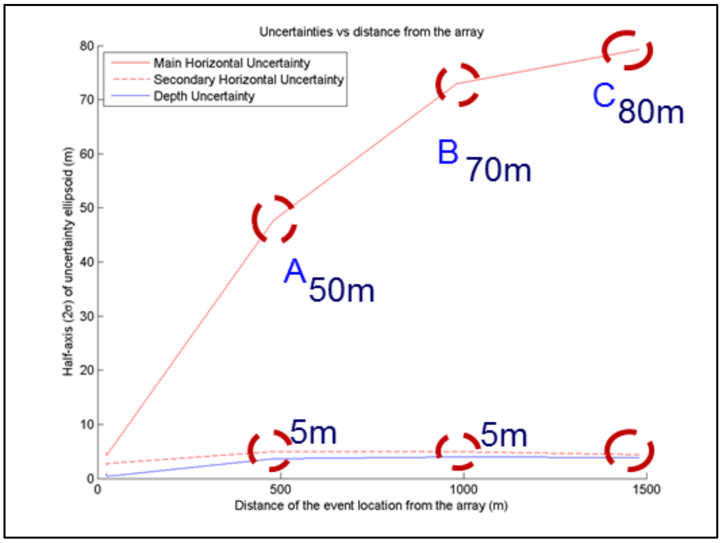
Uncertainties vs distance from the array
Main Horizontal Uncertainty
Secondary Horizontal Uncertainty
Depth Uncertainty
Half-axis (2σ) of uncertainty ellipsoid (m)
Distance of the event location from the array (m)
80
70
60
50
40
30
20
10
0
0
500
1000
1500
A 50m
B 70m
C 80m
5m
5m

8.3 Hypocenter Sesntivity to Velocity Uncertainity

The velocity model is a critical element of microseismic image processing: even if all components are optimum, an inaccurate velocity model can lead to few hundred feet off in hypocenters locations. In many cases, it is initially derived from dipole sonic logs, where a high-resolution primary (P) and shear (S) wave can be calculated. However, these velocities are not ideal for microseismic processing, as they are vertical velocities along the wellbore at time of drilling. The monitor well could be no competent, drilling mud invasion could have been occurred, and several other disturbing factors exist. The correct horizontal velocities tend to be different relative the log derived velocities. In this section, two perturbed velocity models were constructed out of the calibrated velocity model (see section 6.5) to estimate velocity model uncertainty effects on microseism location accuracy. On the first model, P-wave velocities were increased by a 5% and S-wave velocities were decreased by 5%, and on the 2nd model, P remained unchanged and S was increased by 10%. (Figure 8-2)

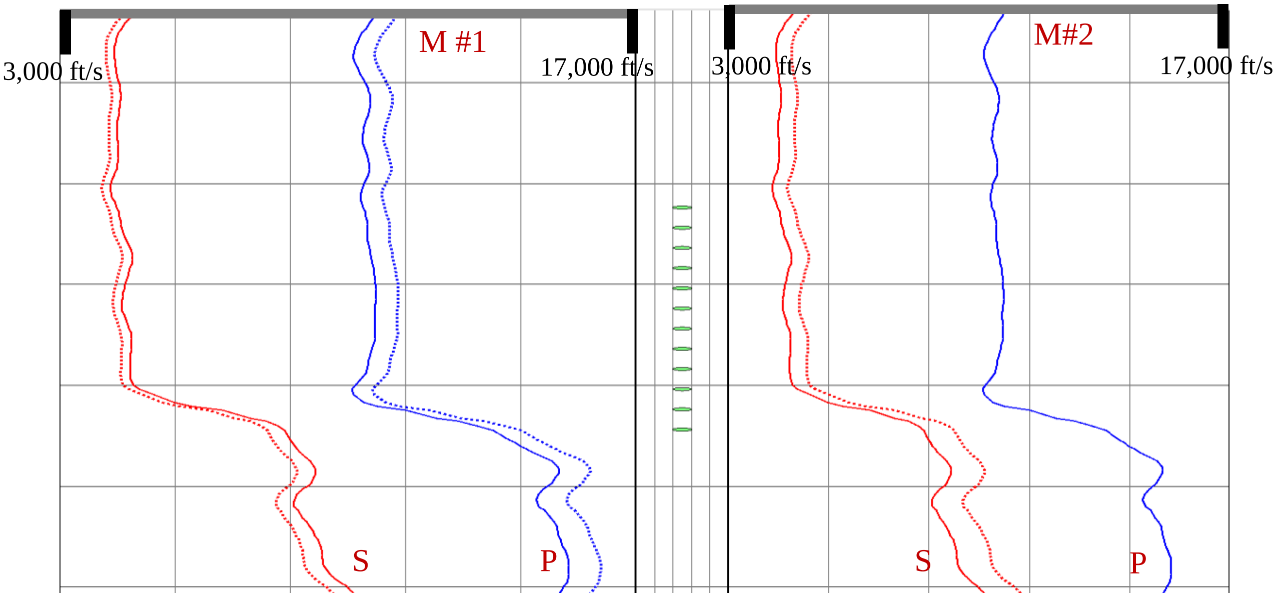

Figure 8-5: The two perturbed velocity models a) M#1 where P was increased by 5% and S was decreased by 5% b) M#2 where P remained unchanged and S was increased by 10%. Dashed lines denote the perturbed velocities.

Accounting for velocity related uncertainties is key factor in microseismic processing; and understanding of P-wave and S-wave velocities uncertainty effects on hypocenter locations calculation is critical. Equation 7-1 describes the distance from the source to the monitoring well a simple isotropic velocity model.

$$D = \frac{V_P V_S \times (T_S - T_P)}{V_P - V_S}$$

Equation 8-1

Stage 9 and 8 events of our subject experiment were relocated based on the two new perturbed velocity models (Model #1, and Model #2) using Geiger method for hypocenter relocation. Figure 8-3 shows the different clouds of events and the associated offset relative to the calibrated events. Model #1, which has 5% increase of P-wave velocities and 5% decrease of S-wave velocities, shifted the hypocenters closer to the monitoring well, whereas model #2, which has no change on P-wave velocities and increase of 10% of S-wave velocities, shifted the cloud of events further away from the monitoring borehole. Considering equation 8-1, the distance between monitoring array and events hypocenter has an inverse relationship to (Vp/Vs) ratio. As a result, model #1 which has a higher Vp/Vs ratio would locate the hypocenter closer to monitoring borehole, and vice versa applies to Model#2.

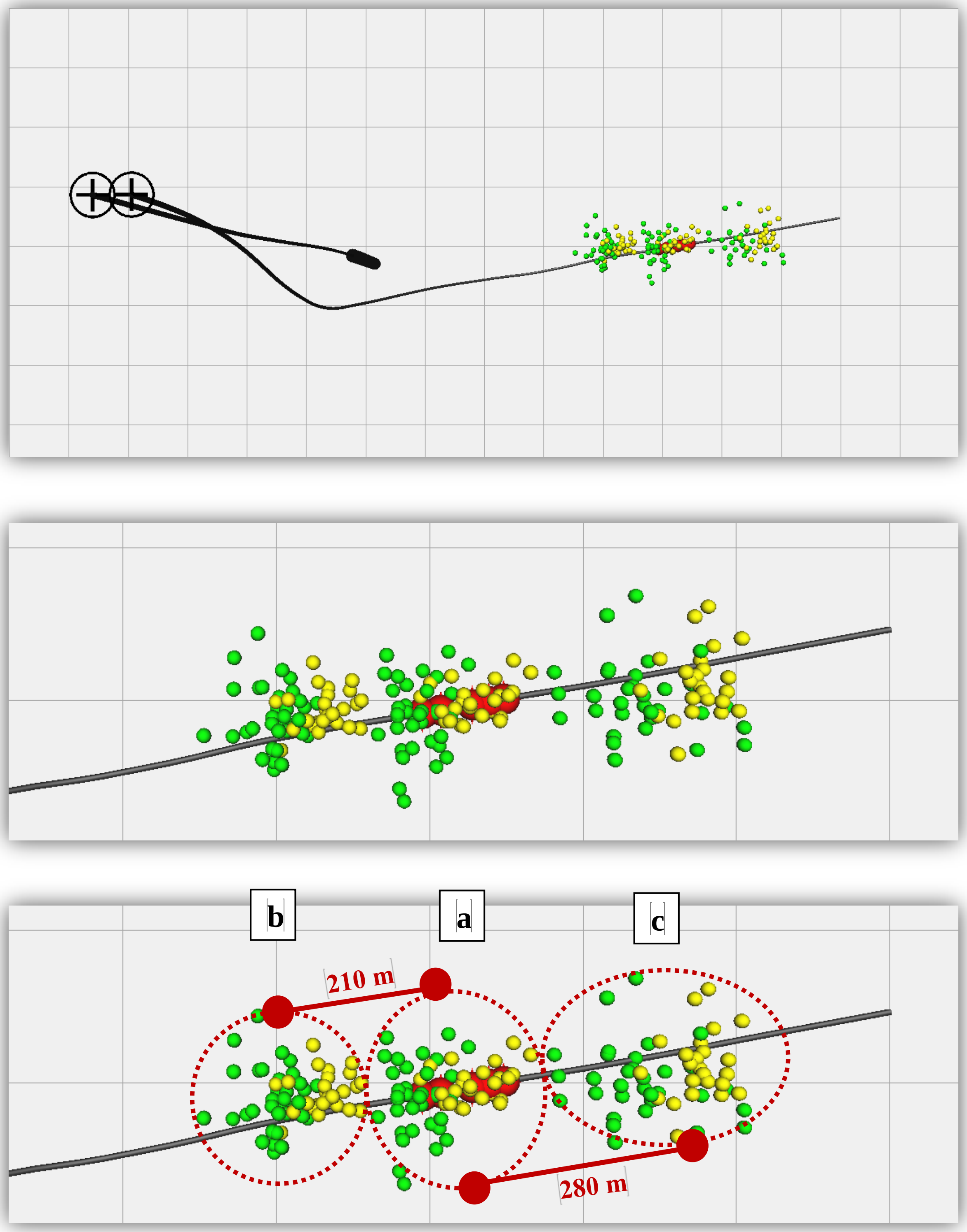

Figure 8-6: Relocation of observed events on stages 9 (green dots) and 8 (yellow dots) based on three different velocity models, a) events hypocenters based on the original calibrated velocity model b) events hypocenters based on perturbed model #1, c) events hypocenters based on perturbed model #2.

8.4 Velocity Structure Complexity Analysis

The greater the velocity structure complexity the higher the microseism associated uncertainty ellipsoid and associated error margins. Figure 8-4 shows the velocity structure of our target zone. Figures 8-5 to 8-10 shows the modeled ray paths for synthetic events at different depths according to a simplistic synthetic velocity structure in comparison to our current existing complex velocity structure. Clearly, events that occur right below the target zone would tend to have much more complex ray paths compare to shallower events. The complexity is due to the relatively sudden and rapid change in velocity structure going from Shale, hot shale, to Sandstones strata. This complexity is introducing a greater error margin for locating events that occur right below or into the target zone, amplified by the existing non-optimal geometry.

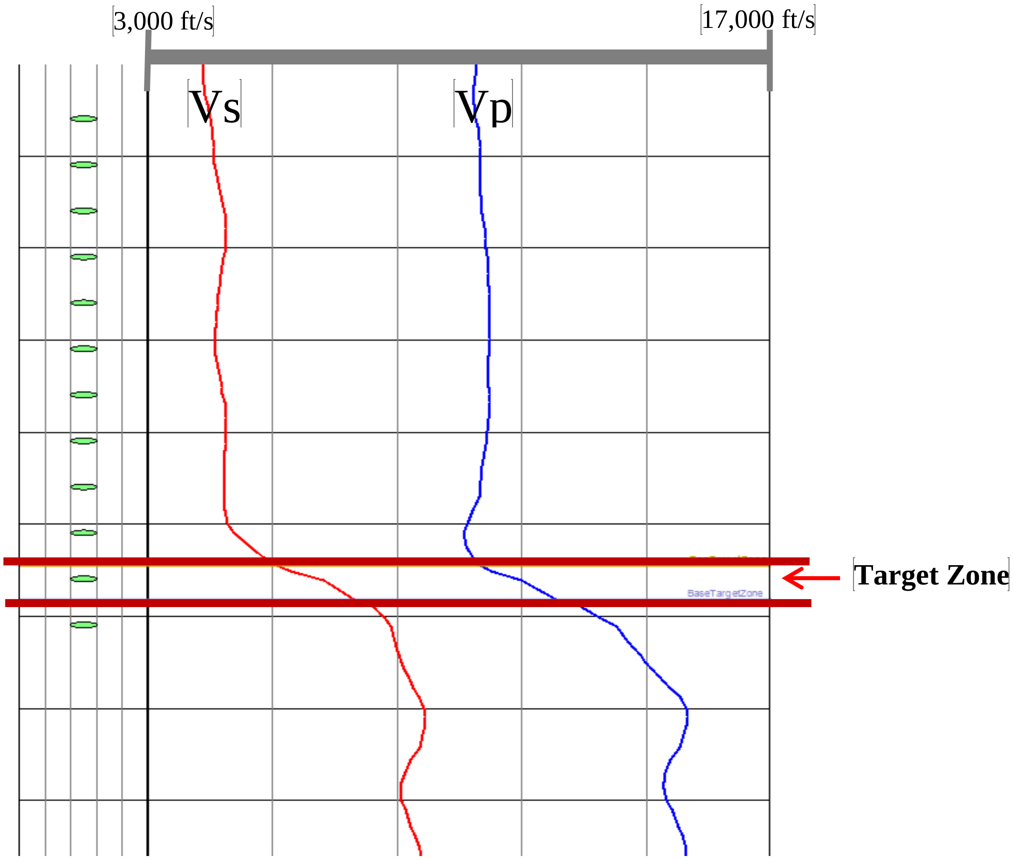

Figure 8-7: A well section of Vs and Vp logs of the subject monitoring well.

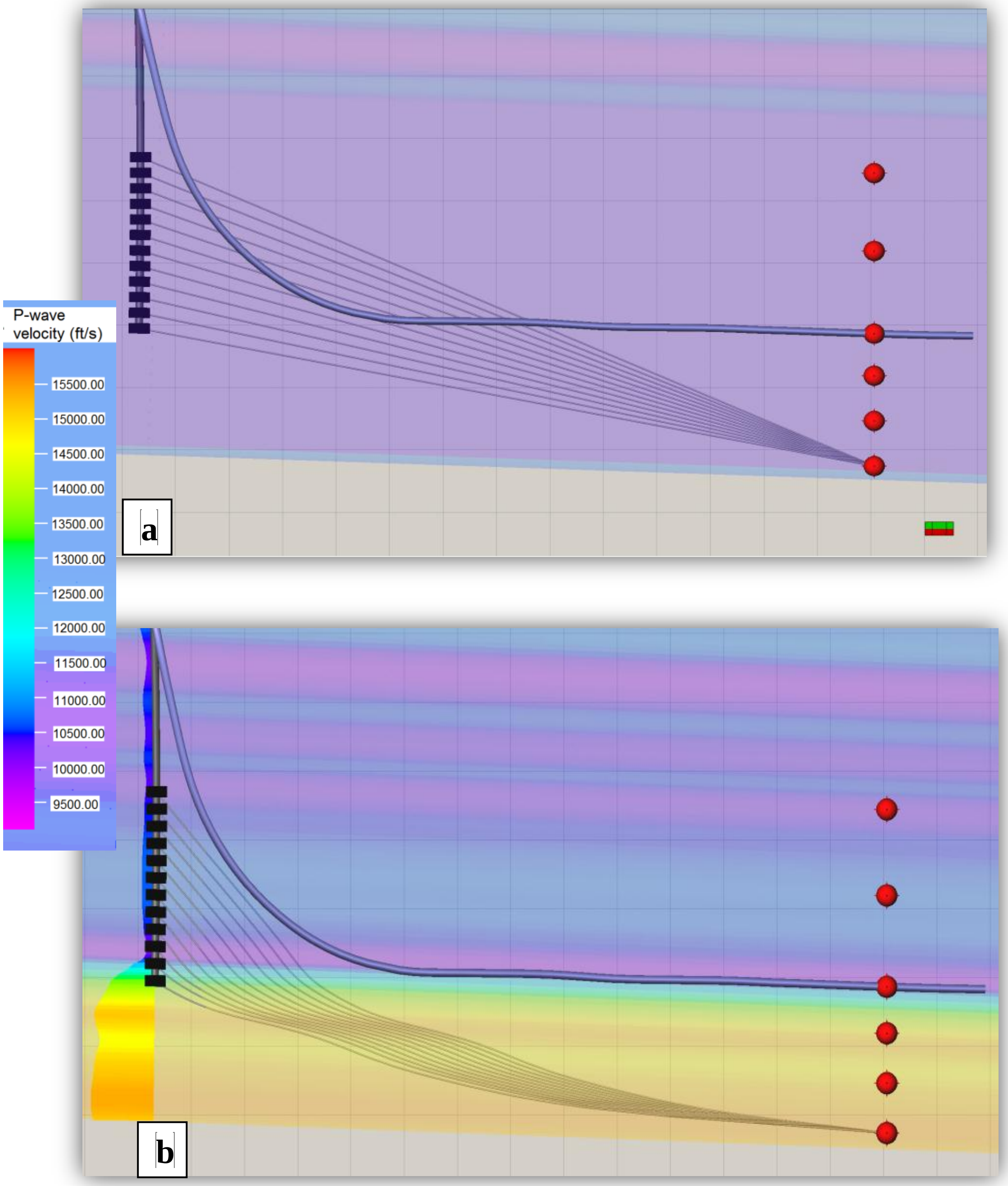

Figure 8-8: The modeled ray paths for synthetic events (deeper than target zone) according to a) a simplistic synthetic velocity structure in comparison to our current existing b) complex velocity structure. Colored background reflects the P-wave velocity model.

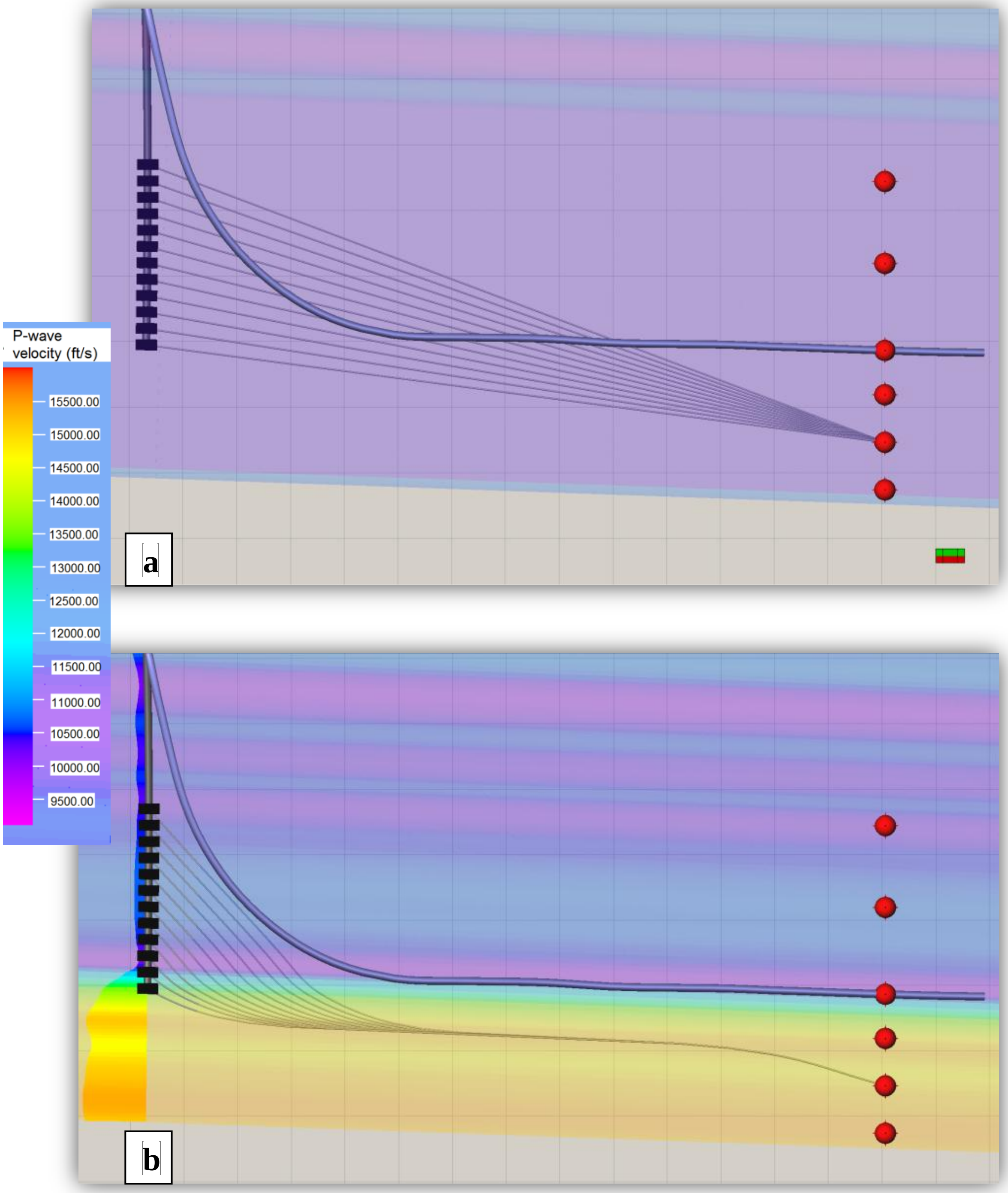

Figure 8-9: The modeled ray paths for synthetic events (deeper than target zone) according to a) a simplistic synthetic velocity structure in comparison to our current existing b) complex velocity structure. Colored background reflects the P-wave velocity model.

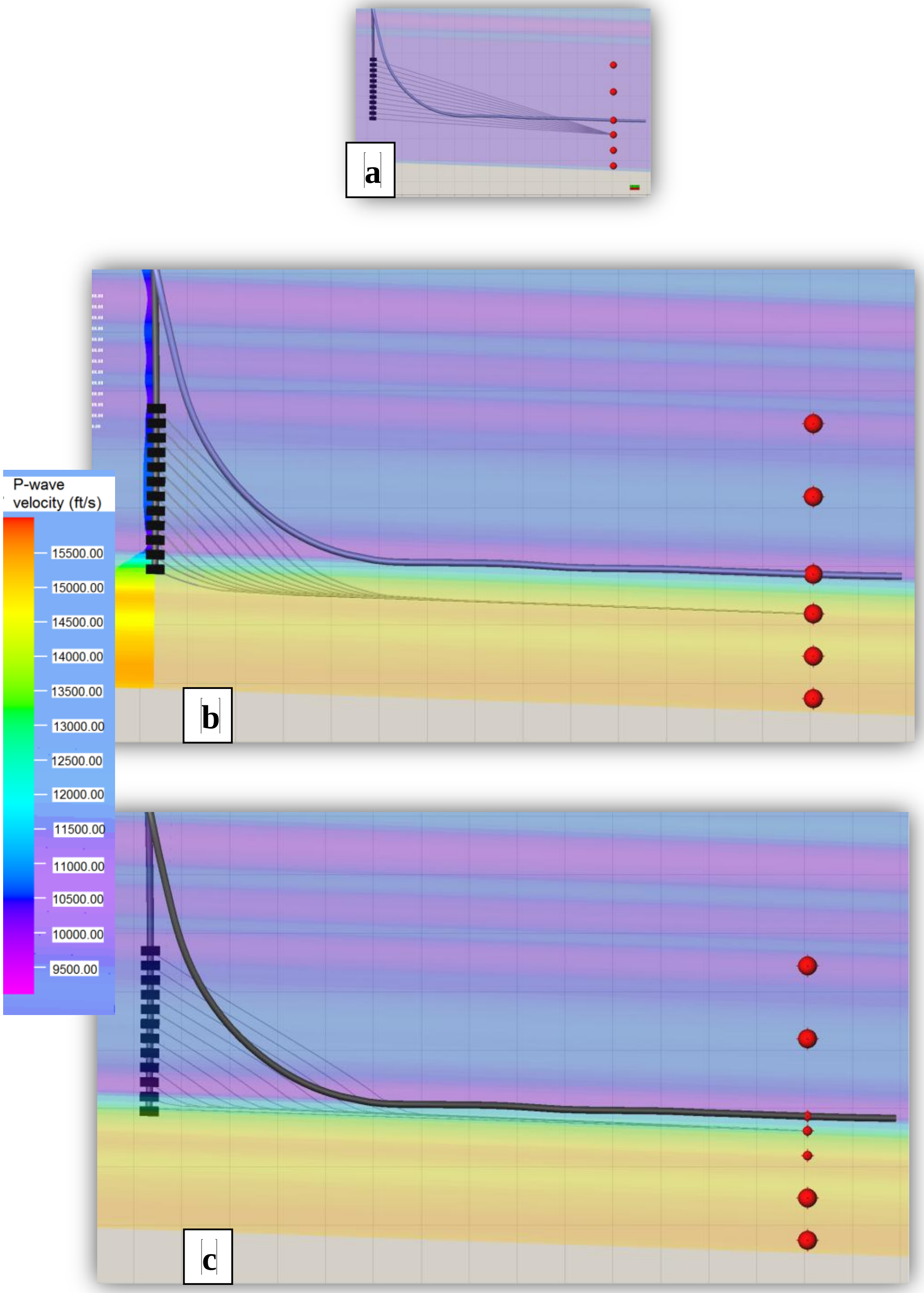

Figure 8-10: The modeled ray paths for synthetic events (below target zone) according to a) a simplistic synthetic velocity structure in comparison to our current existing b) complex velocity structure. Colored background reflects the P-wave velocity model. c) An additional events right below the target level.

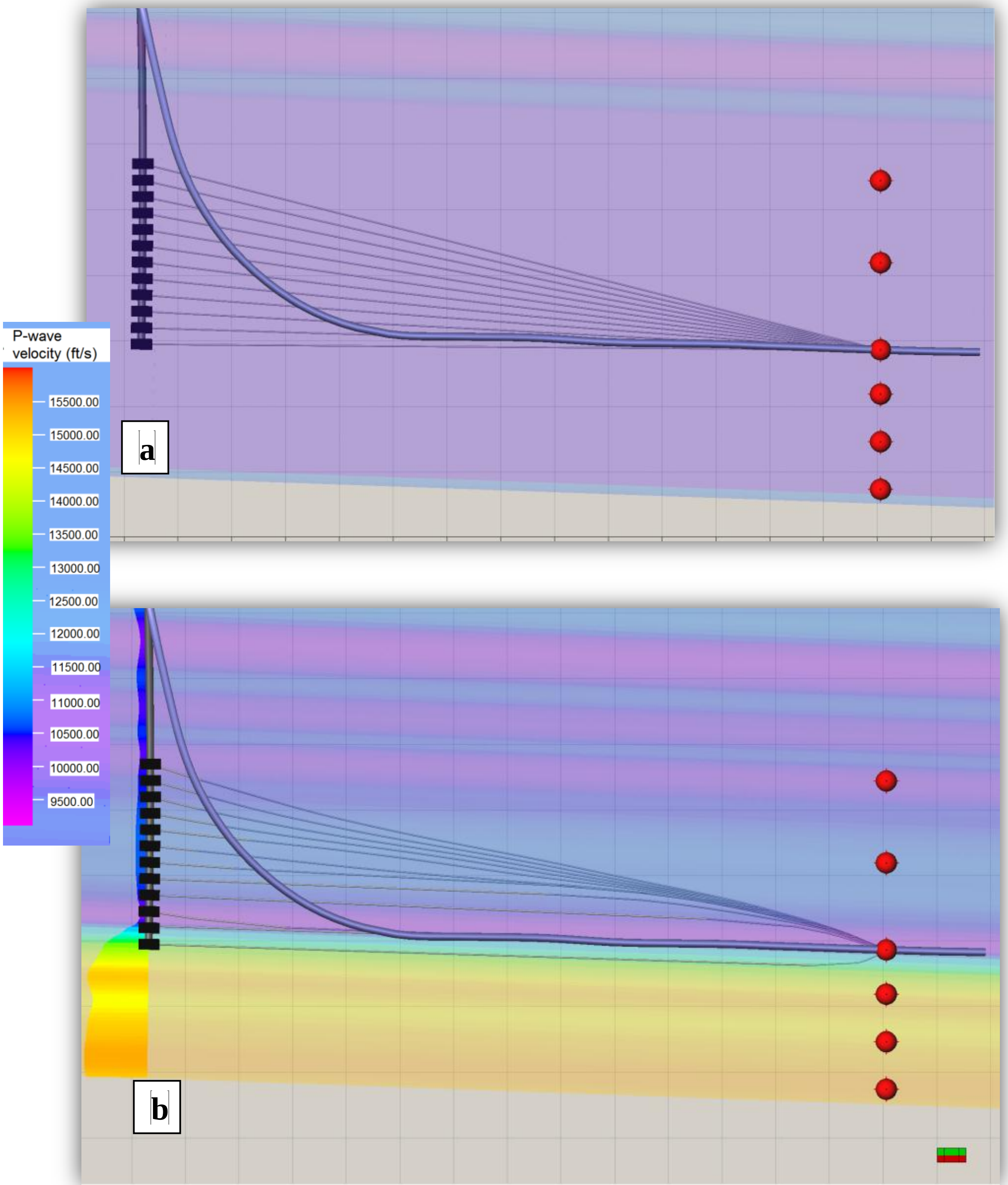

Figure 8-11: The modeled ray paths for synthetic events (right at target zone) according to a) a simplistic synthetic velocity structure in comparison to our current existing b) complex velocity structure. Colored background reflects the P-wave velocity model.

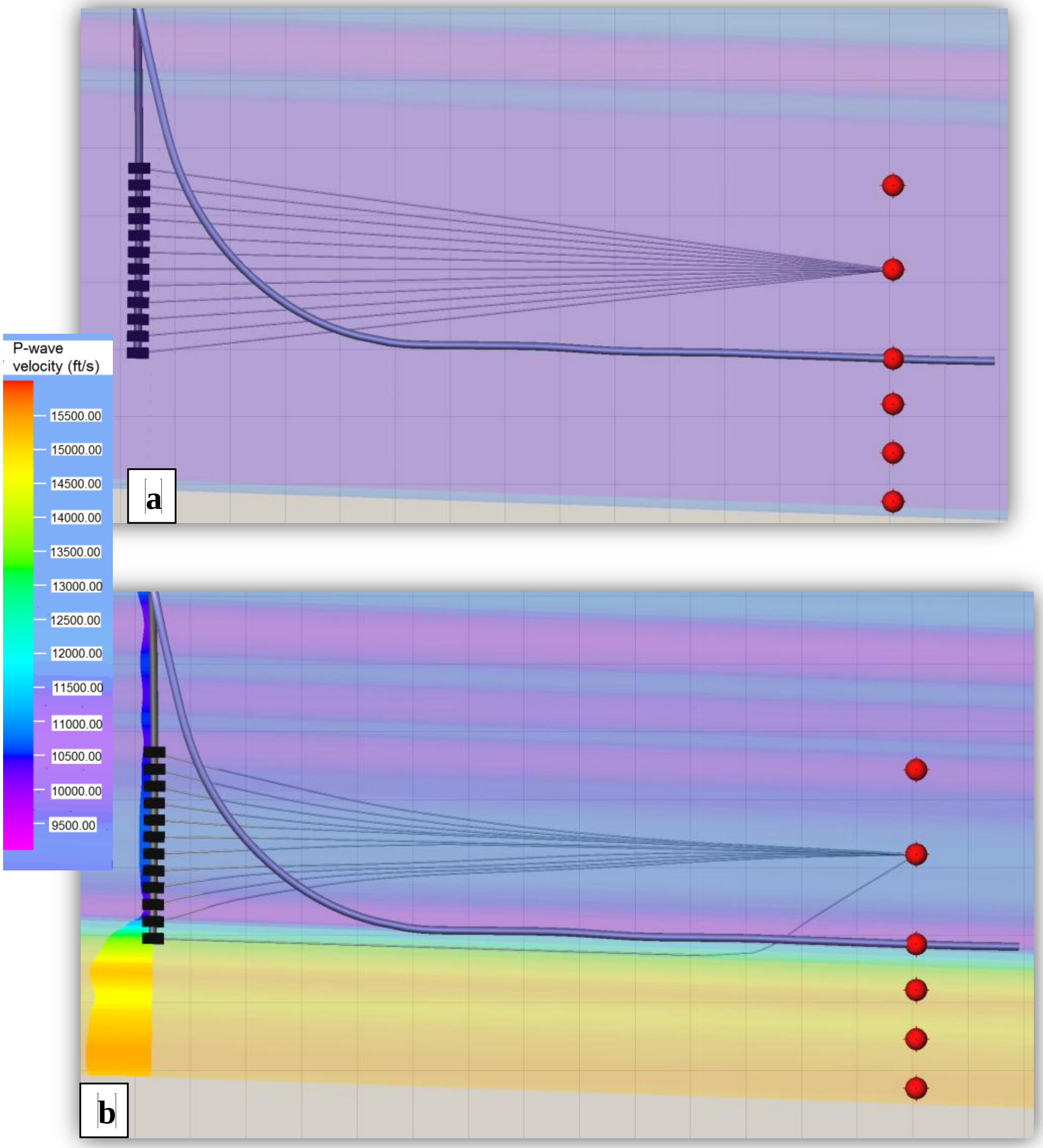

Figure 8-12: The modeled ray paths for synthetic events (shallower than target zone) according to a) a simplistic synthetic velocity structure in comparison to our current existing b) complex velocity structure. Colored background reflects the P-wave velocity model.

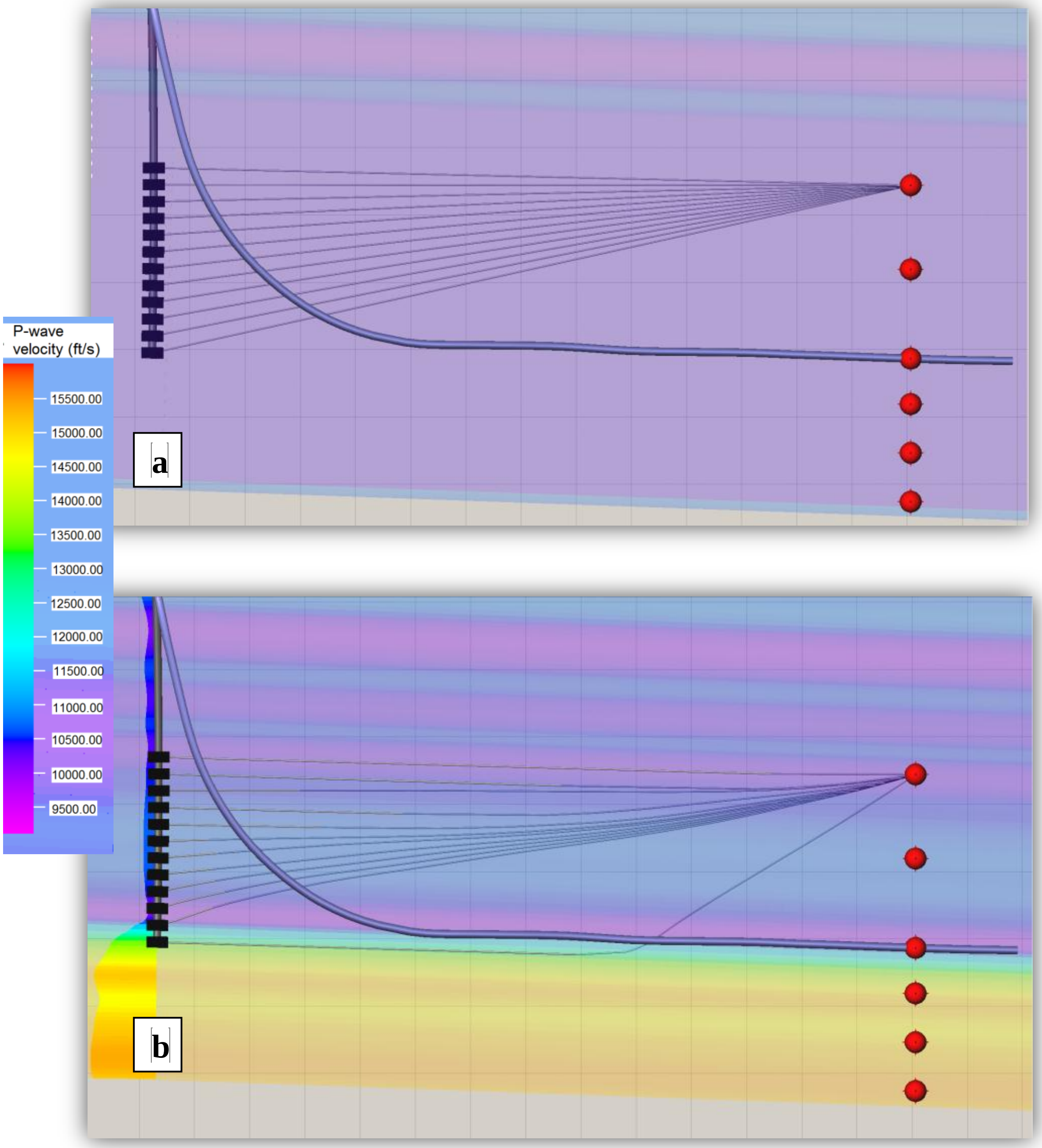

Figure 8-13: The modeled ray paths for synthetic events at (shallower than target zone) according to a) a simplistic synthetic velocity structure in comparison to our current existing b) complex velocity structure. Colored background reflects the P-wave velocity model

CHAPTER 9:

CONCLUSION

9.1 Conclusion Summary

Microseismic event location uncertainty is one of the most critical aspects of microseismic monitoring. MS locations form the basis of simulated rock volume estimation. Velocity model and geometry settings are the main sources of microseismic location uncertainties as shown on chapter 8, as well as waveforms arrivals picking.

Construction of an appropriate velocity model requires extensive data and sufficient details to correctly predict arrival times in order to accurately relocate the source locations. Depending on the lithological details and acoustic characteristics of the reservoir, velocity heterogeneity and anisotropy parameters may need to be incorporated in the processing workflow. Transverse Isotropy velocity model calibration is most suitable solution to correct for anisotropy effects on hypocenter location estimation. Location errors resulting from velocity models highlight the importance of quality control plots of arrival time differences and the need be used to identify systematic apparent velocity errors in the arrival tie move out.

Results have shown that vertical monitoring setting is the optimal setting with the least geometry introduces uncertainties. Vertical monitoring array has minimum error margin on the vertical resolution, whereas, horizontal monitoring has minimized horizontal resolution error. Also, the analysis has shown that our subject dataset have a large margin of errors introduces by geometry. Future work recommendation is to include surface monitoring data.

REFERENCES:

[1] Abu-Ali, M.A., Rudkiewicz, J.L.L., McGillivray, J.G., and Behar, K, 1999, Paleozoic petroleum system of Central Saudi Arabia: GeoArabia, v.4, p. 321-336.

[2] Aqrawi, A.A.M., 1998, Paleozoic stratigraphy and petroleum systems of the western and southwestern deserts of Iraq: GeoArabia, v. 3, p. 229-247.

[3] Ay E., H. Sadi Kuleli, Fuxian Song, M. Nafi Toksöz, 2012. Detection and Enhancement of Microseismic Signals with Correlation Operators: "Cross Product and Master Event" Methods. Expanded Abstracts, 'SEG, Istanbul 2012 International Geophysical Conference And Oil & Gas Exhibition [2]

[4] Beers, R. F., and C. Goodman, 1944, Distribution of radioactivity in ancient sediments: Geological Society of America Bulletin, v. 55, p. 1229–1254.

[5] Bishop, R.S., 1995, Maturation history of the lower Paleozoic of the eastern Arabia Platform, in Al-Husseini, M.I., ed., Geo-94, Middle East Petroleum Geosciences Conference, Gulf PetroLink, Manama, Bahrain, v. l,p. 180-189.

[6] Cipolla, C.L., Williams, M.J., Weng, X, Mack, M., and Maxwell, S., 2010, Hydraulic Fracture Monitoring to Reservoir Simulation: Maximizing Value, SPE133877

[7] Cole, G.A., Abu-Ali. M.A., Aoudeh, S.M., Carrigan, M.J., Chen, H.H., Colling, E.L., Gwathney, W.J., Al-Hajii, A.A., Halpern, H.I., Jones, P.J., Al-Sharidi. S.H.. and Tobey, M.H., 1994. Organic geochemistry of the Paleozoic petroleum system of Saudi Arabia: Energy and Fuels, v. 8, p. 1425-1442.

[8] Crampin, S., 1989, Suggestions for a consistent terminology for seismic anisotropy, Geophysical Prospecting, 37, 753-770.

[9] Daley, P. F. and F. Hron, 1977, Reflection and transmission coefficients for Transversely isotropic media, Bull. Seis. Soc. Am., 67, 661-675.

[10] DeMeersman, K., J.M. Kendall, and M. van der Baan, 2009, The 1998 Valhall microseismic data set: An integrated study of relocated sources, seismic multiples, and S-wave splitting: Geophysics, 74, no. 5, B183–B195.

[11] Dyer, B. C., R. H. Jones, J. F. Cowles, O. Barkved, and P. G. Folstad, 1999, Microseismic survey of aNorth Sea reservoir:World Oil, March, 74–78.

[12] Economides, M.J., Nolte, K.G., 2000. Reservoir Stimulation 3rd ed Wiley and Sons Ltd., United Kingdom.

[13] Eisner L., Heigl W., Duncan P. and Keller W. 2009. Uncertainties in passive seismic monitoring. The Leading Edge 28, 648–655

[14] Eisner, L. (2013). “Microseismic monitoring in oil or gas reservoir. SEG Continuing Education Course.

[15] Evans, D.M. [1966] The Denver Area Earthquakes and the Rocky Mountain Arsenal Disposal Well. The Mountain Geologist, 3 (1), 23–36.

[16] Evans, D.S., Bahabri, B.H., and Al-Otaibi, A.M., 1997, Stratigraphic trap in the Permian Unayzah Formation, central Saudi Arabia: GeoArabia, v.2, p. 257-278.

[17] Evans, D.S., Bahabri, B.H., and Al-Otaibi, A.M., 1997, Stratigraphic trap in the Permian Unayzah Formation, central Saudi Arabia: GeoArabia, v.2, p. 257-278.

[18] Faqira, M., M. Rademakers, A. M. Afifi (2000) New insights into the Hercynian Orogeny, and their implications for the Paleozoic Hydrocarbon System in the Arabian Plate, Geoarabia, 14, 199–228.

[19] Fuxian Song, H. Sadi Kuleli, M. Nafi Toksoz, Erkan Ay, and Haijiang Zhang, An improved method for hydrofracture-induced microseismic event detection and phase picking, Geophysics, Volume 75, Issue 6, 2010.

[20] Gane, P.G., Hales, A.L. and Oliver, A.A., 1946 A seismic investigation of the Witwatersrand Earth Tremors. Bull. Seism. Soc. Am., vol. 36, p. 49-80

[21] Geiger, L. “Probability method for the determination of earthquake epicenters from the arrival time only (translated from Geiger's 1910 German article),” *Bulletin of St. Louis University*, vol. 8, no. 1, pp. 56–71, 1912.

[22] Green, A., Robert D. Barree, B. &., & and Jennifer L. Miskimins, C. S. (2007). Development of a Methodology for Hydraulic Fracturing Models in Tight, Massively Stacked, Lenticular Reservoirs. SPE Hydraulic Fracturing Technology Conference.

[23] Gibowicz. S.J. and A. Kijko, 1994, An introduction to Mining Seismology, Academic Press San Diego.

[24] Grechka, V., 2009, Applications of seismic anisotropy in the oil and gas industry, EAGE Publications bv.

[25] Green C.A., Barree R.D. and Miskimins J.L., SPE 106270-PA “Hydraulic Fracture Model Sensitivity Analyses of a Massively Stacked, Lenticular, Tight Gas Reservoir” (2007)

[26] Healy, J.H., Warren, D.H., 1969. Explosion seismic studies in North America. In: Hart, P.J. (Ed.), the Earth's Crust and Upper Mantle: Am. Geophysics.

[27] Higgins, S., S. Goodwin, Q. Donald, A. Donald, T. Bratton, and G. Tracy, 2008, Anisotropic stress models improve completion design in the Baxter shale: SPE Annual Technical Conference and Exhibition, 21-24 September 2008, Denver, Colorado, SPE 115736-MS, 10 p. doi:10.2118/115736-MS

[28] John A. Quirein, J. G. (2006). MICROSEISMIC FRACTURE MONITORING. Society of Petrophysicists & Well Log Analysts - SPWLA-2006-VV.

[29] Jones, P.J., and Stump, T.E., 1999, Depositional and tectonic setting of the Lower Silurian hydrocarbon source facies, central Saudi Arabia: American Association of Petroleum Geologists Bulletin, v. 83, p.314-332.

[30] Kendall, M., S. Maxwell, G. Foulger, L. Eisner, and Z. Lawrence, 2011, Microseismicity: Beyond dots in a box Introduction: Geophysics, 76, WC1–WC3.

[31] King, A. and Talebi, S. 2007. Anistropy Effects on Microseismic Event Location. Pure and Applied Geophysics, 164:2141.

[32] Konert, G., Afifi, A., Al-Hajri, S.A, and Droste, H.J., 2001, Paleozoic stratigraphy and hydrocarbon habitat of the Arabian Plate: GeoArabia. v. 6.p. 407-441.

[33] Lee, W. H. K., and D. A. Dodge, (Editors), (1992). “A Course on: PC-Based Seismic Networks", U.S. Geol. Surv. Open-file Report 92 -441, 535 pp.

[34] Lomax, A., Virieux, J., Volant, P., and Berge, C., 2000, Probabilistic earthquake location in 3D and layered models: Introduction of a Metropolis-Gibbs method and comparison with linear locations, in Advances in Seismic Event Location, Thurber, C.H., and N. Rabinowitz (eds.), Kluwer, Amsterdam, 101-134

[35] M.K. Fisher, S. C., & A.K. Goodwin, S. E. (2005). Integrating Fracture-Mapping Technologies To Improve Stimulations in the Barnett Shale . SPE-77441-PA.

[36] Mahmoud, M.D., Vaslet, D., and Al-Husseini, M.I., 1992, The Lower Silurian Qalibah Formation of Saudi Arabia-an important hydrocarbon source rock: American Association of Petroleum Geologists Bulletin, v. 76, p. 1491-1506.

[37] Mandel, B. M. (2000). Acoustic method of connecting boreholes for multilateral completion. US PATENT 6,026,913.

[38] Maxwell, S. C. (2012). “Statistical evaluation for comparative microseismic interpretation.” 74th EAGE Conference & Exhibition, Extended Abstracts.

[39] Maxwell, S. C., 2010, Microseismic: Growth born from success: The Leading Edge, 29, 338–343

[40] Maxwell, S. C., and T. Urbancic, 2001, The role of passive microseismic monitoring in the instrumented oil field: The Leading Edge, 20, 636–639

[41] Maxwell, S. C., J. Du, and J. Shemeta, 2008, Passive seismic and surface monitoring of geomechanical deformation associated with steam injection: The Leading Edge, 27, 260–266.

[42] Maxwell, S., J. Rutledge, R. Jones, and M. Fehler, 2010, Petroleum reservoir characterization using downhole microseismic monitoring: Geophysics(2010), 75(5):75a129.

[43] Maxwell, S.C., 2012, Comparing microseismic interpretation of hydraulic fractures: SPE 162782, SPE Canadian Unconventional Resources Conference, Calgary, Canada

[44] Maxwell, S.C., What Does Microseismic Tell Us About Hydraulic Fracture Deformation, Recorder, 29-43, October, 2011.

[45] Maxwell, S. (New Orleans, Louisiana, 4-7 October 2009). Assessing the Impact of Microseismic Location Uncertainties On Interpreted Fracture Geometries. SPE Annual Technical Conference and Exhibition, SPE-125121-MS.

[46] Meyr, B. and Nederlof, M.: 1984, identification of source rocks on wireline logs by density/resistivity and sonic transite time/resistivity cross plots, AAPG Bull. V.68, PP. 121-129. Moldowan, J., Seifert, W. and Gallegos, E.1985: Relation between petroleum composition and depositional environment of petroleum source rocks, AAPG Bull. V.69, PP. 1255-1268.

[47] Milner, P.A., 1998, Source rock distribution and thermal maturity in the southern Arabian Peninsula: GeoArabia, v. 3, p. 339-356.

[48] Mizuno, T., Leaney, S. and Michaud, G., 2010, Anisotropic velocity model inversion for imaging the microseismic cloud, EAGE Extended Abstracts.

[49] Mukul M. Sharma, P. B.-A., Richard Sullivan, R. S., & Larry Griffin, L. W. (26-29 September 2004). Slick Water and Hybrid Fracs in the Bossier: Some Lessons Learnt . SPE 89876, SPE Annual Technical Conference and Exhibition, Houston, Texas.

[50] Pei, D., Quirein, J., Cornish, B.E., Quin, D., and Warpinski, N.R. 2009. Velocity Calibration for Microseismic Monitoring: a Very Fast Simulated Annealing Approach. Paper presented at the CPS/SEG Beijing International Geophysical Conference, Beijing, China, 24-27 April.

[51] Phillips,W. S., J. T. Rutledge, L. H. House, and M. C. Fehler, 2002, Induced microearthquake patterns in hydrocarbon and geothermal reservoirs: Six case studies: Pure andApplied Geophysics, 159, no. 1, 345–369.

[52] Phinney, R.A. and S. W. Smith, 1963. Processing of Seismic Data from an Automatic Digital Recorder. Bulletin of the Seismological Society of America 53 (3): 549–562.

[53] Pistre, V., Kinoshita, T., Endo, T., Schilling, K., Pabon, J., Sinha, B., Plona, T., Ikegami, T., Johnson, D., 2005, A modular wireline sonic tool for measurements of 3D (azimuthal, radial, and axial) formation acoustic properties: paper presented at the 46th SPWLA Symposium.

[54] Rich, J.P. and Ammerman, M. 2010. Unconventional Geophysics for Unconventional Plays. SPE 131779.

[55] Riding, J. B. and Rochelle, C. A. (2009). "Subsurface characterisation and geological monitoring of the co2 injection operation at weyburn, saskatchewan, canada." Geological Society Special Publications, 313, 227–256.

[56] Sayers, C.M., 2005, Seismic anisotropy of shales: Geophysics, v. 64, p. 93-98.

[57] Sharland, PR., Casey, D.M., Davies, R.B., Hall, S.H., Heward. A.P., Horbury, A.D., Simmons, M.D., 2001, Arabian plate sequence stratigraphy: GeoArabia Special Publication 2, Gulf PetroLink. Manama, Bahrain, 371 p.U.S. Geological Survey World Energy Assessment Team. 2000, U.S. Geological Survey World Petroleum Assessment 2000-Description and results: U.S. Geological Survey Digital Data Series 60, 4 CD-ROMs.

[58] Shimshoni, S. and S. W. Smith, 1964. Seismic Signal Enhancement with Three-Component Detectors. Geophysics 29 (5): 664–671.

[59] Song F., H. S. Kuleli, M. N Toksöz, E. Ay and H. Zhang . 2010. An improved method for hydrofracture-induced microseismic event detection and phase picking. Geophysics 75, A47–A52.

[60] Stein, S. a. (2003). An Introduction to Seismology, Earthquakes, and Earth Structure. Malden, MA, USA: Blackwell Publishing Ltd.

[61] Thomsen, L, 1986, Weak elastic anisotropy, Geophysics, 51 (10), 1954-1966.

[62] Toda, S., and R. Stein., 2003, Toggling of seismicity by the 1997 Kagoshima earthquake couplet: A demonstration of time dependent stress transfer, J. Geophysics. Res., 108(B12), 2567, doi:10.1029/2003JB002527.

[63] Trnkoczy, A., 1998. Guidelines for civil engineering works at remote seismic stations. Application Note 42, Kinemetrics Inc., 222 Vista Av., Pasadena, Ca. 91107

[64] Urbancic, T. I., Shumila, V., Rutledge, J. T. and Zinno, R. J., 1999. Determining hydraulic fracture behavior using microseismicity: Vail Rocks 1999, The 37th U.S. Symposium on Rock Mechanics (USRMS), 99-0991.

[65] Verdon, JP, Kendall, J-M and Wüstefeld, A (2009) Imaging fractures and sedimentary fabrics using shear wave splitting measurements made on passive seismic data, Geophysical Journal International, 179(2), 1245-1254.

[66] Vesnaver A., and Urpi L. (2013), Full three-dimensional relocation and tomographic inversion of the 1977-2008 earthquakes in north-eastern Italy: a feasibility study. Annals of Geophysics 56, 1, R0110, doi:10.4401/ag-5760.

[67] Vesnaver, A. L. (1996), Ray tracing based on Fermat's principle in irregular grids. Geophysical Prospecting, 44: 741–760. doi: 10.1111/j.1365-2478.1996.tb00172.x

[68] Vesnaver, A., L. Lovisa, and G. Böhm (2008), Full 3D relocation of microseisms for reservoir monitoring. Expanded Abstracts, 78th SEG Annual Meeting, Las Vegas, PSC P1.6.

[69] Vesnaver, A., L. Lovisa, and G. Böhm (2010), Joint 3D processing of active and passive seismic data. Geophysical Prospecting 58, 831-844.

[70] Walsh, J., Sinha, B., Plona, T., Miller, D., Bentley, D. and Ammerman, M., 2007. Derivation of anisotropy parameters in a shale using borehole sonic data. SEG Annual Meeting, Expanded Abstracts, 26, 323–327

[71] Warpinski, N. (Volume 61, Issue 11, Pages 80-85, 2009). Microseismic Monitoring: Inside and Out. Journal of Petroleum Technology, SPE-118537-MS.

[72] Warpinski, N. S., Branagan, P. P., Wolhart, S. G., & Uhl, J. S. (SPE 40014, 1998). Mapping Hydraulic Fracture Growth and Geometry Using Microseismic Events Detected by a Wireline Retrievable Accelerometer Array . SPE Gas Technology Symposium, Calgary, Alberta, Canada.

[73] Warpinski, N.R., Sullivan, R.B., Uhl, J.E., Waltman, C.K., and Machovoe, S.R. 2005a. Improved Microseismic Fracture Mapping Using Perforation Timing Measurements for Velocity Calibration. SPE Journal 10-1: 14-23.

[74] Warpinski, N.R., Waltman, C.K., Du, J. and Ma, Q. [2009] Anisotropy effects in microseismic monitoring. SPE paper 124208.

[75] Wender, L.E., Bryant, J.W, Dickens, M.F., Neville, A.S., and Al-Mogbel, A.M., 1998, Paleozoic (Pre-Khuff) hydrocarbon geology of the Ghawar area, eastern Saudi Arabia: GeoArabia, v. 3, p. 273-301

[76] Winterstein, D. F., and G. S., De, 2001, Vti documented, Geophysics, 66(1), 237–245

Vitae

Name : Haitham Own Mohammed Alsahfy

Nationality : Saudi Arabian

Date of Birth : 2/8/1986

Email : Alsahfy@hotmail.com

Address : 7180 Mohammed Bin Fahad Road
Dammam, 32413 - 3263
Eastern Province, Kingdom of Saudi Arabia

Academic Background : B.Sc. of Geophysics, University of Oklahoma

Publications :

1) H. Alsahfy, A.L. Vesnaver, M. Jervis, & H. Kuleli "3D relocation of errors of microseismic event by surface and borehole receivers for shale gas stimulation" an abstract submitted to EAGE 2014

2) H. Alsahfy, G. Korvin, A.L. Vesnaver, M. Jervis, & H. Kuleli "Improved Microseismic event location accuracy: The role of acquisition geometry and velocity model" to 15AKUW SPE Unconventional Workshop March 19-31st, 2015, Kuwait

3) H. Alsahfy, A Al-Ghamdi, "Optimized 3D Seismic Acquisition, Processing and interpretation for Unconventional Resources in Saudi Arabia" on Second EAGE/SPE/AAPG Shale Gas Workshop (21 – 24 September 2014; Dubai, UAE)

4) A. Ahmed, A. Hakami, H. Alsahfy, & F. Oyarzabal "Kingdom Shale Gas Hydrocarbons as Emerging Resource Play and Impact of Successful North/South America Analogs" to GEO2014, Manama, Bahrain

5) H. Sadi Kuleli, H. Alsahfy, "Microseismic Event Detection and Enhancement Using Phase Detectors" submitted to first EAGE/SPE/AAPG Shale Gas Workshop (21 – 24 September 2013; Dubai, UAE)